UNIVERSITÄT HAMBURG
DEPARTMENT PHYSIK

Glass transition near the free surface studied by synchrotron radiation

Dissertation

zur Erlangung des Doktorgrades des

Fachbereichs Physik

der Universität Hamburg

vorgelegt von

Marcin Sikorski

aus

Bydgoszcz, Polen

Hamburg

2008

Gutachter der Dissertation:	**Priv. Doz. Dr. R. Röhlsberger**
	Prof. Dr. W. Wurth
Gutachter der Disputation:	**Prof. Dr. W. Wurth**
	Prof. Dr. E. F. Weckert
Datum der Disputation:	**10.06.2008**
Vorsitzender des Prüfungsausschusses:	**Dr. M. Martins**
Vorsitzender des Promotionsausschusses:	**Prof. Dr. J. Bartels**
Dekan des Fachbereichs Physik:	**Prof. Dr. R. Klanner**
Dekan der Fakultät für Mathematik, Informatik und Naturwissenschaften:	**Prof. Dr. Arno Frühwald**

Abstract

A comprehensive picture of the glass transition near the liquid/vapor interface of the model organic glass former dibutyl phthalate is presented in this work. Several surface-sensitive techniques using x-ray synchrotron radiation were applied to investigate the static and dynamic aspects of the formation of the glassy state from the supercooled liquid. The amorphous nature of dibutyl phthalate close to the free surface was confirmed by grazing incidence x-ray diffraction studies. Results from x-ray reflectivity measurements indicate a uniform electron density distribution close to the interface excluding the possibility of surface freezing down to 175 K.
Dynamics on sub-μm length-scales at the surface was studied with coherent synchrotron radiation via x-ray photon correlation spectroscopy. From the analysis of the dispersion relation of the surface modes, viscoelastic properties of the dibutyl phthalate are deduced. The Kelvin-Voigt model of viscoelastic media was found to describe well the properties of the liquid/vapor interface below room temperature. The data show that the viscosity at the interface matches the values reported for bulk dibutyl phthalate. The scaled relaxation rate at the surface agrees with the bulk data above 210 K. Upon approaching the glass transition temperature the free surface was observed to relax considerably faster close to the liquid/vapor interface than in bulk.
The concept of higher relaxation rate at the free surface is also supported by the results of the quasielastic nuclear forward scattering experiment, during which dynamics on molecular length scales around the calorimetric glass transition temperature is studied. The data were analyzed using mode-coupling theory of the glass transition and the model of the liquid(glass)/vapor interface, predicting inhomogeneous dynamics near the surface. The quasielastic nuclear forward scattering data can be explained when the molecular mobility is assumed to decrease with the increasing distance from the interface.

Zusammenfassung

Die vorliegende Arbeit zeichnet ein umfassendes Bild des Glasübergangs an der Grenzfläche von der Flüssigkeit zur Gasphase am Beispiel des organischen Modellglasbildners Dibutyl-Phthalat. Mittels mehrerer oberflächensensitiver Verfahren wurden die statischen und dynamischen Aspekte bei der Bildung des Glaszustandes aus der unterkühlten Flüssigkeit mit Synchrotronstrahlung untersucht. Der amorphe Charakter von Dibutyl-Phthalat nahe an der Oberfläche bestätigte sich durch Phasenanalysen an dünnen Schichten mittels Diffraktionsuntersuchungen. Ergebnisse aus Messungen des Reflexionsvermögens deuten auf eine konstante Elektronendichteverteilung in der Nähe der Grenzfläche hin und schließen die Möglichkeit einer Oberflächenkristallisation bis zu einer Temperatur von 175 K aus. Die Dynamik an der Oberfläche auf Längenskalen im sub-μm-Bereich wurde mit kohärenter Synchrotronstrahlung mittels Röntgen-Photonen-Korrelations-Spektroskopie untersucht. Aus der Analyse der Dispersionsrelation der Oberflächenwellen wurden die viskoelastischen Eigenschaften von Dibutyl-Phthalat abgeleitet. Es stellte sich heraus, dass das Kelvin-Voigt Modell viskoelastischer Körper für die Beschreibung der Eigenschaften an der Grenzfläche von Flüssigkeit zu Gas unterhalb von Raumtemperatur gut geeignet ist. Die Daten zeigen, dass die Viskosität an der Grenzfläche mit den Volumenwerten, die für Dibutyl-Phthalat angegeben werden, übereinstimmt. Auch die skalierte Relaxationsrate an der Oberfläche entspricht oberhalb von 210 K den Volumendaten. Bei Erreichen der Glasübergangstemperatur wurde beobachtet, dass die freie Oberfläche bedeutend schneller relaxiert als das Volumen. Die These einer höheren Relaxationsrate an der freien Oberfläche wird auch durch die Ergebnisse des quasielastischen kernre-sonanten Streuexperimentes, bei dem die Dynamik auf molekularen Längenskalen um die kalorimetrische Glasübergangstemperatur herum untersucht wurde, bestätigt. Die Daten wurden mithilfe der Modenkopplungs-Theorie des Glasübergangs und des Modells des Übergangs von flüssig (Glas) zu gasförmig analysiert und prognostizierten dabei eine inhomogene Dynamik in der Nähe der Oberfläche. Die Daten der quasielastischen kernresonanten Streuung können erklärt werden, wenn man annimmt, dass die molekulare Mobilität mit zunehmendem Abstand von der Grenzfläche abnimmt.

Contents

Chapter 1

Motivation

The dramatic change in the molecular dynamics of amorphous systems around the glass transition temperature T_g is a well-known phenomenon in condensed matter physics. The relaxation of the disordered state at the temperatures down to T_g is subject of investigations for a wide range of materials, like polymers, metallic glasses, molecular liquids, foams, and others. Despite the differences in their nature, all the glassy systems shear common features: nonexponential relaxation towards (metastable) equilibrium and dramatic increases of the viscosity upon approaching T_g. Although the general physics is universal for all glasses, the detailed behavior varies. A large number of theories have been developed to describe the mechanisms involved in the vitrification of the glass from the supercooled liquid state but non of them explains all of the observed phenomena. One of the strategies applied to gain a unified description of the glass transition is based on the systematic studies of model glass formers. By comparing the results from different experiments a complete picture of the physics of the glassy state is expected to be obtained. Considering the similarities in the outcomes from the studies of various systems, the universal theory of glasses is intended to be developed. Unfortunately, the systematic analysis of the observed phenomena is difficult due to the dependence of the obtained results not only on the system under study and its thermal history but also on the the applied experimental approach.
The major part of the studies of the glass transition phenomenon has been focused on the samples. Despite a large number of experimental approaches used to study the static structure and dynamics of the supercooled and the frozen states, a universal empirical description of the glass has not been formulated. The investigation of the dynamics of glasses confined to nanometer sizes is believed to be a direct way to verify the key concepts of the glass transition phenomenon. However, the studies of the glass transition of confined liquids often lead to contradictory results. The observed phenomena seem to be a complex superposition of volume effects and interaction effects with the confining matrix, which often can not be precisely separated during the data

analysis. An advantage of studying the free surface is that all of the observed phenomena have their origin in the disordered state of the sample and are free from sample-matrix interactions. The asymmetry of the molecular arrangement in the vicinity of the interface, is expected to alter the static and dynamic properties of the amorphous state. The influence of the boundaries on the dynamics of the supercooled liquid is an extremely important aspect of the glass transition phenomenon from the basic science and the technological point of view. A free surface is the most common boundary, to which an amorphous system can be subjected. The enhanced diffusion, excitation of thermal vibrations, surface crystallization or surface melting are only a few examples out of a wide spectrum of effects unique for the liquid/vapour interface. Many experiments and simulations have been performed to verify the concept of an enhanced molecular mobility at the free surface. However, due to experimental limitations, the increase of the relaxation rate near the free surface is usually deduced in an indirect way investigations of the effects only related to the surface dynamics. The most common systems for those kind of studies are the polymers. For those systems the observed phenomena are the convolution of intrinsic properties of the interface with the effects originating from the large dimensions and the complicated shapes of the constituent chains.
The aim of this project was to study the dynamics of the supercooled liquid state at the free surface of the model organic, non-polymeric, glass former dibutyl phthalate with x-ray scattering techniques. This compound combines a simple molecular structure with a high glass forming ability. The dynamics of the supercooled and glassy states of dibutyl phthalate was heavily investigated for both bulk samples and in confinement. The surface-limited picture of glass transition is intended to be compared with the results obtained in different geometries. The measurements are expected to provide the answers concerning the influence of the liquid/vapour interface on the glass transition. The surface induced deviation from the bulk short-range order is going to be monitored with help of diffraction studies, while the temperature dependent picture of the surface waves will be gained from the x-ray reflectivity and x-ray photon correlation spectroscopy investigations. From the analysis of the dispersion relation of the surface modes the concept of the viscoelasticity of the supercooled liquid surface is planed to be verified. The molecular dynamics at the timescales corresponding to the transition from the fast β- to α-relaxation will be the subject of the quasielastic nuclear forward scattering experiment performed in the grazing incidence geometry. The value of the critical temperature T_c at the liquid/vapour interface will be deduced from the analysis of the delayed resonant signal patterns in the framework of the mode-coupling theory of the glass transition. The purpose of this project is to provide a length-scale dependent estimation of the glass transition temperature at the surface of dibutyl phthalate and squalane. The interconnection between the picture of the dynamics on the molecular level with the one provided by continuum theory and the capillary wave model is searched for.

Chapter 2

The glassy state

The term glass is used to name non-crystalline solids, which often, due to historical reasons, is identified with an amorphous material formed by rapid cooling from the melt. The physics of the disordered state has been investigated for a wide range of systems with different sizes of the structural unit (atoms, particles, molecules, chains, and others). The recent members of the glass formers family are the metallic alloys. Their tendency to suppress crystals nucleation during cooling was heavily studied for different sample compositions, dimensions, and applied cooling rates R [1]. In case of metallic glasses the relaxation processes are studied on the atomic level. Formation of long-range order takes place via rearrangement of single atoms or small clusters. In contrary to the metallic alloys for polymers, known to exhibit high glass forming ability, the smallest structural unit consists of tens of atoms. The dynamics of their supercooled state has been investigated in bulk [2, 3] and reduced dimensions [4, 5, 6]. Also other organic liquids, characterized by much smaller molecular sizes were observed to transform from liquid into glass without any sign of crystallization when cooled with sufficiently high speed. Regardless of their nature, all glasses show common features like dramatic increase in the viscosity close to the glass transition temperature or the non-exponential relaxation toward the (metastable)equilibrium.

Fig. 2.1 displays the temperature dependence of the specific volume V, thermal expansion coefficient α_p, and enthalpy H for for the case of crystallization and glass vitrification. For the supercooled liquid those quantities are significantly higher in comparison to the crystalline state at the same temperature. However, below the glass transition temperature they settle on similar level as for the long-range ordered structures. The transition between both values is not instantaneous (like in case of the crystallization process) but extends over a certain temperature interval. According to the Ehrenfest classification scheme the formation of the glass can not be classified neither as a first nor as a second order phase transition.

One of the most interesting feature of the glass transition phenomenon is the

fact that the temperature at which it occurs depends strongly on the thermal history of the system. The amount of liquid-like disorder "trapped" is a unique property of the investigated sample and its thermal history. Measured properties of the glass were found to dependent on both sample treatment and the experimental method. The effect of increase of T_g with the increase of the applied cooling(heating) rate R was studied, for example, by means of differential scanning calorimetry (DSC) [8] and x-ray reflectivity (XR) [9].
A systematic classification of the glass formers based on the evolution of the viscosity η of the supercooled liquid versus temperature T has been proposed by Angel [10], who introduced the fragility index m(T) [11, 12, 13]

$$m(T_g) = -\frac{d\log_{10}\eta}{d\ln T}\,|_{T=T_g}\,. \tag{2.1}$$

The value of m ranges from about 15 (strong glasses) up to around 200 (fragile glasses). The strong glasses show Arrhenius-type dependence between T and η (see Fig. 2.2), while the viscosity of the fragile glass formers is often well described by the Vogel-Fulcher-Tammann (VFT) equation above T_g

$$\eta = \eta_\infty \exp(\frac{B}{T-T_0}). \tag{2.2}$$

The meaning of the parameters η_∞, B, and T_0 in the eq. 2.2 is still not clarified. Two of them serve as asymptotes. For the infinitely high temperature the viscosity of the investigated liquid would be equal to η_∞ and complete freezing-in of the structure ($\eta \to \infty$) is predicted to take place at the Vogel temperature T_0. The VFT equation is often used to model the viscosities of glass forming liquids upon approaching T_g. However the temperature interval of its applicability has been observed to vary for different samples. For example, it was found to break down close to T_g in case of salol, α-phenyl-o-cresol, and trio-α-naphtylbenzene, while an agreement over eleven decades was found between collected data and VFT predictions for glycerol, ethylene glycol, and

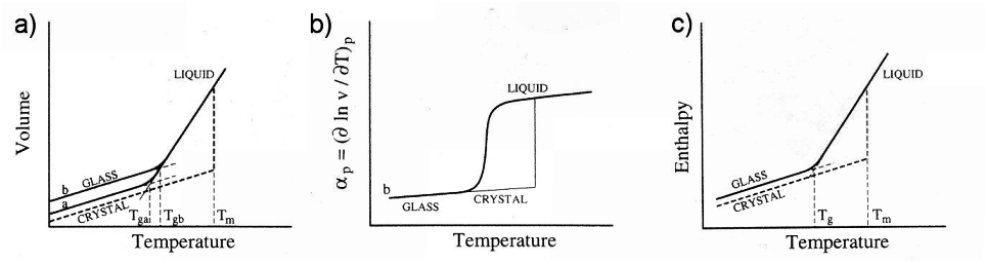

Figure 2.1: The relationship between a) the volume V, b) thermal expansion coefficient α_p, and c) enthalpy H and temperature T in the liquid, glassy, and crystalline state. T_m is the melting point, while the glass transition temperature is denoted by T_g. Figure taken and modified from [7].

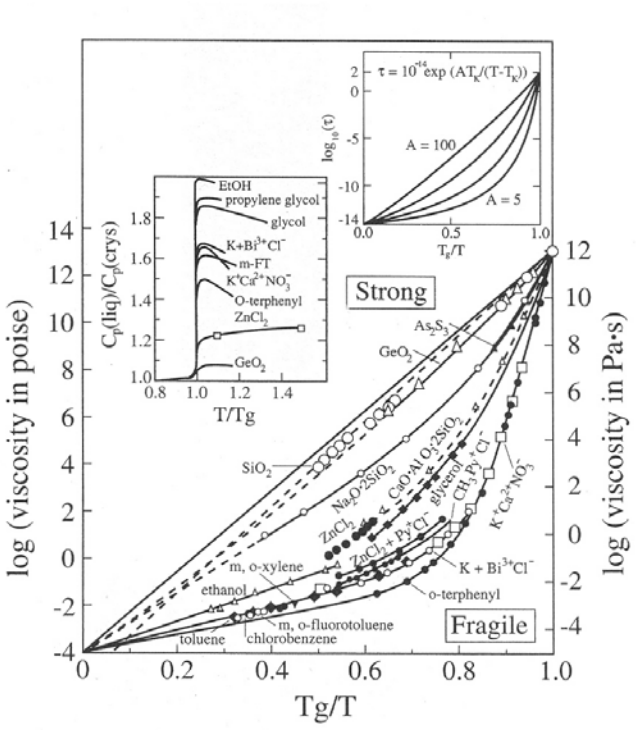

Figure 2.2: Dependence of the viscosity on the reduced temperature for selected glass formers. Figure taken from [7].

propylene glycol.

An interpretation of the "strength" of the glasses in the potential energy hypersurface (see Fig. 2.3) has been given by Angel [7]. The strong glasses are supposed to have low density of the energy minima, while for the fragile glasses the number of accessible potential wells is significantly greater. The third class of the glass formers are the hydrogen-bounded systems. They are believed to be thermodynamically fragile (posses large number of energy minima) and at the same time kinetically strong (high energy barriers for the structural evolution).

2.1 Adam-Gibbs theory

The theory of the transition from the liquid to glassy state formulated by Adam and Gibbs [14], is based on the concept of a temperature dependence of the size of cooperatively rearranging regions (CRR) in the supercooled liquid. In a very dense medium, particles (molecules) are not able to move independently from their surrounding but instead the simultaneous change in the position of a larger volume is necessary. The size of such a region is a function

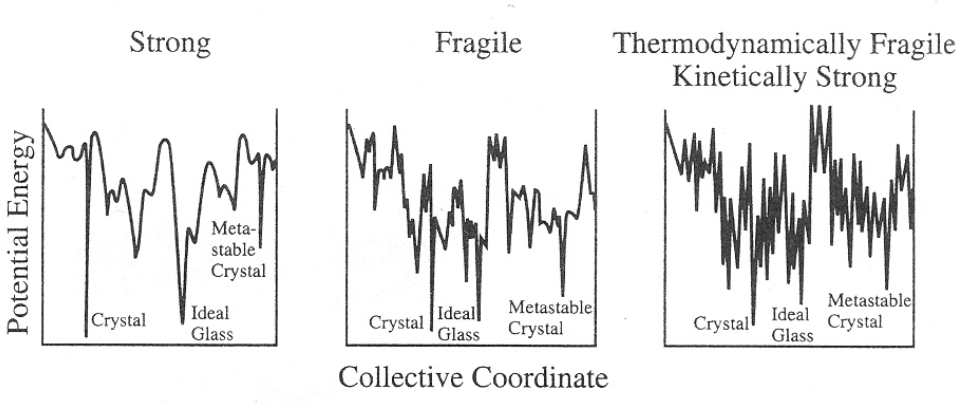

Figure 2.3: Schematic representation of the potential energy barrier hyperspace os strong (left), fragile (center), and kinetically strong and thermodynamically fragile (right) glasses. Figure taken from [7].

of temperature and becomes comparable with the sample dimensions at the glass transition temperature.
The Adam-Gibbs (AG) theory predicts a following relation between the relaxation time τ and temperature T

$$\tau \propto \exp(\frac{C}{T\Delta s}), \tag{2.3}$$

where Δs is the molar entropy difference between the supercooled liquid and the crystal. The change in the chemical potential $\delta\mu$ and the configurational entropy of the critically sized cooperatively rearranging region are incorporated in the constant C. Making use of fact that

$$\Delta s(T_g) = \int_{T_k}^{T_g} \frac{\Delta c_p}{T} dT \tag{2.4}$$

it is straightforward to obtain the Vogel-Fulcher-Tamann (VFT) form for the temperature dependence of the viscosity

$$\tau \propto const. \times \exp(\frac{A}{T - T_k}) \propto \eta, \tag{2.5}$$

where T_k stand for the Kauzmann temperature [7]. Several assumptions made during the formulation of the Adam-Gibbs theory were proofed to be in an apparent disagreement with experimental results. First of all the simple exponential relaxation function is implied by the Adam-Gibbs model, while the measurements clearly point into the stretched exponential scheme. Furthermore, the increase in T_g in confinement predicted by Adam-Gibbs model is contradictory to the experimental finding for many model glass formers like

ortho-terphenyl [15], for which the opposite effect was observed. However, the cooperative motion is still considered as one of the possible mechanisms of structural relaxation of the supercooled state.

2.2 Free volume model

An alternative picture of the glass transition mechanism was proposed by Turnbull and Cohen [16]. Denoting the average volume per molecule by ν and the volume excluded for other molecules by ν_0, the excess volume of the glassy system is given by $\nu - \nu_0$ and is assumed to be a function of temperature T. Raising T results in the creation of an extra volume in the ensemble, which must be redistributed uniformly among all of the constituent species. Thermal expansion results from the increased amplitude of the vibrational motion and does not differ much from the crystal value. As the temperature exceeds T_g part of the excess volume (called the free volume ν_f) can be redistributed randomly among the constituent particles. In a such situation the thermal expansion of the system is liquid-like. The ideal glass transition occurs upon cooling the sample when $\nu_f = 0$.
In contrast to the high temperature liquid state, molecules in a dense medium are constrained by so-called cages created by their neighbors. Density fluctuations may cause temporal opening of such cages and allow the trapped molecule to jump out of such confinement, giving rise to long-range diffusion. The viscosity is defined in the frame of the free volume model as

$$\eta^{-1} = A \exp(-\frac{b\nu_0}{\nu_f}). \tag{2.6}$$

The constants A and b in formula 2.6 are of order of unity.
The weakest point of the free volume picture is the fact that the redistribution of the excess volume is assumed not to require any local free energy so the modeled system is obviously in equilibrium, which is in contradiction to experiential findings. Additionally, the theoretically predicted reduction of the sample volume during freezing overestimates the observed values. Regardless the apparent drawbacks of the glass transition model proposed by Turnbull and Cohen, the concept of the cage effect was adapted by later models of the relaxation process and is often used to explain experimental findings.

2.3 Mode-Coupling theory

Initially, mode-coupling theory (MCT) has been applied to describe the dynamic of simple liquids. MCT is based on the idea of density-density correlations in the liquid state and freezing of the density fluctuations at the glass transition temperature. The key quantity of this theory is the normalized

intermediate scattering function defined as

$$F(q,t) = \langle \partial n(q,t) \partial n(-q,0) \rangle / N. \tag{2.7}$$

The density fluctuation $\partial n(q,t)$ are defined with respect to the quasi-equilibrium average value $n(t)$. The van Hove correlation function $G(r,t)$ is related to the $F(q,t)$ via the Fourier transform

$$G(r,t) = \langle \partial n(r,t) \partial n^*(0,0) \rangle / \rho. \tag{2.8}$$

Following the Mori-Zwanzig formalism an equation of motion for the correlators can be formulated

$$[\frac{\partial^2}{\partial t^2} + \frac{\partial}{\partial t}\gamma + \omega^2(q)]F(q,t) + \omega^2(q) \int_0^t M(q,t-t') \frac{\partial}{\partial t'} F(q,t') dt = 0, \tag{2.9}$$

where ω is the characteristic frequency and a Newtonian friction term is denoted by γ. This equation resemble the one of the damped harmonic oscillator. The retarded coupling, which explains the stabilization of the density fluctuations, is implemented in the kernel $M(q,t)$. Laplace transformation yields the following solution

$$F(q,t) = \frac{-1}{z - \frac{\omega^2}{z + M(q,z)}} \tag{2.10}$$

where

$$M(q,z) = i\gamma + \omega^2 m(q,z). \tag{2.11}$$

Factor $m(q,z)$ depends essentially on $F(q,z)$. Only the "slow" solutions of eq. 2.9 are relevant from the glass dynamics point of view. That implies $m(q,z)$ to be also slowly varying functions of time. The memory function should mimic the environment of the particle, which in the case of a supercooled liquid is the cage formed by the neighboring particles, $m(q,z)$ can be approximated by the sum over density fluctuations

$$m(q,t) = \sum_{q_1,q_2} V_{q,q_1,q_2} F(q_1,t) F(q_2,t). \tag{2.12}$$

At high temperatures the coupling constants V_{q,q_1,q_2} are small what leads to a fast decay of density fluctuations (liquid state). Higher values of V_{q,q_1,q_2} represent the glassy state, in which the density fluctuations do not decay but remain localized. The transition between two limits occur suddenly at a critical density ρ_c corresponding to the mode-coupling critical temperature T_c, which is predicted to be well above the calorimetric glass transition temperature T_g. The evolution of the intermediate scattering function in time is presented in Fig. 2.4. Far above T_c $F(q,t)$ decays fast to zero. In this regime particles are completely free to diffuse. Upon approaching T_c the relaxation splits into a slow and a fast part. The fast relaxation, called the fast β-relaxation, is

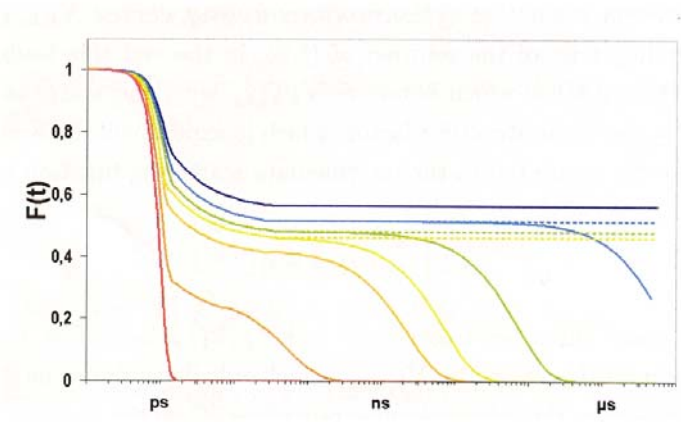

Figure 2.4: Normalized intermediate scattering function $F(q,t)$ for liquid at high (red) and low (orange) temperatures, at the critical temperature T_c (yellow), and far below T_c (green and blue) according to an extended MCT (solid) and an ideal MCT (dotted line). Figure taken from [17].

ascribed to the rattling of the molecule in the cage, while the slower one, the α-relaxation, is responsible for breaking or/and the movement of the cage. According to ideal mode-coupling theory, the diffusion constant vanishes and the viscosity diverges below T_c. This is in apparent contradiction to the experimental findings. In the framework of extended mode-coupling theory this discrepancy has been attributed to thermally activated hopping processes responsible for shifting the freezing of the supercooled liquid from T_c to T_g. The complete freezing of the structure is reflected by the plateau-like behavior of $F(q,t)$ for all experimentally accessible times.

Chapter 3

Samples

3.1 Dibutyl phthalate

Dibutyl phthalate $C_{16}H_{22}O_4$ abbreviated as **DBP** (CAS No: *84-74-2*) is a colorless viscous organic solvent widely used in industry as a plasticizer. Its molecule (see Fig. 3.1) consists of a phthalic ring with two hydrocarbon tails attached to it. Its very high ability to form a glass without any signs of crystallization makes dibutyl phthalate a model sample to investigate the supercooled state of organic matter. A fragility index of m=69 places dibutyl phthalate at the border of fragile and medium glasses. Differential scanning calorimetry measurements yields a glass transition temperature $T_g = 178 \pm 1$ K(heating rate 10 K/min) [18]. The physical properties of dibutyl phthalate, both in the

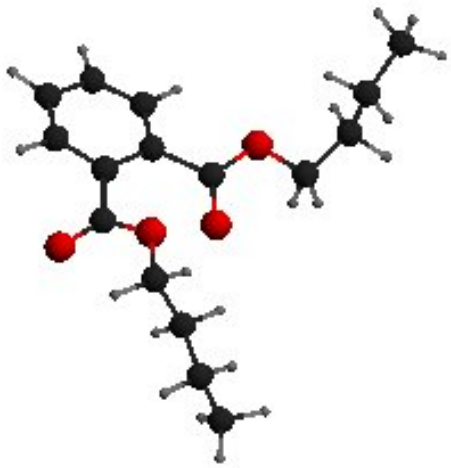

Figure 3.1: The dibutyl phthalate molecule $M_W = 278.34$.

liquid and the glassy state, have been investigated for bulk [19, 20, 21, 18] and for confined samples [22, 23]. At 295 K dibutyl phthalate is characterized

by the viscosity $\eta = 21 \times 10^{-3}$ Pas and the density $\rho = 1.05$ g/cm^3. The possibility to tune the viscosity without introducing the crystal nucleation allows to study both fast and slow relaxation of the amorphous state. Upon cooling $\eta(T)$ was found to follow the Vogel-Fulcher-Tamman law in a wide temperature range [20, 24]

$$\ln(\eta(T)) = \ln(\eta_0) + \frac{B}{T - T_0}, \tag{3.1}$$

with the Vogel temperature $T_0 = 151.3K$ [25, 20, 26]. The density of dibutyl phthalate ϱ changes with temperature as [20]

$$\rho(T) = 1.15\frac{g}{cm^3}[1 - 6.68 \times 10^{-4}K^{-1}(T - 151.3K)]. \tag{3.2}$$

Dibutyl phthalate is an example of the non-polymeric molecular liquid exhibiting elastic properties above its melting temperature $T_m = 238$ K. The room temperature measurements show that the observed level of the elasticity of this compound depends on the frequency of the applied external shear force. Beside the GHz regime [20], solid-like behavior of dibutyl phthalate was confirmed for the relatively slow shear forces $f \leq 40$ Hz [27]. The viscoelasticity of the bulk dibutyl phthalate was investigated at different length- and timescales using x-rays [25], light scattering [28], and ultrasonic methods [29].
The molecular dynamics in the glassy state of DBP was measured with dielectric relaxation [21, 30], and quasi-elastic nuclear forward scattering [23]. The reported results show stretched exponential $\alpha-$relaxation as omnipresent in glassy samples. In the time domain the experimental data are described by the Kohlrausch function [26]. The exact value of the stretching exponent β and its temperature and pressure dependence has been investigated by several authors [26, 21, 31, 32] but often the inconsistent results are reported.
Small size and simple molecular structure make dibutyl phthalate a ideal system for studies of the concept of the diverging length-scales at the glass transition. The relaxation rate of DBP has been observed to be a strong function of the applied geometrical constrains. For example, the nuclear forward scattering studies of dibutyl phthalate injected into nanoporous silica matrices clearly show an increase of the relaxation time of dibutyl phthalate, for the diameter of the pores smaller than 75 Å [33]. Confinement introduces also anisotropy of the glass transition. The dynamic of the dibutyl phthalate molecules was measured to vary within the pore cross-section [17].

3.2 Squalane

The second liquid, to be studied is squalane $C_{30}H_{62}$ (CAS No: *111-01-3*). This colorless, transparent oily alkane with molecular weight $M_W = 422.83$ is widely used in cosmetic industry as a skin lubricant. The squalane molecule

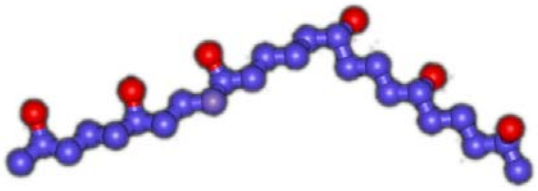

Figure 3.2: The squalane molecule $M_W = 422.83$.

(see Fig. 3.2) consists of a C_{24} backbone and six methyl groups attached symmetrically around the center of the backbone. $C_{30}H_{62}$ is characterized by a slightly higher fragility m=75 [34] than dibutyl phthalate, and lower bulk glass transition temperature T_g=167 K [35].

The viscosity of squalane can be described by the Vogel-Fulcher-Tamman equation [36] with T_0=119 K. The elastic properties of $C_{30}H_{62}$ as a function of temperature were investigated by means of dielectric spectroscopy [36]. An interesting feature of the alkane family is the strong sensitivity of the structure of those compounds to the applied geometrical constrains. The layering of the squalane molecules next to a solid interface has been a subject of both theoretical and experimental investigations [37, 38]. Often contradictory results were reported. The density fluctuations in the liquid squalane near the liquid/solid interface were observed to depend on the structure of the used substrate. For example, evidence of ordering of the squalane molecules was found for $SiO_2/Si(100)$ and pyrolitic graphite, while no such effect was found for a mica substrate.

X-ray reflectivity and grazing incidence diffraction experiments confirmed that the liquid/vapor interface induces similar effect as for the liquid/solid counterpart. Surface crystallization of C_{18}, C_{20}, and C_{24} alkanes has been observed to occur at temperatures slightly above ($\Delta T \approx$3 K)the bulk melting temperature [39]. The data support the picture of hexagonally packed structures with molecules oriented in the direction normal to the surface. The ordering effect is limited to a thin layer, while the rest of the sample remains liquid.

3.3 Ferrocene

Ferrocene $Fe(C_5H_5)_2$ (CAS no:*102-54-5*) is a organometallic compound with a sandwich-like molecular structure (see Fig. 3.3). In its natural state it forms orange crystals, which are soluble in organic solvents but insoluble in water.

A good chemical stability, small molecular volume and weight $M_W = 186.4$ make ferrocene an excellent candidate for a tracer if the presence of iron inside the investigated sample is needed. It is often used to mimic the dynamics of

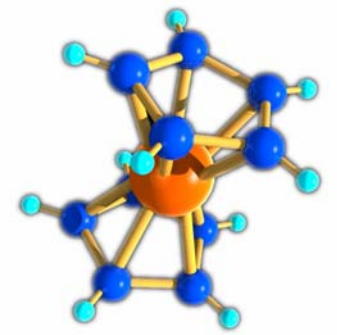

Figure 3.3: The ferrocene molecule $M_W = 186.4$.

other organic liquids, such as dibutyl phthalate [40, 33, 23, 26], for experiments based on the Mössbauer effect.

The solubility limits of ferrocene in dibutyl phthalate and squalane were found to be at the level of 5% for both liquids.

Chapter 4

Liquid sample cryostat

One of the goals of this project was to develop a cryostat well-suited for the studies of the liquid/vapor interface using synchrotron radiation. For x-rays, the surface-sensitivity is established by applying the grazing incidence geometry. Since the typical lateral dimensions of the footprint of the incident beam on the investigated surface exceeds several centimeters for angles of incidence α_i lower than the critical angle α_c, a large meniscus-free area of the studied liquid is desirable. It is well-know that many organic molecules suffer radiation damage when exposed to x-rays. To optimize the data acquisition, the cryostat should provide an area of the sample large enough to allow for a translation of the studied surface in the direction perpendicular to the scattering plane. The chemical resistance of the sample environment to the organic solvents is an important issue. Any chemical reaction of the probed liquid with its surrounding could result in contamination of the sample and/or in malfunction of the experimental setup.
Calorimetric measurements yield a glass transition temperatures 179 K for dibutyl phthalate and 167 K for squalane. Since no estimates of T_g near the free surface could be provided beforehand, the cryostat was expected to operate at least down to 140 K with stability better than 0.1 K.
An important requirement to be met by the setup concerns the possibility to perform experiments in various scattering geometries. For example, to conduct the reflectivity measurements a wide range of accessible incident and exit angles in the vertical direction is needed, while the scattered intensity at large exit angle in the horizontal plane is recorded during diffraction studies.

The principles of the design and operation of the cryostat used during this project have been based on an already existing setup [41]. In comparison to the previous version, both the cooling and vacuum system were improved, in order to meet all of the experimental requirements, especially the minimum available temperature around 100 K. An overview of the cryostat is presented in Fig. 4.1. The investigated liquid is encapsulated in the inner Cu chamber.

Removable Cu troughs with several different depths (0.1 mm, 0.3 mm, and 0.5 mm) serve as sample holders. The influence of the meniscus, formed in the vicinity of the rim, on the curvature of the liquid surface has been minimized by setting the diameter of the specimen holder to ϕ=120 mm. Depending on the details of the experiment two kinds of troughs can be used. When the standard one is used, the whole area of the plate is covered. This sample holder is well-suited for measurements requiring the large dimensions of the studied surface, while the apparent drawback is the necessity to dip the temperature sensors directly into the measured specimen.

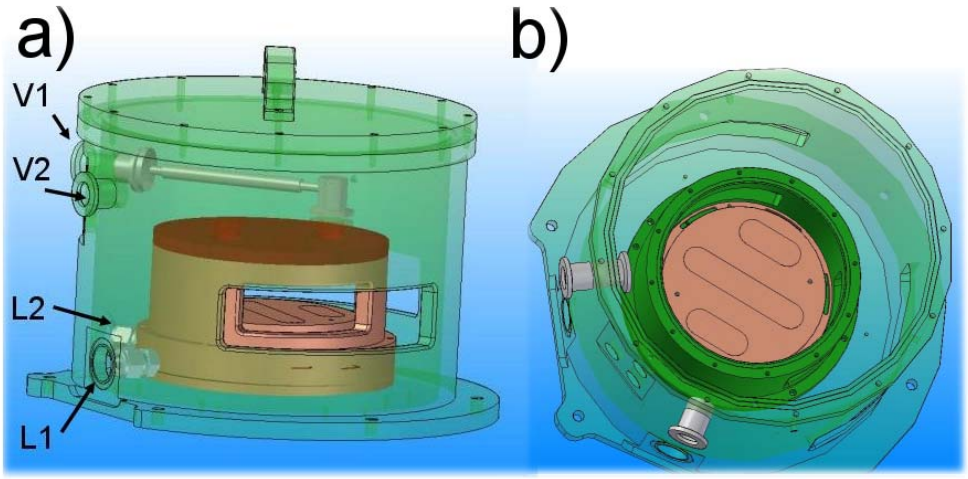

Figure 4.1: 3D model of the liquid sample cryostat. a) The closed cryostat; the vacuum (V1, V2) and the liquid nitrogen (L1, L2) connectors are indicated by arrows. b) The mounting of the Cu sample plate with three reservoirs.

In case, when only a very limited amount of sample is available or it can not be in contact with the sensors, a three-reservoirs version of the trough should be used. The central reservoir contains the liquid to be investigated with the x-ray beam, while the side reservoirs are filled with liquid, into which the temperature sensors are dipped.

Because of the significant difference in the thermal expansion between copper and organic glasses, mechanical stress is created inside the specimen, which may result in fracture and cracks on the sample surface in the solid state. In practise, this limits the minimum temperature, to which the investigated glass can be cooled. This problem was overcome by coating the sample plate with an additional, preferably organic, thin layer. The purpose of it is to absorb the mechanical stress inside the coating layer and to maintain the thermal shrinkage of the sample and its support at a comparable level. The buffer layer has to exhibit resistance to organic solvent, good wetting by the investigated liquids, and mechanical stability at temperatures close to 100 K. Among several compounds tested, a 30 μm thick teflon coating was found to be the

optimal compromise for all experimental requirements.
High efficiency of the cooling system and excellent temperature stability was

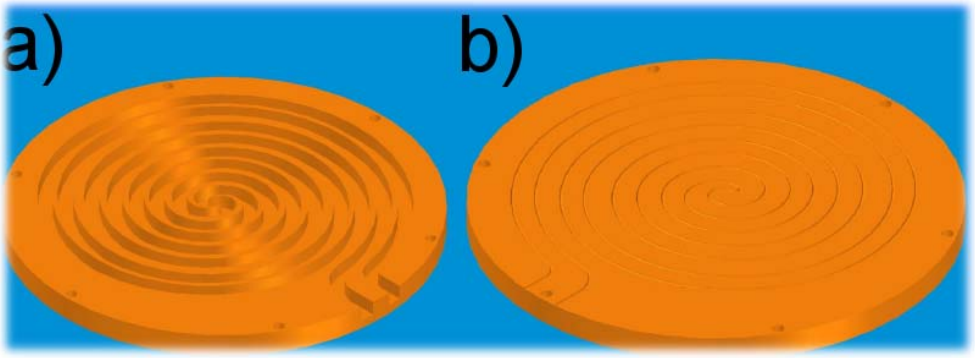

Figure 4.2: The cooling plate seen form a) the bottom (liquid nitrogen) and b) the top(heater) side. The spiral shape of the grooves on both sides ensures uniform heat distribution over the whole surface.

achieved by manufacturing the cooling plate as an integral part of the inner chamber. The sample temperature is controlled by tuning the heating power, while keeping the cooling power i.e. the liquid nitrogen flow constant. The amount of electrical current flowing through the wire heater, mounted between the chiller and the sample chamber is adjusted by a Lakeshore 340 temperature controller. The actual sample temperature is measured independently by two Pt100 sensors. They can be dipped directly into the sample or into separate portions of sample poured into the auxiliary reservoirs (see Fig. 4.1). Additionally, the third sensor, mounted outside the sample chamber, is used to monitor the temperature of the cooling plate. All three temperatures together with the level of the electrical output power currently supplied by the Lakeshore 340 are displayed and stored on the PC connected to the controller via GPIB interface card. The developed software allows also the basic on-line data treatment.
The cryostat was designed to operate with liquid nitrogen as a cooling medium. However, also other cryogenic liquids or cold gasses can be used with this setup. The highest cooling efficiency is achieved, when the evaporation of the liquid N_2 takes place inside the cooling plate (see Fig. 4.2).

Vacuum-isolated pipes are used to reduce the heat losses between the cryostat and the liquid nitrogen source. The fine tuning of the cooling power is done by adjustment of the amount of exhaust N_2 gas by means of a mass flow controller. During standard operation, the flow rate of nitrogen gas is kept at 14 to 25 l/min. The upper limit for the mass flow controller to operate is around 100 L/min of N_2. An important factor determining the amplitude of the temperature deviations from the setpoint versus time is the stability of the pressure of the cooling liquid. The best performance was reached for

liquid nitrogen pressure within the range from 1 to 2.2 bars. In the current configuration, the pressure inside the cooling system should not be larger than 3 bars. A safety valve mounted upstream the mass flow controller assures that this limit is not exceeded.
The purpose of the outer chamber is to establish thermal isolation of the sample chamber. To avoid water condensation on the outer kapton windows, the pressure between both chambers should not exceed a few mbars while the standard vacuum inside the inner one is maintained below 1 mbar. A system of valves allows independent pumping of either of the two chambers. Two independent pressure sensors are used to monitor the vacuum level inside both chambers.
The cryostat is designed for a wide range of surface sensitive measurements on the liquid surface. The large opening of the windows allows tuning of the angles, at which the x-rays impinge on the surface and the angles at which they are detected within $\Delta\psi_{incident} = \Delta\psi_{exit} = \langle -15°; 60° \rangle$ in horizontal and $\Delta\alpha_{incident} = \Delta\alpha_{exit} = \langle 0; 15° \rangle$ in vertical direction. This allows to investigate the sample/vapor interface with different x-ray or neutron experimental techniques like diffraction, reflectivity, correlation spectroscopy and others.
In the standard configuration, the cryostat operates from 95 K up to 400 K with a stability better than 50 mK over a time interval of several hours(Fig. 4.3). The maximum cooling and heating rate are strong functions of the temperature T. In the range from 300 K to 150 K they are equal to around 0.6 and 0.4 K/min, respectively. The averaged time needed to change the sample temperature by 10 K was determined empirically to be equal to around 30 minutes in this temperature region. Below 150 K the performance of the cryostat becomes strongly dependent on the liquid nitrogen pressure and the vacuum level inside the outer chamber. The speed at which the temperature can be ramped is a function of the given experimental conditions like the quality of the thermal isolation and the pressure of the liquid nitrogen. To compensate the heat losses between the chambers, higher cooling power is required and the nitrogen flow must be increased often to above 30 l/min.
Several additionally components have been developed to improve the performance of the cryostat. For example a system of valves was built to connect two dewars to the cryostat, what extends the time between liquid nitrogen refills to around 100 hours and allows long timescale experiments to be conducted without any break.

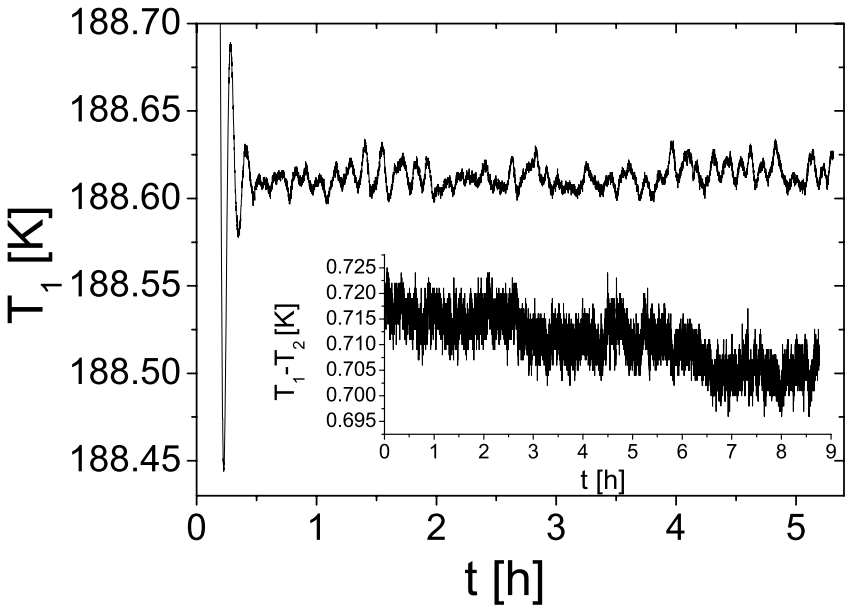

Figure 4.3: Variation of the sample temperature T_1 vs. time recorded by one of the sensors during a typical experiment. The time interval t<30 min corresponds to the stabilization of the cryostat when the new setpoint has been reached. The difference between the previous and current set temperature was greater than 40 K in this case. Inset: The temporal discrepancy in the temperatures measured by two Pt100 sensors $T_1 - T_2$.

Chapter 5

X-ray reflectivity and grazing incidence x-ray diffraction

5.1 Motivation

The aim of the x-ray reflectivity (XR) and grazing incidence diffraction experiments (GID) was to obtain detailed information about the structure of the surface of the investigated liquids. It is of the highest importance to exclude ordering effects next to their liquid/vapor interfaces for the temperature range of interest. By ruling out the possibility of surface crystallization, one makes sure that all the phenomena observed during other experiments originate from the amorphous nature of the specimen. X-ray reflectivity measurements provide information about the profile of the sample in the direction perpendicular to its surface. From the shape of the reflectivity curves one can deduce the electron profile and the evolution of the surface roughness as the temperature of the specimen is lowered. For the nuclear forward scattering (NFS) experiment, the investigated liquids must be doped with an iron-containing compound. As described in section 3.3, the most common tracer used to mimic the motion of dibutyl phthalate molecules is ferrocene $Fe(C_5H_5)_2$. The goal of the GID and XR experiments, was to test if, within the detection limits, the addition of ferrocene alters the dibutyl phthalate surfaces.
The diffraction experiment was performed to proof that the structure of the investigated liquids near its surfaces does not differ from the bulk structure, in the temperature region of interest.

5.2 Theoretical background

5.2.1 X-ray reflectivity XR

The interaction of a medium with x-rays can be described by means of the complex index of refraction

$$n(\vec{r}) = 1 - \delta(\vec{r}) + i\beta(\vec{r}), \tag{5.1}$$

with

$$\delta(\vec{r}) = \frac{\lambda^2 r_e \varrho(\vec{r})}{2\pi} \tag{5.2}$$

$$\beta = \frac{\lambda\mu(\vec{r})}{4\pi}, \tag{5.3}$$

where $\delta(\vec{r})$ is the dispersion coefficient, $\beta(\vec{r})$ stands for the absorption coefficient, $\varrho(\vec{r})$ denotes the electron density at point $\vec{r}$, λ is the radiation wavelength, r_e=2.814×10^{-5}Å is the classical electron radius, and $\mu(\vec{r})$ is the linear absorption coefficient. The principle of reflectivity measurements is based on the phenomenon of reflection of the incident electromagnetic wave, described by the wavevector $\vec{k}$ and the frequency ω

$$\vec{E}(\vec{r}) = \vec{E_0}\exp(i(\vec{k}\cdot\vec{r} - \omega t)) \tag{5.4}$$

at the interface of media characterized by different complex indices of refraction n_1 and n_2, respectively. The quantity of interest is the ratio of the reflected intensity $I(\alpha_i)$ to the incident one I_0 as a function of the incident angle $\alpha_i = \alpha_f$

$$R(\alpha_i) = \frac{I(\alpha_i)}{I_0}. \tag{5.5}$$

For a perfectly flat interface the change of the electron density across the border of two media follows a step function behavior. The reflectivity, in this case, can be calculated using the Fresnel formula

$$R_f = |\frac{k_{i,z} - k_{t,z}}{k_{i,z} + k_{t,z}}|^2, \tag{5.6}$$

where $k_{i,z} = k\sin\alpha_i$, $k_{t,z} = k\sqrt{n^2 - \cos^2\alpha_i}$, $n_1 = 1$, and $n_2 = n$. The components of the wavevector transfer $\vec{q} = \vec{k_f} - \vec{k_i}$ are given by following formulas[1] [42]

$$q_x = \frac{2\pi}{\lambda}(\cos\alpha_f\cos\frac{\psi}{2} - \cos\alpha_i) \tag{5.7}$$

$$q_y = \frac{2\pi}{\lambda}\cos\alpha_i\sin\frac{\psi}{2} \tag{5.8}$$

[1]The wavevector transfer q calculated in vacuum ($n_1 = 1$). For definition of an angle ψ see Fig. 5.3.

$$q_z = \frac{2\pi}{\lambda}(\sin\alpha_i + \sin\alpha_f). \tag{5.9}$$

The roughness σ of the real interface causes a smearing of the electron density in the transition region across the border between the media (see Fig. 5.1) and reduces its ability to reflect incident x-rays. As the scattering amplitude

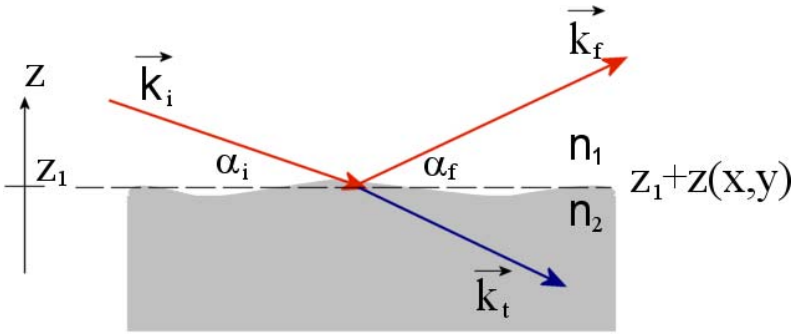

Figure 5.1: In-plane scattering geometry of a plane wave with wavevector $\vec{k_i}$ impinging on the rough surface characterized by the mean z coordinate z_1 and fluctuation $z(x, y)$. The incident wave splits into reflected $\vec{k_f}$ and refracted part $\vec{k_t}$.

is proportional to the Fourier transform of the electron density, the intensity reflected by the rough interface can be determined by

$$\frac{R(q_z)}{R_F(q_z)} = |\frac{1}{\varrho_\infty}\int_0^\infty \frac{d\varrho(z)}{dz}e^{iq_z z}|^2 \tag{5.10}$$

where $\varrho(z)$ is the electron density at height z and ϱ_∞ denotes the average electron density of the bulk medium. The quantity $q_z = 2k\sin\alpha_i$ in eq. 5.10 denotes the z-component of the wavevector transfer $\vec{q}$. The distribution of ϱ_z across the interface is often modeled using the error function $\varrho_z = erf(z/(\sqrt{2}\sigma))$. The Fourier transform of its derivative is a Gaussian, leading to

$$R(q_z) = R_f(q_z)e^{-q_z^2\sigma^2}. \tag{5.11}$$

Since $\exp(-q_z^2\sigma^2) \to 1$ as $q_z \to 0$ the influence of the surface roughness on the reflectivity is more pronounced at larger q_z values. For liquids the imperfection of the interface is explained by the presence of thermally exited capillary waves (CW). For such systems, the roughness is expected to be a function of the surface tension γ, the temperature T, the averaged size of the molecule r_M, and the experimental resolution of the setup (detector slit opening h_d and sample to detector distance L) [43]

$$\sigma^2 = \frac{k_B T}{2\pi\gamma(T)}\ln(\frac{2\pi}{q_z r_M \frac{h_d}{L}}). \tag{5.12}$$

The amplitude of those fluctuations is expected to decrease as the temperature is lowered. Upon approaching the glass transition temperature T_g, the examined liquid freezes, so do the capillary waves. Thus the evolution of $\sigma(T)$ can provide an estimation of T_g.

5.2.2 Grazing incidence diffraction GID

The x-ray intensity I($\vec{q}$) scattered from a surface of a simple molecular liquid is determined by its form factor S($\vec{q}$) and the transmission function of the incident $T_i(\alpha_i)$ and the scattered $T_f(\alpha_f)$ electromagnetic wave [44]

$$I(\vec{q}) \propto |T_i(\alpha_i)|^2 |T_f(\alpha_f)|^2 |S(\vec{q_z^t})|^2. \tag{5.13}$$

The distribution of the intensity within the diffraction pattern provides an information about the arrangement of the molecules in the irradiated liquid. For the liquid(glassy) specimen, the lack of the long-range correlations in the sample structure is reflected by the broad amorphous "hump" on collected data, while in case of the crystallized sample very sharp Bragg reflections are present for wavevector transfers $\vec{q}$ fulfilling the conditions [45]

$$\vec{q} = \vec{k_f} - \vec{k_i} = \vec{G_{hkl}}, \tag{5.14}$$

where

$$\vec{G_{hkl}} = h\vec{a}' + k\vec{b}' + l\vec{c}'. \tag{5.15}$$

The h, k, l are the integer numbers and $\vec{a}', \vec{b}', \vec{c}'$ are the primitive reciprocal lattice vectors[2].

The diffraction experiment performed under the grazing incidence ($\alpha_i < \alpha_c$) condition is a powerful tool for investigation of the 2D structure of thin films and interfaces [46]. The principle of grazing incidence diffraction is based on the fact that the volume of the sample probed with x-rays is a function of the angle α_i, at which radiation impinges the surface and angle α_f, at which the diffracted photons are detected. The surface-sensitivity results from the exponential decay of the amplitude of the incident electromagnetic field in the irradiated medium as a function of depth z $E(z) = E_0 e^{-z/\Lambda}$, where the factor Λ is called the penetration depth and can be estimated using formula [47]

$$\Lambda = Im(\frac{2\pi}{\lambda}(\sqrt{\sin^2\alpha_i - 2\delta + i2\beta} + \sqrt{\sin^2\alpha_f - 2\delta + i2\beta}))^{-1} \tag{5.16}$$

For $\alpha_i \leq \alpha_c$ the evanescent wave, confined to a few nm thick topmost part of the interface is excited. In Fig. 5.2 a typical variation of Λ as a function of α_i and α_f for several values of the absorption coefficient β is presented.

[2] In the further part of this work the vector notation will be omitted for the sake of convenience.

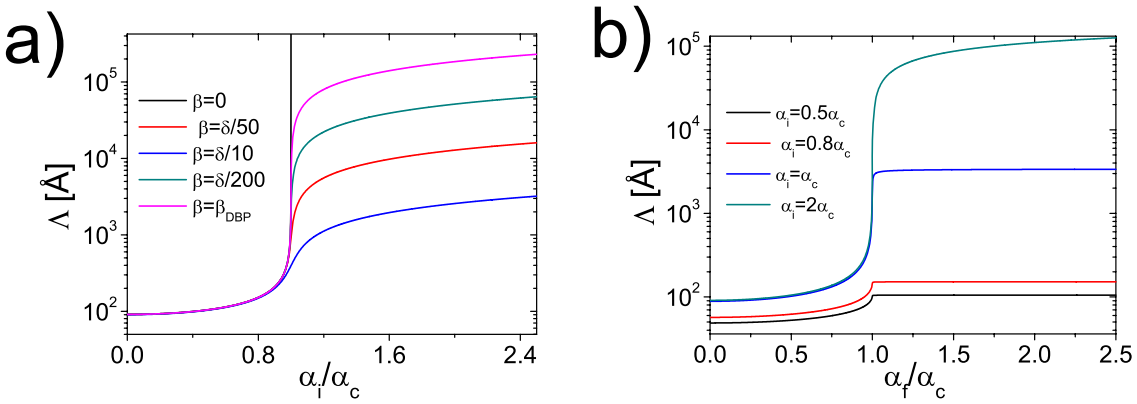

Figure 5.2: a) Calculated penetration depth Λ of 9.5 keV x-rays (λ=1.3 Å) as a function of the angle of incidence α_i for several selected absorption coefficients β including the one of dibutyl phthalate $\beta_{DBP} = 3.7 \times 10^{-9}$ and b) function of the exit angle α_f for different α_i and $\beta = \beta_{DBP}$.

The electron density used for the calculation of these curves equals to the one of dibutyl phthalate and the wavelength λ=1.3 Å corresponds to energy of x-rays used during the reflectivity and GID experiments. A simplified scheme of a diffraction experiment performed under grazing incidence of conditions is shown in Fig. 5.3. The incoming radiation impinges the surface of the sample at $\alpha_i < \alpha_c$, interacts with the sample, and the diffracted part is collected using a position sensitive detector (PSD), located at an angle ψ with respect to the specular direction. The detector resolution is determined by the opening of the soller slits mounted in front of it. By varying the value ψ one obtains the distribution of the diffracted intensity. Each point of such a 2D pattern correspond to certain set of the angles α_i, α_f, ψ and can be transformed into the reciprocal space with the help of eq. 5.7 to 5.9. The in-plane information is obtained by integrating the intensity collected along the direction perpendicular to the sample surface for different values of ψ. The components q_x and q_y, in this case, can be combined to the lateral wavevector transfer

$$q_{||} = \frac{2\pi}{\lambda} \sin \frac{\psi}{2}. \tag{5.17}$$

For GID the condition for the constructive interference (eq. 5.14) reduces to 2D form

$$G_{hk} = q_{||}. \tag{5.18}$$

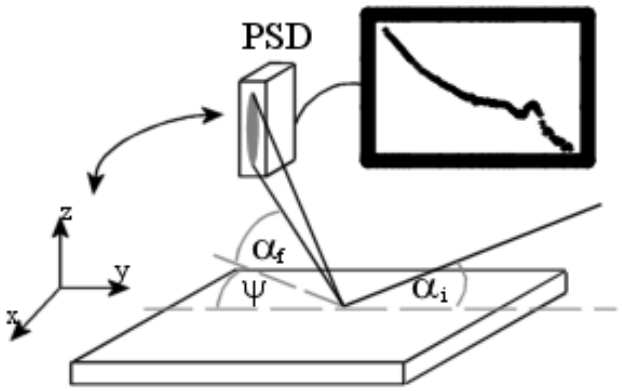

Figure 5.3: Schematic set-up of x-ray diffraction measured under grazing incidence conditions.

5.3 Experimental details

The x-ray reflectivity and grazing incidence diffraction (GID) measurements were performed at beamline BW1 at HASYLAB, which provides a high intensity beam from a wiggler insertion device. The 9.5 keV part of the radiation is selected using a Be(200) crystal in Laue geometry. The angle, at which the incident beam struck the surface of the sample was changed within a wide range from 1 mrad to around 88 mrad by tuning the tilt of that crystal. The cryostat was mounted on the liquid sample diffractometer allowing the horizontal translation in addition to the sample height adjustment. The specular part of the reflected x-rays is detected using a NaI point detector and the off-specular radiation is collected with a Braun linear position sensitive detector PSD. The layout of the experimental setup at BW1 is shown in Fig. 5.4. The typical reflectivity data set collected at BW1 cover eight orders of magnitude. To optimize the data acquisition procedure, the reflected intensity was collected with two different detectors. For α_i around the critical value, the reflected intensity was measured using the vertically mounted NaI detector. In this geometry, the detector "sees" only a part of the reflected radiation, scattered by the kapton foil. The weaker signal at higher angles was recorded using the horizontally positioned, second point detector. The Al attenuator wheel was used for a fine adjustment of the incident intensity. The size of the beam was set to h_V=0.1 mm in vertical and h_H=1 mm in horizontal direction. The small height of the beam limits the footprint length to around 50 mm at the critical angle and minimizes the influence of the meniscus on the recorded data.
The level of the background was determined by repeating corresponding reflectivity scans for a detector detuned from the specular plane of an angle ψ=12.2 mrad.

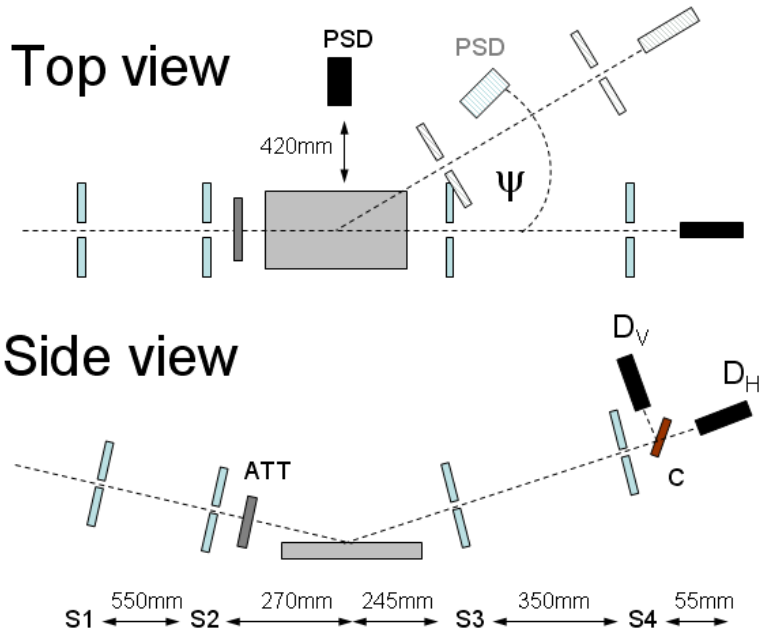

Figure 5.4: Layout of the beamline BW1 at HASYLAB. S1, S2, S3, S4 - slits, ATT - attenuator wheel, C - Kapton foil, D_H - horizontal point detector, D_V- vertical point detector, PSD - position sensitive detector. Opening of the slits: $S1 = 2.1 \times 10mm^2$, $S2 = 0.1 \times 1mm^2$, $S3 = 4 \times 10mm^2$, and $S4 = 1.4 \times 4mm^2$.

The alignment of the beamline was tested by collecting reflectivity scans of distilled water at 300 K. The obtained data together with the corresponding fit (eq. 5.11) is presented in Fig. 5.5. The values of dispersion $\delta = 2.52 \times 10^{-6}$, absorption $\beta = 6.0 \times 10^{-9}$ coefficients, and the surface roughness σ=3.17 Å extracted from the fitting routine are in good agreement with the data reported in literature [48].
Diffraction patterns were collected with a Braun linear detector. During each measurement the scattering angle ψ was scanned from around 10 mrad to 0.7 rad. The smallest accessible angle ψ_{min} was limited by the horizontal width and divergence of the incident beam. A satisfactory compromise between ψ_{min} and the diffracted intensity was found for a footprint width w_H=1 mm. The upper limit ψ_{max} was defined by the opening of the window of the inner chamber in the cryostat. The value of α_i was set to 1.8 mrad, what corresponds to $0.8\alpha_c$ and limits Λ to around 76 Å. The quality of the recorded patterns was improved by integration of the diffracted intensity for $\alpha_f < \alpha_c$ at each value of ψ .

The x-ray reflectivity and grazing incidence diffraction measurements were performed for three samples: $C_{16}H_{22}O_4/Fe(C_5H_5)_2$, dibutyl phthalate and

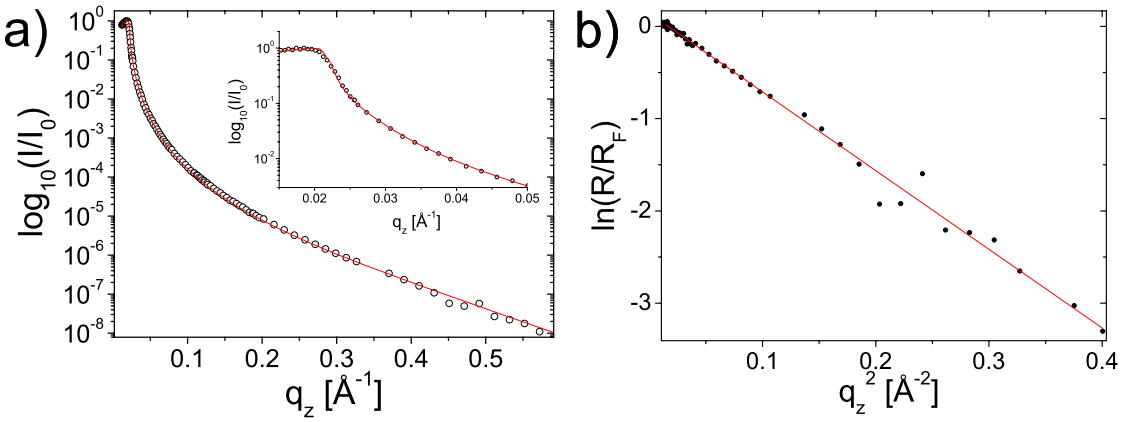

Figure 5.5: a)Reflectivity curve of distilled water measured at 300 K. The obtained value of the surface roughness is $\sigma = 3.17$ Å. Inset: the low-q_z part of reflectivity data. b) Data normalized to the Fresnel reflectivity R_F as a function of q_z^2.

squalane. The purity of the investigated liquids is an important issue for surface measurements. Since in the grazing incidence geometry, the typical depth "seen" by the x-rays is around few tens of Å, even a single monolayer of impurities may produce artificial effects and alter the properties of the investigated interface.
The liquids were poured into a 0.3 mm deep Cu through. The pressure inside the inner and outer chambers was kept at 10^{-3} mbar and 10^{-4} mbar level, respectively.

Table 5.1: Selected properties of investigated liquids at 295 K.

Sample	γ $(\frac{mN}{m})$	δ $(\times 10^{-6})$	ρ $(\frac{g}{cm^3})$	α_c $(mrad)$	Λ † Å
H_2O	73	2.54	1.00	2.27	76
$C_{16}H_{22}O_4$	34	2.59	1.05	2.27	76
$C_{30}H_{62}$	28	2.12	0.81	2.09	84
$Fe(C_5H_5)_2$	-♯	6.33	2.69	3.49	-♯

† Values calculated for $\alpha_i = \alpha_f \approx 0.8\alpha_c$
♯ Data not relevant for the measurement, since a pure $Fe(C_5H_5)_2$ was not studied during this project

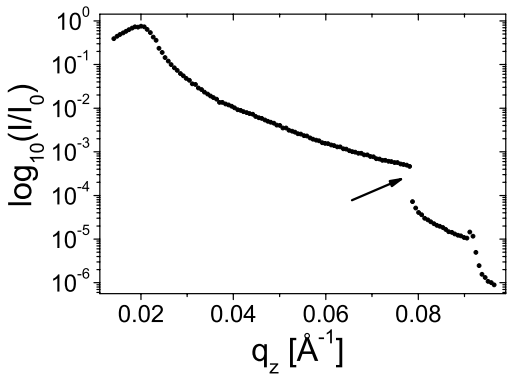

Figure 5.6: An example of the damage of the dibutyl phthalate surface by the radiation. The reflectivity curve was collected at 230 K with the point detector oriented vertically. The arrow indicates the q_z, at which the attenuator was removed from the beam.

The temperature was ramped down with an average rate of 0.5 K/min. After reaching every setpoint, the sample was kept at the desired temperature until the difference of the values shown by the Pt100 sensors settled at a constant level.
A dramatic decrease of the signal reflected from the surface of dibutyl phthalate was observed when the sample was exposed to high x-ray flux (see Fig. 5.6). This effect has been found to be fully reproducible for fixed experimental conditions. However, it vanished when a thicker Al foil has been used to attenuate the incident beam. Sudden drop in the ability of the studied surface to reflect the x-rays can be attributed to dibutyl phthalate being destroyed by the high intensity x-ray beam. At lower temperatures, the mobility of the molecules at the surface is reduced, resulting in the reduced ability of the capillary waves to "stir" the illuminated liquid, what is reflected by the higher sensitivity of the measurements to the damage of the studied molecules to the incident radiation.
During all scans, the fast shutter was used to limit the exposure time of the sample to x-rays. To further minimize the possibility of the radiation damage, sample was translated in direction perpendicular to the scattering plane between the consecutive measurements. Despite all precautions, it was not possible to collect reflectivity data from dibutyl phthalate surface at temperatures lower than 175 K at angles higher than the critical angle of total external reflection α_c.

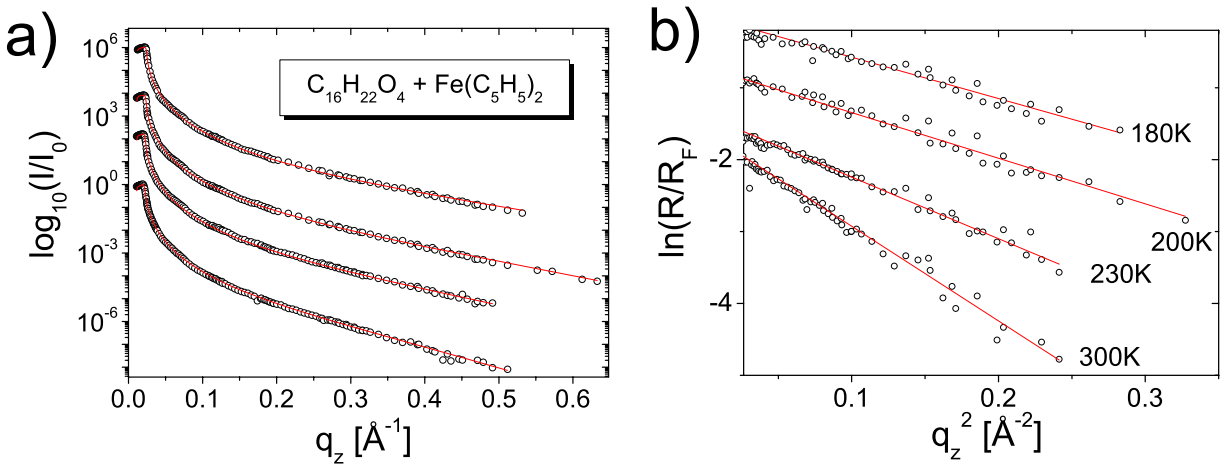

Figure 5.7: a) Reflectivity data of a DBP/ferrocene mixture recorded at 300 K (bottom), 250 K, 220 K, 175 K (top). b) Data normalized to the Fresnel reflectivity R_F as a function of q_z^2.

5.4 Results

5.4.1 Dibutyl phthalate (dibutyl phthalate/ferrocene)

X-ray reflectivity measurements were performed for pure dibutyl phthalate and for the liquid doped with ferrocene. Since the data collected for both samples coincide within the experimental error bars, only the results for $C_{16}H_{22}O_4/Fe(C_5H_5)_2$ are presented in this section.

The reflectivity curves, collected in a temperature range from 300 K down to 175 K, provide simple Fresnel-like shape. All data sets were modeled assuming a semi-infinite, uniform dibutyl phthalate/ferrocene mixture and fitted with eq. 5.11. Selected curves together with the corresponding fits are plotted in Fig. 5.7. When normalized to the Fresnel reflectivity R_F and plotted in logarithmic scale versus q_z^2, all data can be fitted with straight lines (see Fig. 5.7b). No formation of the surface layer was detected down to 175 K.

No indication of surface freezing of dibutyl phthalate was observed in the applied temperature range. The value of the surface roughness σ decreases linearly from 3.65 Å at 300 K to 2.4 Å at 175 K (see Fig. 5.8). According to the capillary wave picture of the liquid/vapour interface, the value of σ^2 is inversely proportional to the surface tension γ (eq. 5.12). The room temperature value of the surface tension agrees well with the literature data $\gamma_{295K} = 34.4$ mN/m. Due to the lack of theoretical or experimental work providing the temperature dependence of γ for dibutyl phthalate, the surface tension values measured at lower temperatures can not be compared with the

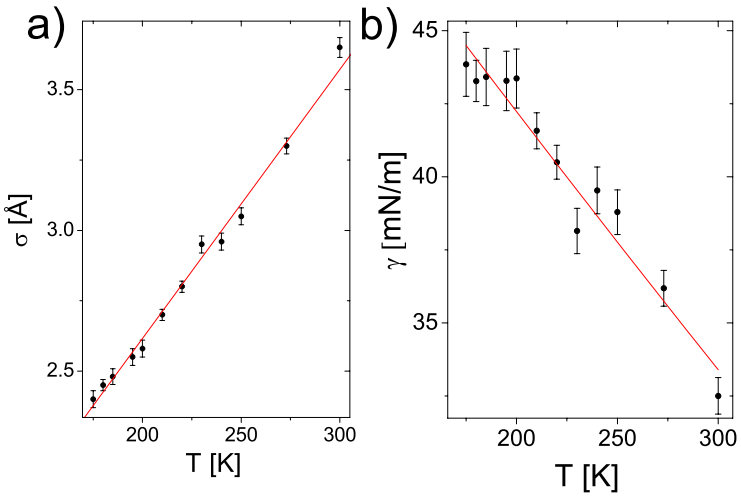

Figure 5.8: a) Values of the surface roughness σ of dibutyl phthalate obtained from reflectivity scans together with a linear fit and b) the corresponding surface tension γ values fitted with formula 5.19 (red line).

capillary waves model predictions. The formula provided by the Guggenheim-Katayama model [49]

$$\gamma = \gamma_0(1 - \frac{T}{T_{critical}})^n \tag{5.19}$$

has been used to described the $\gamma(T)$ profile for dibutyl phthalate. The prefactor $\gamma_0 = (60.9 \pm 1.7)$ mN/m and exponent $n = 1.22 \pm 0.08$ are the compound-dependent parameters, and $T_{critical} = 773$ K is the thermodynamical critical temperature of dibutyl phthalate. It must be pointed out, however that there are no special reasons, to favor this model over many other reported in literature. Eq. 5.19 serves only as mathematical model of $\gamma(T)$, needed for further analysis.

Additionally to the dibutyl phthalate/ferrocene sample also pure dibutyl phthalate was measured at selected temperatures. The values of the electron density and the surface roughness of both samples match within the experimental uncertainty. It can be concluded, that a substitution of 5% dibutyl phthalate molecule by ferrocene does not alter the structure of its liquid/vapour interface.

At room temperature, the electron density calculated from the position of the critical angle agrees with the value estimated for dibutyl phthalate/ferrocene, assuming a uniform mixture with molecular ratio 19:1. The shift of α_c towards higher angles (see Fig. 5.9) reflects the increase in the electron density of $C_{16}H_{22}O_4/Fe(C_5H_5)_2$ at lower temperatures.

The absence of long-range order in dibutyl phthalate near the liquid/vapour

interface was confirmed by means of grazing incidence diffraction measurements.

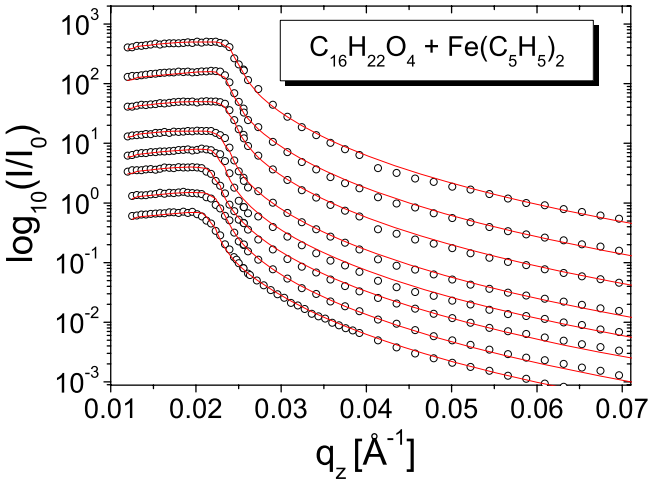

Figure 5.9: Reflectivity curves of $C_{16}H_{22}O_4/Fe(C_5H_5)_2$ recorded at 300 K (bottom), 273 K, 250 K, 240 K, 220 K, 210 K, 200 K, 175 K (top).

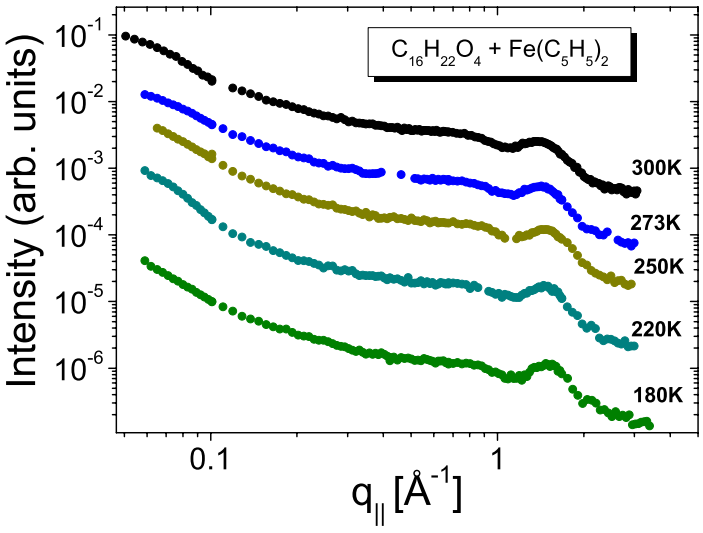

Figure 5.10: GID patterns of $C_{16}H_{22}O_4/Fe(C_5H_5)_2$ collected at 300 K (top), 273 K, 250 K, 220 K, and 180 K(bottom).

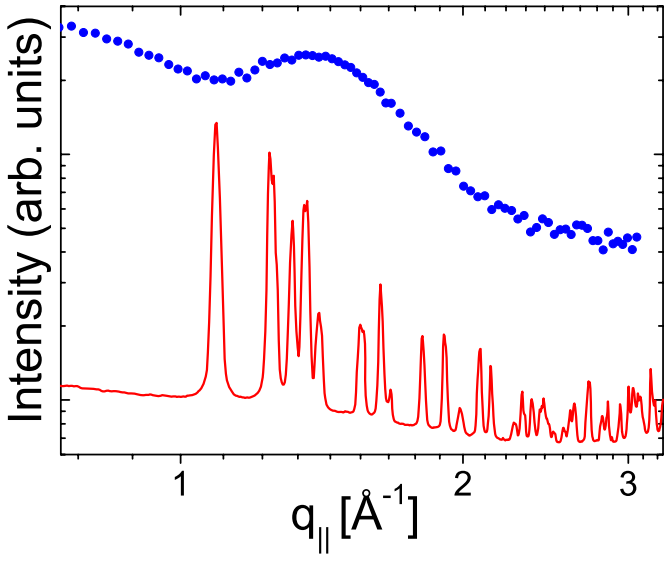

Figure 5.11: The room temperature GID data of DBP/ferrocene mixture (•) compared with the powder diffraction pattern of the crystalline ferrocene (red line).

As presented in Fig. 5.10, the diffraction pattern is similar to that of other aromatic liquids. At 300 K the less intensive prepeak at 0.76 $Å^{-1}$ is followed by the main peak at 1.43 $Å^{-1}$. The position of the second one corresponds to the first coordination shell and is determined by the van der Waals diameter of the molecule. The estimated nearest-neighbor distance d=5.1 Å agrees well with the averaged dimensions of the dibutyl phthalate molecule. The correlation length L=16.12 Å has been estimated from the width of the main peak. The origin of the first peak is still not fully understood. It has been argued that it may reflect the correlation between phenyl groups of neighboring molecules [50, 25]. No significant changes in the diffraction patterns were observed upon cooling the sample down to 180 K (see Fig. 5.10). Decreasing the temperature causes a shortening of the distance between adjacent molecules and results in a slight shift $\Delta q_{||}$=0.05 $Å^{-1}$ of the main peak towards higher $q_{||}$-values, while the position of the prepeak was found to be constant within the experimental error.
The powder diffraction pattern[3] of crystalline $Fe(C_5H_5)_2$ is very rich in the $q_{||}$ range accessible during the surface diffraction experiment (see Fig. 5.11) and the formation of ferrocene crystals near the surface is expected to be reflected

[3]Powder diffraction studies of ferrocene and dibutyl phthalate were part of this project

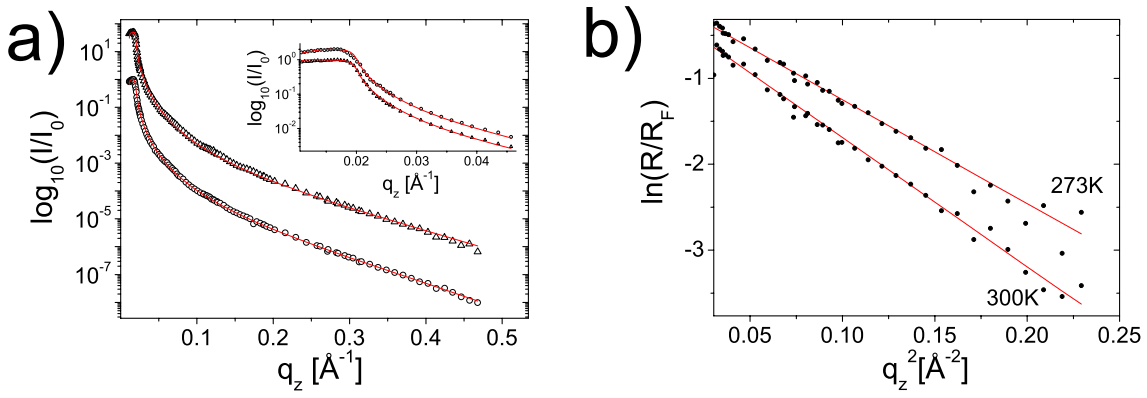

Figure 5.12: a) The reflectivity curves measured for squalane cooled at 300 K (○) and to 273 K (△). b) Data normalized to the Fresnel reflectivity R_F as a function of q_z^2.

by the presence of the corresponding Bragg reflections in the diffraction data. The obtained results verified that such a scenario can be excluded for the temperatures down to 180 K.

5.4.2 Squalane

The reflectivity curves of $C_{30}H_{62}$ collected at 300 K and 273 K are presented in Fig. 5.12.

The fitting routine using eq. 5.11 yields the values of the surface roughness of 3.88 Å and 3.48 Å at 300 K and 273 K, respectively. Further cooling results in formation of the 40 Å thick surface layer with the electron density higher than the bulk liquid value ϱ_{el} by approximately 10%. The surface-induced layering is reflected by the modulation of the Fresnel-like reflectivity profile by Kiessig fringes with the period of $\Delta q_z = 0.16$ Å^{-1} (see Fig. 5.13). The quality of the fits improved, when an intermediate layer with the electron density of $0.9\varrho_{el}$ and 5.9 Å thickness was included into the model. The bilayer model used to analyze the reflectivity curves of the squalane surface has been also reported to explain the reflectivity data collected also for other short and medium-length alkanes C_n with $n \leq 50$ [39, 51]. Those compounds tend to crystalize via so-called rotator phase. This often distorted hexagonal structure is made out of rigid alkane chains oriented perpendicularly to the liquid surface. According to this model, the high density layer indicated by the reflectivity data corresponds to densely packed backbones of the squalane molecules and the low density part underneath consists of CH_3 group at one end of these molecules. The second density depletion region at the other end

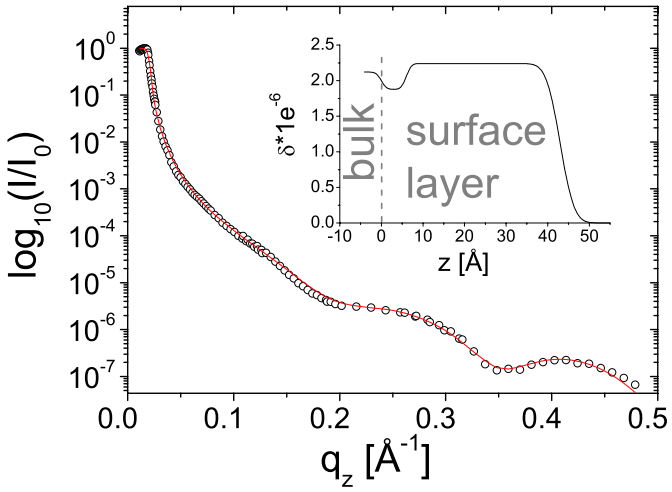

Figure 5.13: Reflectivity curve recorded for squalane cooled down to 260 K and the fit (solid line) with a two layer model. Inset: electron density profile obtained from two layer model.

of the squalane molecules contributes to the value of the surface roughness.

In-plane order near the surface of squalane was subjected to the grazing incidence x-ray diffraction studies. The collected diffraction data confirm the presence of a crystalline phase at a temperature around 260 K. Beside a wide amorphous peak centered at $q_{||}$=1.29 Å^{-1}, an additional Bragg reflection was detected at $q_{||}$=1.52 Å^{-1} (see Fig. 5.14). Both, the position and a FWHM of the amorphous peak do not change in the applied temperature range. The nearest-neighbor distance d=5.6 Å and correlation length L=22 Å were estimated for the squalane in the liquid state. When the crystals are formed those quantities change to 4.8 Å and 615 Å , respectively. No other Bragg reflections were observed in the accessible $q_{||}$ range. It should be stressed, that for squalane the temperature interval between the surface crystallization and melting is much greater than the values reported in literature for other alkanes. For C_{30} both transitions are separated by more than 20 K, while in case of C_{18}, C_{20}, and C_{24} this difference reduces only to 3 K [39].
The possible explanation of such a high discrepancy between the expected crystallization temperature and the measured one is the presence of impurities in the investigated liquid. Although the producer guaranties the purity of the squalane to be higher than 99%, the presence of contaminations in the specimen must be given careful consideration. It is very likely, that the major part of the impurities are squalane derivatives, the byproducts of the synthesis reaction. Other possible impurities, which have a structure similar to alkanes are fatty acids and alcohols. According to literature fatty acids do not form an extra surface layer, while a bilayer structure at the liquid/vapor interfaces

of alcohols was observed.
Performed measurements show that the cryostat does not provide sufficiently high cooling rate to prevent the crystal nucleation in supercooled squalane. This excludes $C_{30}H_{62}$ from further investigations in the framework of this project.

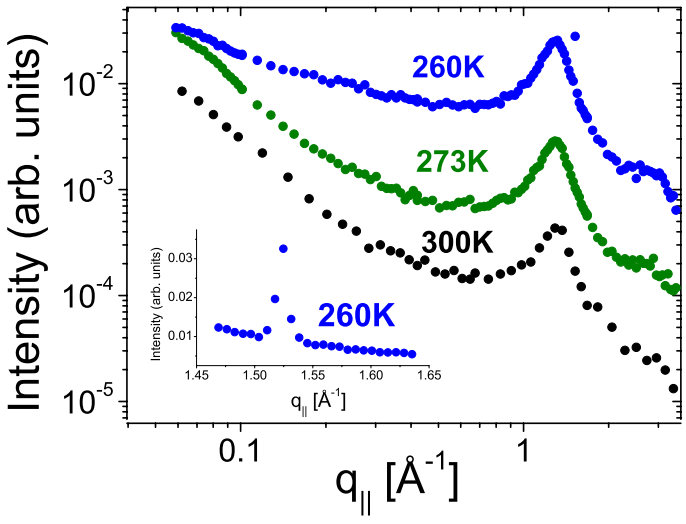

Figure 5.14: The grazing incidence diffraction patterns collected at 300 K (bottom), 273 K, and 260 K (top). Inset: The Bragg reflection observed at 260 K.

Chapter 6

X-ray photon correlation spectroscopy

6.1 Motivation

The aim of the grazing incidence x-ray photon correlation spectroscopy (XPCS) experiment was to investigate the dynamical aspects of the glass transition phenomenon at the free surface of dibutyl phthalate on μm length-scales. A detailed insight into the relaxation of the supercooled liquid was intended to be gained by the investigation of the dynamics of the thermally excited capillary waves modes as a function of temperature. Since the values of the viscosity $\eta(T)$ and the shear modulus μ(T) can be deduced by refinement of the dispersion relation of the surface waves, the viscoelastic behavior of dibutyl phthalate near the free surface can be verified by means of the XPCS studies.

6.2 Viscoelasticity of liquids

It has been theoretically predicted and experimentally proven that a broad range of liquids show a shear elastic effect in addition to viscous flow. A unique possibility to study the viscoelasticity is offered by strong glass forming liquids. By lowering the temperature, the viscosity and the elastic modulus can be tuned over several orders of magnitude without introducing long range structural order. The length-scale and time-scale dependence of the elastic parameters in the liquid state have been investigated for various liquids using different experimental approaches [27, 20, 52]. Despite extensive theoretical and experimental work, no satisfying explanation of the origin of the viscoelastic phenomenon in the liquid state has been given until now. There is no general theory, covering the full range of the structural relaxation times τ. For short τ the Maxwell model is argued to describe the elasticity on a satisfactory level, while the Kelvin-Voigt scheme is applied to explain the properties of high viscosity systems. The viscoelasticity of organic liquids becomes even

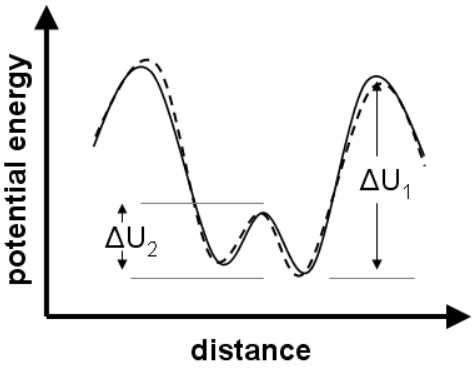

Figure 6.1: Potential energy diagram of a viscoelastic medium according to Mason at al. [53]. The dashed line shows the change in the energy landscape, when an external shearing force is applied.

more complicated, when the influence of geometrical constraint is taken into account. For example, in the case of a free surface, additional hydrodynamic modes are present, which can not be observed in bulk systems.

Polymers are often considered to be model systems for studies of the viscoelasticity of the supercooled liquid state. Their rheological properties have been investigated in great detail for wide a variety of molecular weights M_W and polymer to solvent ratios. The elastic properties of the molecular liquids are believed to originate from the intra- and intermolecular interactions. For example, Mason at al. [53] analyzed the results of ultrasonic measurements of polymerized castor oil and polyisobutylene polymer liquids, dividing molecules into several structural units, called segments. A single segment was assumed to consist of tens of atoms. According to this model, for a liquid consisting of long molecules, certain coiled-up shapes are more probable than others and if a molecule is distorted from such a favorable state, it tends to return to the initial shape in a very short time τ when the stress is removed. This feature is called configurational elasticity. Under shear stress, collective jumps of the cluster of molecules are expected to take place. Such rearrangement results in a change of the center of gravity of the molecules together with a change in their shape. The first process produces viscous flow, while the second one is responsible for configurational shear elasticity. Above a certain threshold value of viscosity or frequency of the shear stress, the segments can not follow the changes of the external force and are trapped in the potential wells. In such a case segments can only be displaced within a given local energy minimum. In this regime, the shear modulus is expected to be of the order of 10^9 Pa. Both the configurational and the high frequency elasticities were suggested in [53] to be dominated by the nearest-neighbor interaction. In terms of an energy landscape, the mobility of each segment is restricted to the local potential wells separated by the energy barriers of different heights (see Fig.

6.1).

Since the viscous flow involves translation as well as rotation, the higher energy barrier ΔU_1 must be overcome by the molecule. The barrier ΔU_2 is associated with the configurational elasticity due to the extension or contraction of the chain. The relative heights of the energy barriers are changed by applying the external shear force $F(t)$. After sufficiently long time t_1, a molecule jumps over ΔU_1 and viscous flow takes place. When the period of $F(t)$ is reduced below t_1, a molecule can only cross ΔU_2 and the configurational elasticity becomes pronounced. The level of elasticity is directly related to the mobility of each segment within the chain. In the limiting case, the frequency of $F(t)$ is so large, that the distortion of the molecule is due to slight displacement of the constituent segment from their equilibrium positions. This results in the large shear modulus comparable to the typical value of the crystalline materials. As the length of the molecule decreases, the distribution of the potential wells becomes more and more uniform and the distinction between the local distortion and the flow process disappears, thus the configurational elasticity can not be observed.

6.3 Capillary waves

Soft matter surfaces are covered by thermally excited capillary waves CW fluctuations [42]. According to the capillary wave model, the thermally excited motion of a molecule near the free surface can schematically be presented as shown in Fig. 6.2. This movement results in a wave-like distortion of the

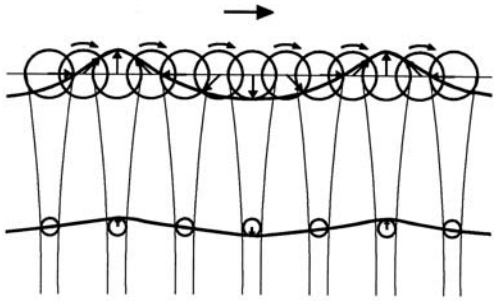

Figure 6.2: Sketch of capillary waves motion at the soft mater surface. As indicated by the size of the circles, the amplitude of the CW decreases exponentially with depth. Figure taken from [42].

surface with an amplitude much smaller than its wavelength. Within the frame of hydrodynamics the velocity potential ϕ[1] in the (x,y) plane of the

[1]The velocity of the molecule is given by $v(\vec{x}, z) = \nabla\phi(x, z)$

capillary waves of frequency ω is given by

$$\phi(x,z) = \phi_0 \exp(-qz)\cos[q_x x - \omega(q_x)t]. \tag{6.1}$$

It is basically a monochromatic wave, which is damped exponentially with the distance z from the surface. The most general way to describe the surface roughness is by introducing a height-height correlation function

$$C(\vec{R}) = \langle z(\vec{r}_{||})z(\vec{r}_{||} + \vec{R})\rangle_{\vec{r}_{||}} \tag{6.2}$$

where $\vec{R}$ is a lateral vector and $\vec{r}_{||}$ defines the point in the (X,Y) plane with corresponding value of $z(\vec{r}_{||})$. In the reciprocal space the eq. 6.2 is given by

$$C(\vec{q}) = FT\{C(\vec{R})\} = \frac{k_B T}{4\pi^2}\frac{1}{q_{||}^2 + q_{l,c}^2}, \tag{6.3}$$

where $q_{||}$ is the wavevector transfer parallel to the surface and $q_{l,c}$ stands for the wavevector cutoff[2]. For x-ray reflectivity experiments $q_{l,c} = q_z \Delta\alpha_f/2$ [42]. Each mode of capillary waves is defined by the wavevector k and complex frequency $f = \omega_c + i\Gamma$ [54, 55]. Depending on the damping strength, two extreme cases of capillary waves can be distinguished. In the low damping limit (low viscosity) the waves are free to propagate with

$$f = k^{\frac{3}{2}}\sqrt{\gamma/\rho} + i\frac{2\eta k^2}{\rho}. \tag{6.4}$$

In the high damping regime, f reduces to its imaginary part only

$$f = i\gamma k/(2\eta). \tag{6.5}$$

6.4 The Jäckle - Kawasaki model

The statistical properties of fluctuating soft matter surface are determined by the probability of the excitation of different modes. The power spectrum of those fluctuations can be calculated within the linear response theory. If weak external forces are assumed, the displacement of the liquid/vapor interface due to an external force $F_z(k,t) = F_{z,0}\exp[-i(\omega t - kx)]$ is given by

$$u_z(k,t) = F_z(k,t)\cdot\chi(k,w) = u_{z,0}\exp[-i(\omega t - kx)]. \tag{6.6}$$

The imaginary part of the dynamic susceptibility $\chi'' = Im(\chi(k,\omega))$ determines the power spectrum $S(\omega,k)$ of the thermal height fluctuations of the interface via the fluctuation-dissipation theorem

$$S(\omega,k) = 2k_B T\chi''(k,\omega)/\omega. \tag{6.7}$$

[2]The influence of the gravity has been neglected.

For incompressible liquids $\chi(k,\omega)$ has the following form [56]

$$\chi(k,\omega) = \frac{k/\rho}{(\gamma/\rho)k^3 - (\omega + i2\nu(\omega)k^2)^2 - 4\nu^2(\omega)k^4\sqrt{1 - i\omega/\nu(\omega)k^2}}. \quad (6.8)$$

$\nu(\omega) = \eta(\omega)/\rho$ is the kinematic viscosity. Denoting the denominator in eq. 6.8 by $D(\omega,k)$ the dynamic structure factor $S(\omega,k)$ can be expressed as

$$S(\omega,k) = -2k_BT\frac{k}{\rho\omega}\frac{ImD(k,\omega)}{|D(k,\omega)|^2}. \quad (6.9)$$

Fig. 6.3 illustrates the power spectrum calculated using eq. 6.9 for a dibutyl phthalate surface at 295 K. At larger length scales (k=1...2.5×10^{-6} Å^{-1}) propagating capillary wave determine the dynamics of the interface. The peak position in $S(\omega,k)$ corresponds to the frequency $\omega_c = k^{\frac{3}{2}}\sqrt{\gamma/\rho}$ of those waves. For larger k capillary waves become overdamped, $S(\omega,k)$ becomes quasielastic broad and centered around the $\omega_c = 0$. The transition from one regime to the other takes place at the critical wave vector [57]

$$k_c = \frac{4\gamma\rho}{5\eta^2}. \quad (6.10)$$

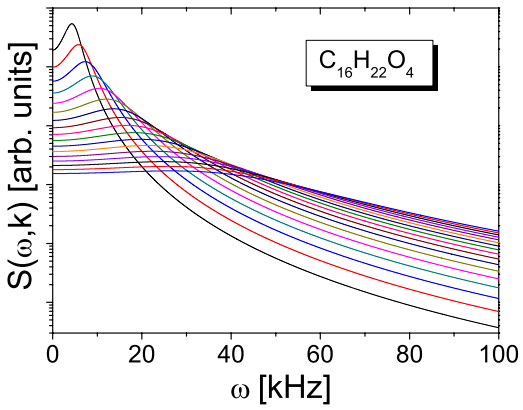

Figure 6.3: The dynamic structure factor $S(\omega,k)$ calculated at k=1, 1.25, 1.5,..., 5×10^{-6}Å^{-1} (top to bottom) for dibutyl phthalate at room temperature.

6.5 The viscoelastic effect

A short introduction to viscoelasticity is given in this subsection. The theoretical description of the Maxwell, the Kelvin-Voigt, and the standard linear

solid model, presented below, is based on the work of W. Flügge [58] and the nomenclature used comes from this book.
Circuits built from two kinds of discrete elements serve as mathematical models of the behavior of the viscoelastic materials under applied uni-axial stress. Those elements are: a spring (representing elastic properties) and a dashpot (describing viscous flow). Assuming a linear response, Hook's law relates the level of strain ε to the applied stress σ

$$\sigma = E\varepsilon, \tag{6.11}$$

while for the case of the dashpot the strain is proportional to the elongation rate $\dot{\varepsilon}$

$$\sigma = F\dot{\varepsilon}. \tag{6.12}$$

Young's modulus E and the spring constant F are used to describe the viscoelastic properties of materials. The simplest viscoelastic model consists of a single pair of spring and dashpot. Depending on the configuration of those components, two basic concepts of viscoelasticity of liquids have been proposed: the Maxwell and the Kelvin-Voigt model.

6.5.1 Maxwell model

In the Maxwell model, a spring and dashpot are connected in series, as shown in Fig. 6.4. This means that the total elongation ε is given by

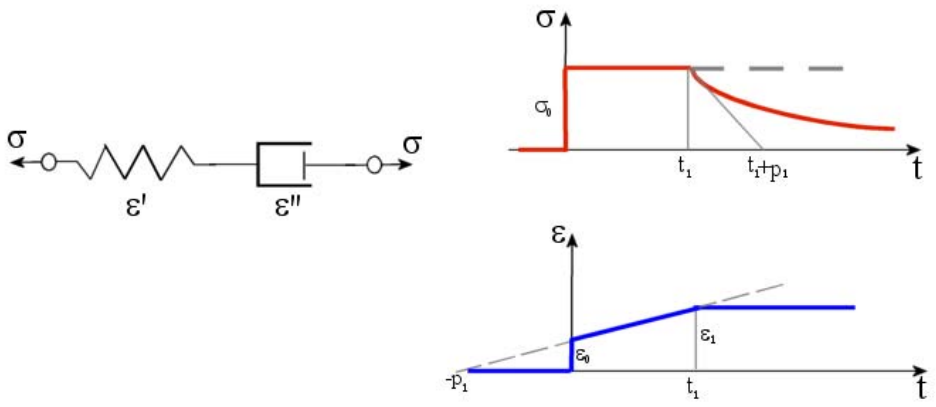

Figure 6.4: The Maxwell model: graphical representation (left) and evolution of ε and σ in creep and relaxation phases (right). Figure taken from [58].

$$\varepsilon = \varepsilon' + \varepsilon''. \tag{6.13}$$

Inserting equations 6.11 and 6.12 into relation 6.13 results in the differential equation

$$\sigma + p_1\dot{\sigma} = q_1\dot{\varepsilon}, \tag{6.14}$$

where $p_1 = F/E$ and $q_1 = F$. The response of a high viscosity liquid to an external force, in the frame of Maxwell theory, consists of two stages. First, at time $t = 0$ it is elastically deformed due to exerted constant stress. When the deformation ceases at $t = t_1$, the residual shear stresses decay in the course of time, so eventually no internal stress is present in the liquid. Those two processes are represented by the two solutions of eq. 6.14

$$\varepsilon = \frac{\sigma_0}{q_1}(p_1 + t) \quad 0 < t < t_1 \tag{6.15}$$

$$\sigma = \sigma_0 \exp[-(t - t_1)/p_1] \quad t > t_1. \tag{6.16}$$

The time evolution of strain and stress is shown in Fig. 6.4 .

6.5.2 Kelvin-Voigt model

The Kelvin-Voigt model gives another concept of the viscoelastic behavior of matter. It can be visualized by a parallel connection of spring and dashpot (Fig. 6.5). An external force causes equal elongation of those two elements,

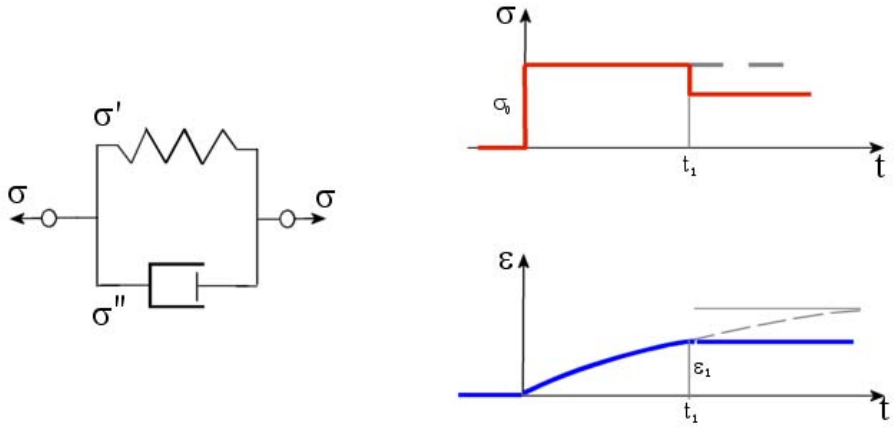

Figure 6.5: The Kelvin-Voigt model: graphical representation (left) and evolution of ε and σ in creep and relaxation phases (right). Figure taken from [58].

so the system can be described by the following equation

$$\sigma = q_0\varepsilon + q_1\dot{\varepsilon}. \tag{6.17}$$

An initial stress σ_0 at $t = 0$ causes a gradual increase of the strain from 0 to ε_1, which then stays constant in the relaxation phase ($t > t_1$).

For fixed strain, partial relaxation of σ_0 takes place at times $t > t_1$. However, there is a residual stress always present in the medium (see Fig. 6.5). This mechanism is described by the following formulas

$$\varepsilon = \frac{\sigma_0}{q_0}(1 - \exp(-\lambda t)) \quad 0 < t < t_1 \tag{6.18}$$

$$\sigma = \sigma_0(1 - \exp(-\lambda t_1)) \quad t > t_1, \tag{6.19}$$

where $\lambda = q_0/q_1$.

6.5.3 Standard linear material

A more sophisticated model of the properties of a real viscoelastic solid or liquid is the three-parameter model (see Fig. 6.6), known also as standard linear material. Starting from

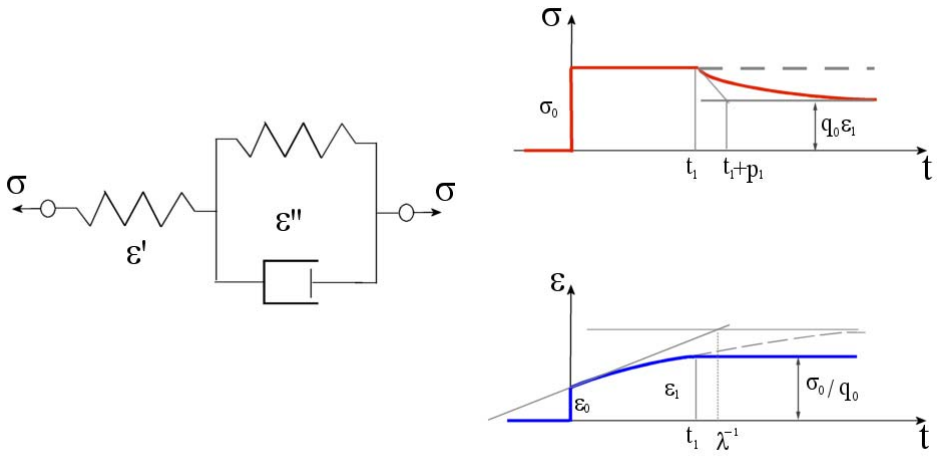

Figure 6.6: The standard linear model: graphical representation (left) and evolution of ε and σ in creep and relaxation phases (right). Figure taken from [58].

$$\sigma = E\varepsilon' \tag{6.20}$$

$$\sigma = q_0''\varepsilon'' + q_1''\dot{\varepsilon}'', \tag{6.21}$$

this system can be described by

$$\sigma + p_1\dot{\sigma} = q_0\varepsilon + q_1\dot{\varepsilon}, \tag{6.22}$$

where $p_1 = q_1''/(E + q_0'')$, $q_0 = Eq_0''/(E + q_0'')$, and $q_1 = Eq_1''/(E + q_0'')$. Such material in the creep phase ($t < t_1$) posses an instant elasticity $\varepsilon_0 = \sigma_0/E_0$,

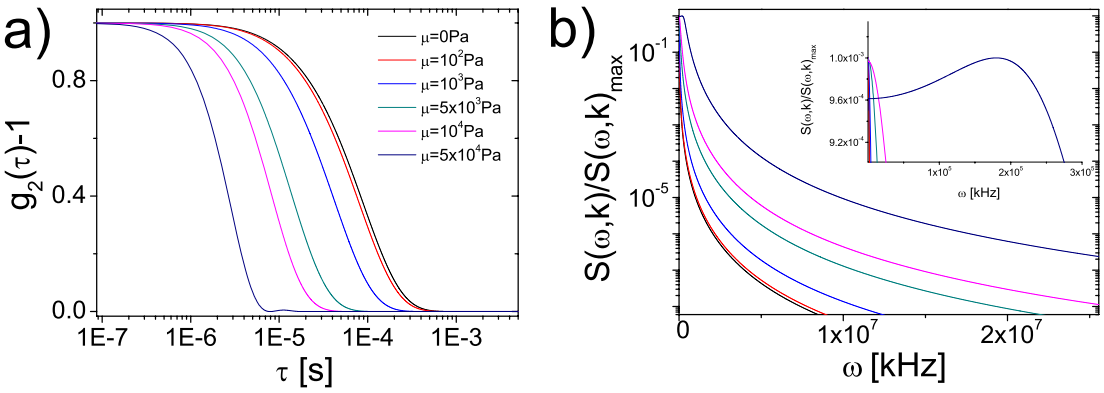

Figure 6.7: a) The intensity autocorrelation functions of a Voigt-Kelvin liquid calculated for $k = 5 \times 10^{-6}$ Å^{-1}, T=260 K, $\rho = 1.055$ g/cm^3, $\sigma = 37 \times 10^{-3}$ N/m, and different shear moduli $\mu = 0, 1 \times 10^2, 1 \times 10^3, 5 \times 10^3, 1 \times 10^4, 5 \times 10^4$ Pa, and b) corresponding dynamic structure factors $S(\omega, k)$. Inset: Low frequency part of $S(\omega, k)$.

which increases to an asymptotic value $\varepsilon(\infty) = \sigma_0/E_\infty$ under applied stress

$$\varepsilon = \frac{\sigma_0}{q_0}[1 - (1 - \frac{p_1 q_0}{q_1})] \exp(-q_0 t/q_1). \tag{6.23}$$

In the relaxation phase ($t < t_1$) the medium gradually reduces the stress to $\sigma_\infty = E_\infty \varepsilon_1$

$$\sigma = q_0 \varepsilon_0 [1 - \exp(-\tau/p_1)] + \sigma_0 \exp(-\tau/p_1). \tag{6.24}$$

6.6 Viscoelasticity near the liquid/vapor interface

A detailed theoretical study of the surface modes in polymer solutions and polymer gels in the limit of strong coupling has been given by Harden et al. [59]. In this approach the polymer network is treated as a continuous elastic medium diluted in the Newtonian solvent. Depending on the relaxation time, the Maxwell and the Kelvin-Voigt models were considered. As presented in Fig. 6.7, the elasticity of the liquid is reflected by the change of the dynamic structure factor $S(\omega, k)$ and the corresponding intensity autocorrelation functions. Beside the peak at the capillary waves frequency ω_c also the maximum positioned at the Rayleigh waves frequency is present.

Both types of waves follow different dispersion relations. The frequency ω of the elastic waves is proportional to the wavevector k and, in case of the capillary waves, $\omega_c \propto k^{\frac{3}{2}}$ holds. For the viscoelastic liquids, the $\{k, \mu_0\}$-plane can be

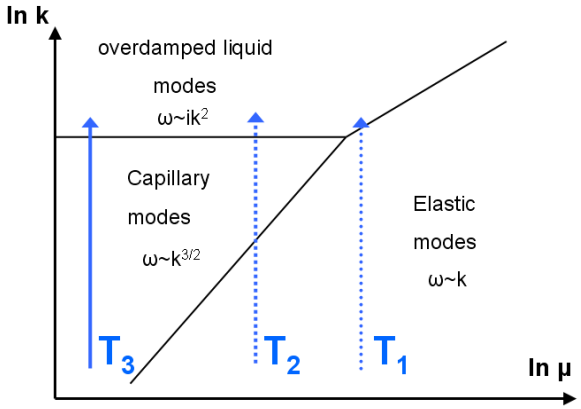

Figure 6.8: Surface mode diagram for viscoelastic glass former showing regions of capillary, Rayleigh elastic, and overdamped liquid modes. The arrows indicates the situation met during the x-ray photon correlation spectroscopy experiment for measurement performed at different temperature $T_3 > T_2 > T_1$.

divided into several distinct regions: propagating capillary waves, overdamped waves and Rayleigh waves (see Fig. 6.8). The transition between those modes has been studied theoretically and experimentally [60, 61]. The viscoelastic effect has been investigated also for a large number of non-polymeric liquids. For example, the high frequency limit of the shear modulus for butanediol, 2-methyl-pentanediol, hexanetriol, and glycerol has been determined by Meister at al. [62]. For all of those compounds a linear temperature dependence of μ_∞ at temperatures far above the glass transition has been reported. However, it was proofed in [27] that the elasticity of bulk organic liquids at room temperature is not restricted to the high frequency limit only. The elastic behavior of a large number of liquids was observed by mean of acoustic measurements for the frequency of the external shear force f=40 kHz [27].

6.6.1 X-ray photon correlation spectroscopy

X-ray photon correlation spectroscopy (XPCS) is a well-established technique used to study slow dynamics in soft matter systems [63, 64]. The principles of XPCS have been "borrowed" from the dynamic light scattering (DLS) technique [65]. The substitution of the laser light by x-rays opens new experimental possibilities like studies of opaque media, is well-suited for the surface-sensitive measurements, and allows tracking the dynamics at smaller length-scales in comparison to DLS experiment. A simplified picture of grazing-incidence x-ray photon correlation spectroscopy is illustrated in Fig. 6.9. Partially coherent radiation impinges on the investigated surface at a shallow angle smaller than the critical value for the total external reflection $\alpha_i < \alpha_c$. The volume probed by the incident beam is in such case defined by the penetration depth Λ of the

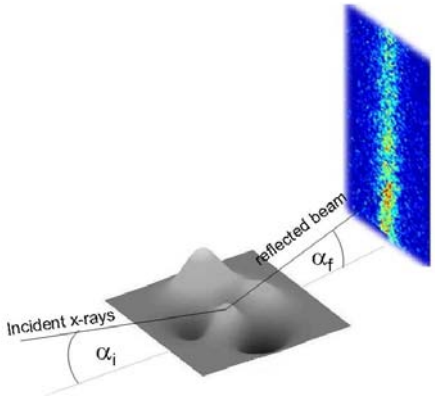

Figure 6.9: Principle of a surface sensitive XPCS experiment.

evanescent wave into the studied specimen. For most organic surfaces exposed to the low energy x-rays Λ is around 100 Å. Photons scattered by the fluctuating surface produce time dependent speckle pattern in the detector plane. The temporal variation of the interference image directly reflects the fluctuations of the specimen under investigation. The quantitative description of the sample evolution is then obtained by measuring the characteristic time of the speckles intensity modulation. Mathematically this is expressed by means of the normalized intensity-intensity autocorrelation function [66]

$$g_2(\tau, q_{||}) = \frac{\langle I(t, q_{||}) I(t+\tau, q_{||}) \rangle}{\langle I(t, q_{||}) \rangle^2} \qquad t > 0, \tag{6.25}$$

where $I(t, q_{||})$ is the intensity at the momentum transfer $q_{||}$ at time t. An average over the time is denoted by the brackets $\langle ... \rangle$. The dimensions of the incident beam define the scattering volume, while the transverse ξ_t and longitudinal ξ_l coherence length determines the coherence volume. The interference occurs only within a particular coherence volume but not between neighboring ones. In the optimum case, the scattering volume should match the coherence volume. Due to the limited penetration depth only the dynamics of the liquid/vapor interface is probed for α_i smaller than critical angle of total external reflection α_c. In the case when the fluctuations of the electric fields $E(t, q_{||})$ follow a Gaussian statistic with a mean value equal to zero, the Siegert relation [66] holds

$$g_2(\tau, q_{||}) = 1 + g_0 |g_1(\tau, q_{||})|^2 \tag{6.26}$$

where the intermediate scattering function is defined as

$$g_1(\tau, q_{||}) = \frac{G_1(\tau, q_{||})}{\langle E(t, q_{||}) \rangle^2} = \frac{\langle E^*(t, q_{||}) E(t+\tau, q_{||}) \rangle}{\langle E(t, q_{||}) \rangle^2} \qquad t > 0. \tag{6.27}$$

The degree of coherence is described by the prefactor g_0 [67]. $G_1(\tau, q_{||})$ is proportional to the height correlation of the investigated surface $C(\tau, q_{||})$, which is the Fourier transform of the dynamic structure factor

$$C(\tau, q_{||}) = \int_0^\infty S(\omega, q_{||}) e^{i\omega\tau} d\omega. \tag{6.28}$$

For low viscosity liquids, the capillary wave model predicts the presence of propagating waves, with

$$S(\omega, q_{||}) = (\pi\Gamma_0[1 + (\frac{\omega - \omega_c}{\Gamma_0})^2])^{-1}. \tag{6.29}$$

The height-height correlation function can then be expressed in terms of the damping constant Γ_0 and propagation frequency $\omega_c = \sqrt{\gamma/\varrho} q_{||}^{3/2}$

$$C(\tau, q_{||}) = cos(\omega_c\tau) \exp(-\Gamma_0\tau) \tag{6.30}$$

with

$$\Gamma_0 = 2\eta q_{||}^2/\rho. \tag{6.31}$$

The normalized intensity autocorrelation function $g_2(\tau, q_{||})$ can be approximated by

$$g_2(\tau, q_{||}) = 1 + g_0 \cos^2(\omega_c\tau) \exp(-2\Gamma_0\tau). \tag{6.32}$$

For the overdamped capillary waves the normalized intensity-intensity autocorrelation function is given by

$$g_2(\tau, q_{||}) = 1 + g_0 \exp(-2\Gamma_0\tau), \tag{6.33}$$

where

$$\Gamma_0 = \gamma q_{||}/(2\eta). \tag{6.34}$$

The dynamics of the surface modes is described by means of the dispersion relation $\Gamma_0^{-1}(q_{||})$. The capillary wave model predicts a linear relationship between Γ_0^{-1} and the wavevector transfer $q_{||}$ (eq. 6.33). When elastic waves are present at the studied surface $\Gamma_0^{-1}(q_{||})$ takes a more complicated form, because of the impact of the shear modulus μ on the frequency of the excited modes. The viscoelastic theory, based on the Maxwell model, predicts a dispersion relation to be described by [56]

$$\Gamma_0(q_{||}, T) = \frac{\gamma(T)}{2\eta(T)} \frac{1}{1 + \frac{\gamma(T) q_{||}}{2\mu_\infty}} q_{||}. \tag{6.35}$$

When the Kelvin-Voigt model is considered, the damping constant is expressed as [68]

$$\Gamma_0(q_{||}, T) = \frac{\gamma(T)}{2\eta(T)} (q_{||} + \frac{\mu(T)}{\gamma(T)}). \tag{6.36}$$

6.6.2 Resolution effects

In practice, due to the effects of the partial coherence, the correlation function recorded during XPCS measurements are convoluted with the resolution function $\Xi(q)$ of the experimental setup. The rigorous calculations of the resolution function described by Gutt et al. [69] yield the following expression for the experimentally accessible correlation function

$$g_2(\tau, q) = 1 + \frac{\int\int dq' dq'' \tilde{C}_{\rho\rho}(\tau, q') \tilde{C}_{\rho\rho}(\tau, q'') F(q, q', q'')}{(\int dq \tilde{C}_{\rho\rho(0,q')} H(q, q'))^2}, \tag{6.37}$$

where the $\tilde{C}_{\rho\rho}(\tau, q)$ denotes the Fourier transform of the electron density function, $F(q, q', q'')$ and $H(q, q')$ are generalized resolution functions.
$F(q, q', q'')$ and $H(q, q')$ are functions of the coherent properties of the incident radiation, the optics used to monochromatize and focus the beam, and the detector resolution. Often, a simplified approach is used to take account the finite spread in Δq within the collected data. The autocorrelation function is then given by

$$g_2(\tau, q_{||}) \propto |\Re(q_{||}) + \frac{k_B T}{\gamma} \int_0^\infty d^2 q'_{||} g_1(q'_{||}, \tau) \Xi(q'_{||} - q_{||})|^2. \tag{6.38}$$

The term $\Re(q_{||})$ describes the finite dimensions of the specular beam, while the distribution of $q_{||}$ "seen" by the detector is represented by the function $\Xi(q_{||})$. The problem of modeling $\Re(q_{||})$ and $\Xi(q_{||}$ has been addressed by several authors [63, 70, 42]. Often both functions are assumed to have a Gaussian shape.

6.7 Experiment details

6.7.1 Beamline ID10A

The XPCS experiment was performed at the beamline ID10A (TROIKA I) at the European Synchrotron Radiation Facility (ESRF). The layout of the

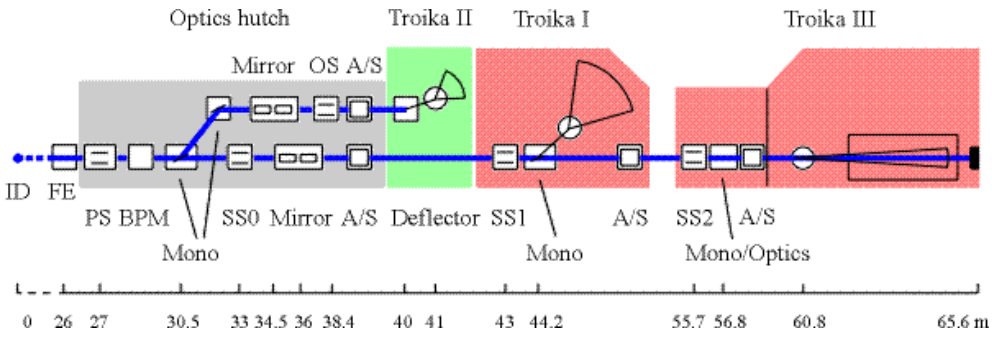

Figure 6.10: Layout of the Troika beamlines at the ESRF. Figure taken from *www.esrf.eu/UsersAndScience/Experiments/SCMatter/ID10A/*.

optical and experimental hutches is presented in Fig. 6.10. Before entering the experimental hutch, the radiation provided by a series of three undulators passes through the primary slits PS, beam position monitor BPM, secondary slits SS0, SS1 and a monochromator. The Si(111) crystals were used to select a 8 keV radiation out of the accessible x-rays energy range (7.5 keV up to 20 keV). The energy bandpass $\Delta\lambda/\lambda = 1.4 \times 10^{-4}$ leads to the longitudinal coherence length $\xi_l \approx 1\mu$m. A schematics of the experimental setup is shown in Fig. 6.11. The typical coherent intensity is on level of 10^{10}photon per 20μm pinhole (for 100 mA ring current). The incoming radiation with a transverse coherence length $\xi_t \approx 10\mu$m is deflected by the mirror M and hits the liquid surface at an angle α_i smaller than the critical angle α_c. The pinhole P ($10\mu m \times 10\mu m$) reduces the incident beamsize to the value corresponding to ξ_t. The Fraunhofer fringes from P are suppressed by guardslits GS set to $300\mu m \times 300\mu m$. The cryostat was mounted on the standard translation stage supporting the movement of the chamber in x, y, and z direction. The scattered signal was recorded with two detectors alternatively: Cyberstar and CCD camera. The point detection scheme is well-suited for investigations of the fast dynamics with characteristic times much shorter than 1s. The resolution in $q_{||}$-space is defined by the opening of the slits DS positioned in front of the detector. The $g_2(\tau, q_{||})$ function is, in this case, provided by the hardware autocorrelator device. The drawback of this setup is that during each measurement the intensity at only one wavevector transfer can be collected. In practice, this factor limits the number of recorded $g_2(\tau, q_{||})$ functions(and consequently the statistic) due to finite duration of the experiment.
Upon approaching the glass transition temperature the dynamics of the investigated system slows down considerably and the relaxation times τ_{relax} of the surface fluctuations enter the long timescale regime ($\tau_{relax} \gg 1$ s). In this case, the efficiency of the data acquisition can be improved by using a 2D detector. The CCD camera allows the simultaneous collection of the scattered photons in a wide range of $q_{||}$. The readout time($\Delta t = 0.73$ s) after each exposure defines the shortest detectable delay time τ, which can be used for

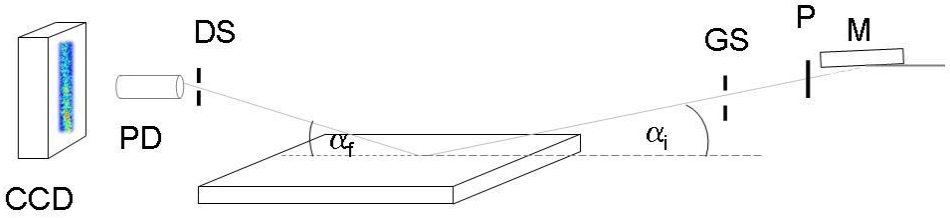

Figure 6.11: The schematic layout of the XPCS setup: P-pinhole, GS- guardslits, DS-detector slits, PD-point detector.

off-line computation of the intensity autocorrelation functions.

6.7.2 The sample environment

The liquid sample cryostat in the standard configuration has been used during the experiment at ID10A. A 0.3 mm deep Cu plate was used as a sample holder for pure dibutyl phthalate and squalane. The pressures inside the inner and outer chambers were kept at around 1 mbar and 10^{-2} mbar, respectively. The temperature of the liquid was tuned from 295 K to 186 K with an average cooling rate of 0.3 K/min. To equilibrate the sample environment, after approaching each desired temperature the setup was kept for 1h at given conditions before starting the measurements. To minimize the probability of radiation damage, the sample was translated in direction perpendicular to the scattering plane after every scan and a fresh area of the specimen was exposed to x-rays.

6.7.3 Data treatment

In the point detection scheme, the fluctuations of the reflected intensity are correlated automatically by the autocorrelator connected to the detector. When the CCD camera is used, the $g_2(\tau, q_{||})$ function must be calculated from a series of images equally spaced in time by the Δt. Each image provides a 2D distribution of the diffuse signal at times $t_i = i \times \Delta t$. A typical CCD picture is shown in Fig. 6.12. The $g_2(\tau, q_{||})$ function is obtained by correlating

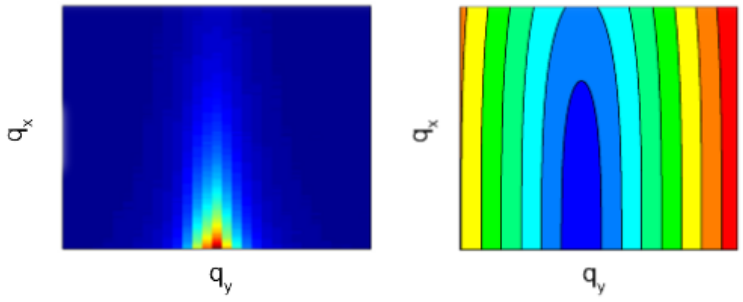

Figure 6.12: Example of a CCD image recorded at 205 K (left) and the distribution of $q_{||} = \sqrt{q_x^2 + q_y^2}$ values in the detector plane (right). For clarity, the whole range of $q_{||}$ has been divided into eight regions, marked by different colors.

the intensities at discrete times (frames) at selected values in $q_{||}$-space. Data have been evaluated according to the recipe given in [71]. To improve the

quality of the correlation functions, each CCD image has been divided into 3×3 pixel areas and an averaged intensity from each of those sub-regions has been processed by in-house developed Matlab routines. All the intensity autocorrelation functions have been normalized using a symmetric normalization scheme. For a given number of time lags N and delay times τ, it makes use of the two partially independent time averages

$$\langle I(\tau, q_{||})_{left} \rangle = \frac{1}{N-\tau} \sum_{n=1}^{N-\tau} I(n, q_{||}) I(n+\tau, q_{||}) \tag{6.39}$$

and

$$\langle I(\tau, q_{||})_{right} \rangle = \frac{1}{N-\tau} \sum_{n=\tau+1}^{N} I(n, q_{||}) I(n+\tau, q_{||}) \tag{6.40}$$

to normalize the temporal intensity autocorrelation function $G_2(\tau, q_{||})$

$$g_2(\tau, q_{||}) = \frac{G_2(\tau, q_{||})}{\langle I(\tau, q_{||})_{left} \rangle \langle I(\tau, q_{||})_{right} \rangle}. \tag{6.41}$$

The level of the electronic noise was estimated by recording a series of images without exposing the sample to the x-rays.
The randomness of the incident radiation intensity fluctuations has been proofed by correlating the signal from the beam monitor mounted upstream of the cryostat.
All the point detector and the CCD data sets were fitted with the following formula

$$g_2(\tau, q_{||}) = g_0 \exp(-2(\tau/\tau_0)^{\beta}) + 1 \quad \beta \leq 1, \tag{6.42}$$

where g_0 is the contrast, describing the degree of coherence, τ_0 is the characteristic time constant, and β is the Kohlrausch stretching parameter.
The reproducibility of the obtained results and possibility of radiation damage were tested by collecting series of $g_2(\tau, q_{||})$ functions at the same spot on the surface. Within the detection limit, the dibutyl phthalate surface was confirmed to be unaffected by the incident radiation. Two consecutive autocorrelation functions recorded at 205 K are shown in Fig. 6.13. Beside the noise at larger times, both curves are indistinguishable.

6.8 Results

According to the prediction of the capillary wave model, in the experimentally accessible q_x range the transition from propagating to overdamped waves is expected to take place on the surface of dibutyl phthalate at room temperature (see Fig. 6.3). However, the shape of the recorded autocorrelation functions deviates significantly from the theoretical predictions. The explanation for this discrepancy is the finite resolution of the experimental setup. As described in

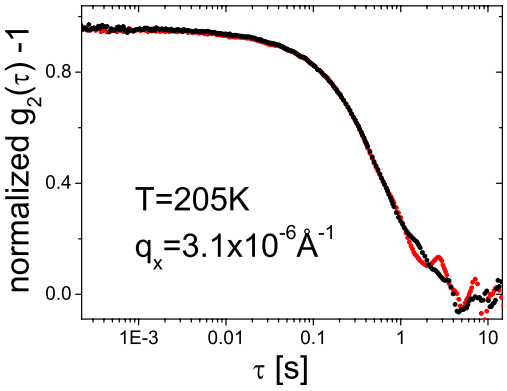

Figure 6.13: Two intensity autocorrelation functions collected at 205 K at a fixed spot at the dibutyl phthalate surface. For sake of convenience, the contrast for both function was normalized to 1.

the introduction, an estimate of the experimental resolution can be obtained by convoluting the simulated correlation function with the Gaussian resolution function $\Xi(q_{||})$ (eq. 6.38). The shapes of all data sets collected at 295 K can be reproduced assuming wavevector spreads of the order of 10^{-7}Å^{-1} in q_x and 10^{-5}Å^{-1} in q_y (see Fig. 6.14 and Fig. 6.15).

In general, the shape of the intensity autocorrelation function was empirically found to be more affected by resolution effects for the low viscosity η and high surface tension γ liquids [54] than in case of high-η and low-γ samples [72]. The observed position and the width of the propagating capillary waves peak in the dynamic structure factor $S(\omega, k)$ spectrum are very sensitive to the finite experimental resolution, while the broad feature centered at $\omega = 0$ describing the overdamped waves (see Fig. 6.7) is far more "robust". At temperatures lower than 295 K the viscosity η of dibutyl phthalate is high enough to prevent the capillary waves from propagating on the surface and on that basis the experimental resolution was assumed to introduce only minor effects on collected data and was consequently not taken into account during further analysis.
If the value of the viscosity $\eta(T)$ in the bulk and at the surface of dibutyl phthalate would be comparable, only overdamped capillary waves should be present at the liquid/vapor interface of dibutyl phthalate at temperatures lower than 295 K. The high contrast g_0 and the lack of oscillations in $g_2(\tau, q_x)$ support the picture of the strong damping of the surface modes. The assumption of equality of $\eta(T)$ in the bulk and at the surface has been used only to estimate the type of fluctuations present at the liquid/vapor interface at lower temperatures. Otherwise, the viscosity was left as a free parameter during the data

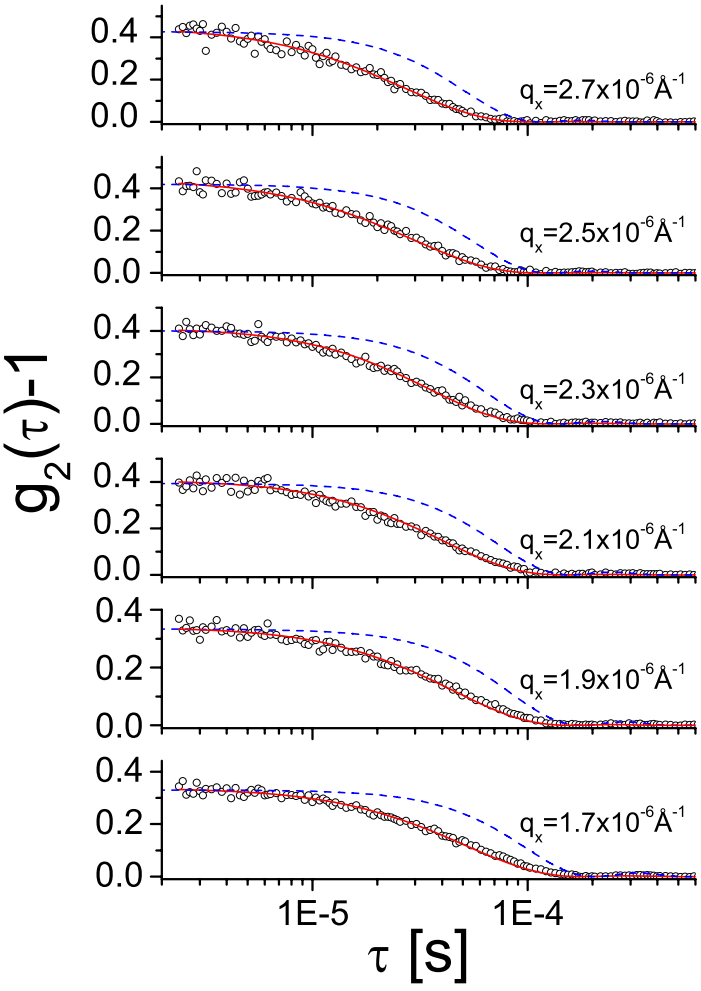

Figure 6.14: Intensity autocorrelation functions $g_2(\tau, q_x)$ recorded on the surface of dibutyl phthalate at 295 K for detector slits opening $30\mu m \times 30\mu m$. Experimental data ($\circ$) are compared with the calculated curves assuming perfect instrumental resolution (dashed lines) and the finite resolution of the experimental setup (solid line).

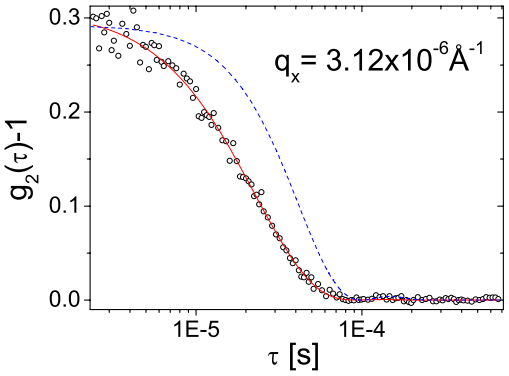

Figure 6.15: Intensity autocorrelation function $g_2(\tau, q_x)$ recorded on the surface of dibutyl phthalate at $q_x = 3.12\text{Å}^{-1}$ at 295 K for the detector slits opening $50\mu m \times 50\mu m$. Experimental data ($\circ$) are compared with the calculated curves assuming perfect instrumental resolution (dashed lines)and the finite resolution of the experimental setup.

fitting procedure.

From an inspection of the intensity autocorrelation functions a rapid slowing down of the surface fluctuations in the applied temperature range is apparent, reflecting the dramatic increase of the viscosity η. Close to T_g the relaxation time of the dibutyl phthalate surface exceeds the time-scale suitable for the point detection scheme. The slow fluctuations ($\tau > 1s$) of the liquid/vapor interface were investigated using the CCD camera. These measurements were performed in the following temperature sequence 192 K, 189 K, and 186 K. The influence of the thermal history on the surface dynamics of dibutyl phthalate was investigated by performing two additional measurements (for sample heated up from 186 K) at 195 K and 220 K, using the CCD and the point detector, respectively. Unfortunately, because of a too high intensity of the

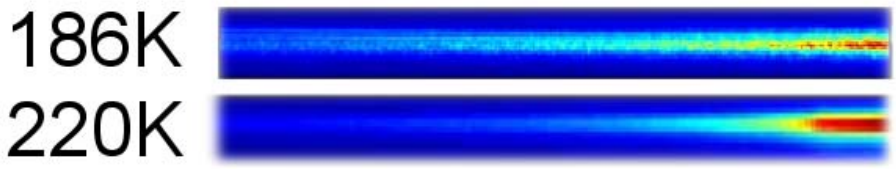

Figure 6.16: Integrated CCD images collected at 186 K (10200 frames) and 220 K (500 frames). Time interval between two consecutive frames $\Delta t = 0.73\ s$.

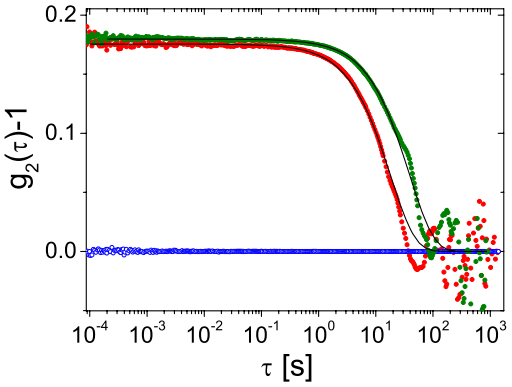

Figure 6.17: The intensity autocorrelation functions collected at the surface of dibutyl phthalate at 192 K at $q_x = 2.7 \times 10^{-6}$Å^{-1} (green), $q_x = 7.2 \times 10^{-6}$Å^{-1}(*red*) together with the autocorrelation function of the beam monitor signal (blue).

speckles close to the specular position, it was impossible to collect the speckle pattern in the same q_x range as with the point detector and the time evolution of the scattered intensity at much higher q_x was investigated. The 2D distribution of the intensity within the speckle pattern (see Fig.6.16) is consistent with the theoretical description of grazing incidence XPCS [63] and with data reported for other soft matter surfaces [73, 41]. The small q_y range, in which the speckles can be observed, reflects the smoothness of the irradiated surface on small lateral length-scales.

Complementary to the CCD measurements, the intensity autocorrelation functions were collected with the NaI detector at smaller wavevector q_x at 192 K (see Fig.6.17). Already at 192 K, the time constant of the relaxation process at μm length scales approaches the 100 s border used to define the glass transition temperature. It is apparent that the acquisition time of 1000 s was not sufficient to collect the good quality correlation functions allowing a reliable fit and only a rough estimate for the relaxation times of $\Gamma^{-1} = 33$ s at $q_x = 7.2 \times 10^{-6}$Å^{-1} and $\Gamma^{-1} = 76$ s at $q_x = 2.7 \times 10^{-6}$Å^{-1} could be obtained. Even for relaxation times exceeding 300 s, the intensity autocorrelation functions decay to zero. At μm length-scale dibutyl phthalate does not exhibit an ergodic to non-ergodic transition at temperatures down to 186K. This clearly shows that the definition of the glass transition T_g as the temperature, at which the relaxation time exeeds 100 s is not applicable to the collected data. The normalized intensity autocorrelation function $g_2(\tau, q_x)$ collected with the point detector and the CCD camera were fitted using eq. 6.42 for $\beta = 1$. Deviation from the simple exponential decay have been observed for all data

Table 6.1: Values of the viscosity and the shear modulus obtained from fits of the XPCS data using the Kelvin-Voigt model.

	Kelvin - Voigt model	Maxwell model
T [K]	η [Pas]	μ [Pa]
260	$1.0 \times 10^{-1} \pm 1.0 \times 10^{-3}$	$5.5 \times 10^{1} \pm 4.7 \times 10^{0}$
240	$1.2 \times 10^{0} \pm 1.0 \times 10^{-2}$	$8.7 \times 10^{1} \pm 7.0 \times 10^{0}$
220	$3.3 \times 10^{1} \pm 7.0 \times 10^{-1}$	$1.5 \times 10^{2} \pm 1.4 \times 10^{1}$
215	$1.3 \times 10^{2} \pm 4.7 \times 10^{0}$	$3.0 \times 10^{2} \pm 2.8 \times 10^{1}$
210	$5.2 \times 10^{2} \pm 4.8 \times 10^{1}$	$2.4 \times 10^{2} \pm 6.5 \times 10^{2}$
205	$2.1 \times 10^{3} \pm 5.5 \times 10^{1}$	$6.1 \times 10^{2} \pm 3.3 \times 10^{2}$
195	$1.1 \times 10^{5} \pm 2.1 \times 10^{3}$	$6.4 \times 10^{3} \pm 2.1 \times 10^{2}$
192	$6.6 \times 10^{5} \pm 1.7 \times 10^{4}$	$4.3 \times 10^{3} \pm 2.7 \times 10^{2}$
189	$4.1 \times 10^{6} \pm 2.3 \times 10^{5}$	$1.3 \times 10^{4} \pm 1.4 \times 10^{3}$
186	$7.0 \times 10^{7} \pm 1.0 \times 10^{7}$	$6.1 \times 10^{4} \pm 1.1 \times 10^{4}$

sets. Satisfactory fits were obtained, when the stretched exponential scheme was applied. As an example, the outcomes of the fitting routine for the single and stretched exponential relaxation models for the data collected at 260 K are compared in Fig. 6.18a. A systematic increase of the stretching exponent was observed only for data collected at 260 K, 240 K, and 220 K (see Fig. 6.18b). At lower temperatures β oscillates in random manner between 0.85 and 1. The decrease in the signal to noise ratio for the data measured below 220 K broadens the uncertainty intervals of the estimated Kohlrausch exponents. The selected intensity autocorrelation functions collected in the temperature range $186\ K \leq T \leq 260\ K$ together with corresponding fits are presented in Fig. 6.19 to Fig. 6.20. The remaining data sets are included in the appendix.

The insight into the change of the dynamics of the surface modes upon approaching the glass transition has been gained from the analysis of their dispersion relation $\Gamma^{-1}(q_x)$ (see Fig. 6.21) at lowered temperatures. Already at 260 K the characteristic time Γ^{-1} does not decay in linear manner as a function of the wavevector transfer q_x, as it is predicted by the capillary wave CW model, but exhibits much weaker dependence on q_x with decreasing the wavevector transfer being characteristic for the elastic surface waves. The discrepancy between experimental results and the CW picture becomes more pronounced at lower temperatures. The well-marked crossover from the Rayleigh-type modes at small q_x ($q_x < 1 \times 10^{-5}\text{Å}^{-1}$) into the capillary waves ($q_x > 1 \times 10^{-5}\text{Å}^{-1}$) at larger wavevector transfers q_x was observed for data set collected at 195 K. For all temperatures the viscoelasticity of the surface of dibutyl phthalate is described by the Kelvin-Voigt model.

The fitting of the dispersion relations yields the temperature dependent ratios of the viscosity to the surface tension $\eta(T)/\gamma(T)$ and the shear modulus to

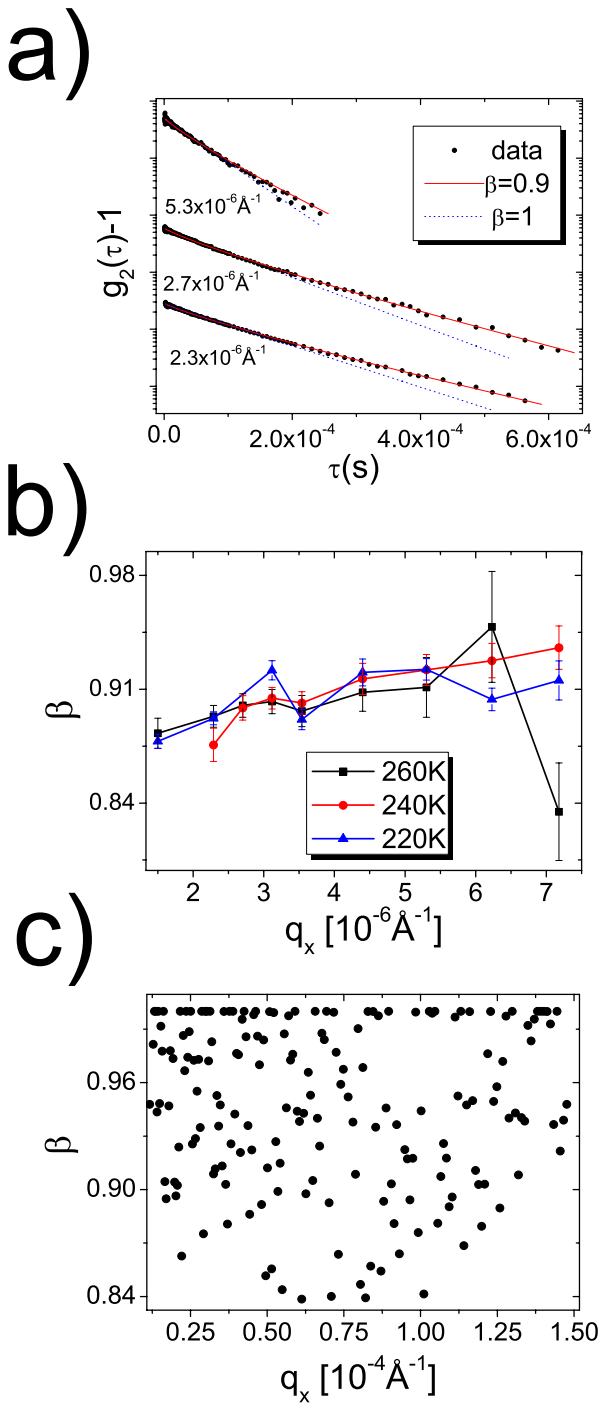

Figure 6.18: a) Fits with stretched exponential relaxation model compared with the simple exponential relaxation. Data were collected at 260 K. The correlation functions have been shifted for clarity. b) The stretched exponent $\beta(q_x)$ measured at 260 K, 240 K, 220 K, and c) at 192 K.

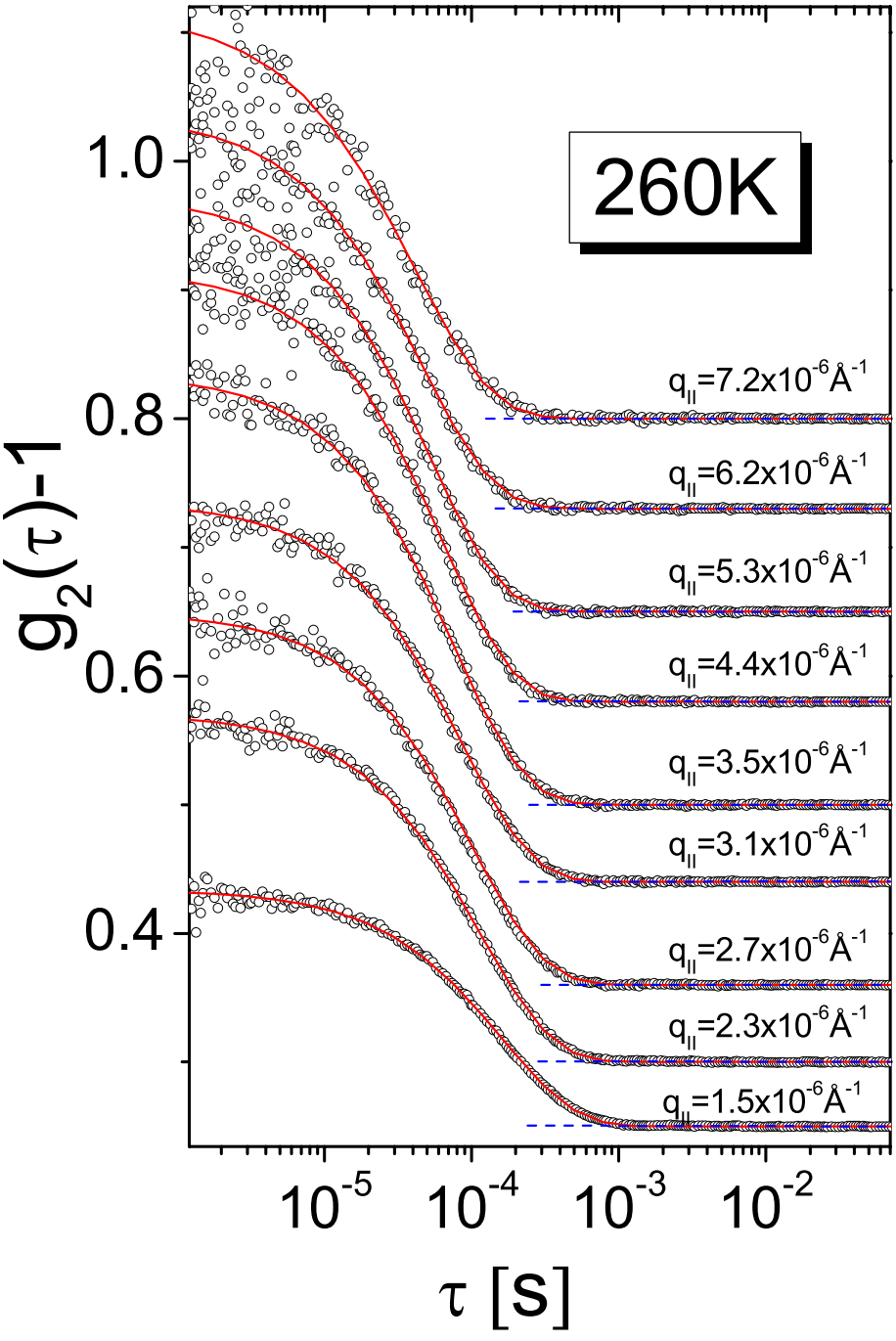

Figure 6.19: Intensity autocorrelation functions $g_2(\tau, q_x)$ recorded on the surface of dibutyl phthalate at 260 K. The origin of the correlation functions have been shifted for clarity and marked with the dashed blue line.

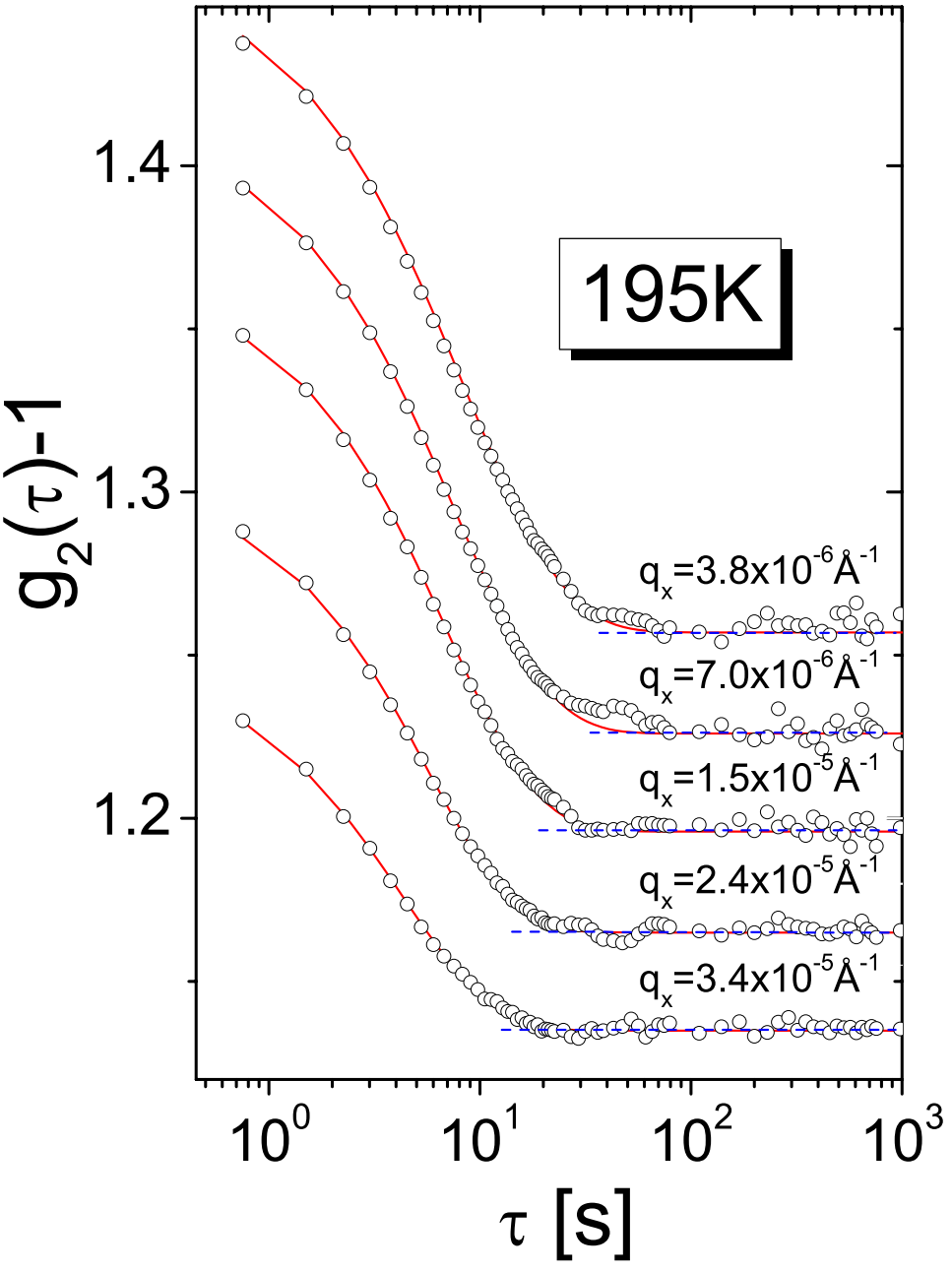

Figure 6.20: Selected intensity autocorrelation functions collected at 195 K. The origin of the correlation functions have been shifted for clarity and marked with the dashed blue line.

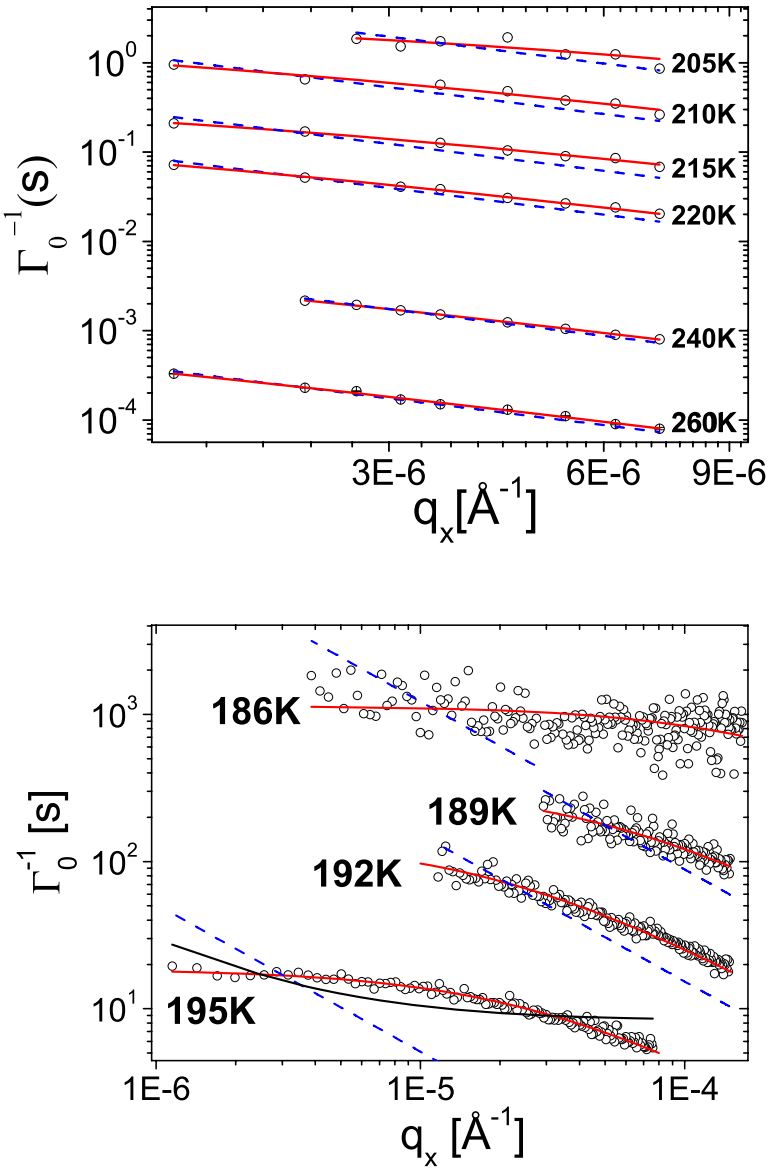

Figure 6.21: Dispersion relation $\Gamma^{-1}(q_x)$ for dibutyl phthalate for 186 K $\leq$ T$\leq$ 260 K. Measured data sets ($\circ$) were analyzed in the frame of the capillary wave model (dotted blue line) and Kelvin-Voigt (solid red line) model of viscoelastic liquid. The prediction of the Maxwell model (black solid line) is shown for the data collected at 195 K.

the surface tension $\mu(T)/\gamma(T)$. Since $\gamma(T)$ has been previously determined by means of x-ray reflectivity measurements, the viscosity and shear modulus can be directly calculated from the XPCS data. The obtained viscosity $\eta(T)$ and shear modulus $\mu(T)$ are summarized in Tab. 6.1.
The static aspect of the dibutyl phthalate surface was studied by analyzing the distribution of scattered intensity within the sum of all the CCD images collected at a given temperature. Two CCD images integrated over the total acquisition time of 400 s at 220 K and 7140 s at 186 K are presented in Fig. 6.16. With decreasing temperature below T_g the characteristic time of the surface fluctuations becomes comparable with the experimental timescale and a static speckle pattern is observed. Above the glass transition temperature the fluctuation of the surface results in blurring of the interference picture.

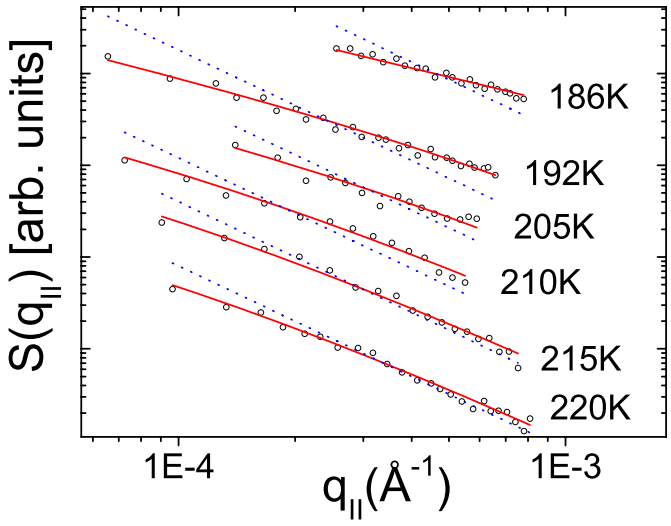

Figure 6.22: Static structure factor $S(q_{||}, 0)$ of dibutyl phthalate surface fitted with capillary wave model (dashed line) and Voigt-Kelvin model (solid line).

The viscoelasticity of dibytyl phthalate near the surface is also supported by the static structure factor $S(q_{||}, 0)$ data (see Fig. 6.22). All curves have been fitted using the formula provided by the Kelvin-Voigt model, relating the static structure factor to surface tension γ and shear modulus μ of the investigated liquid

$$S(q_{||}) \propto k_B T \frac{1}{\gamma q_{||}^2 + 2\mu q_{||}}. \tag{6.43}$$

Since the obtained value of the shear modulus is strongly influenced by the level of the background used during data evaluation, only a quantitative anal-

ysis of the static data can be performed. At lower temperatures, an enhanced elasticity is reflected by the systematic deviation of the profile of the collected intensity from the capillary wave model predictions.
The surface viscosity $\eta(T)$ (see Fig. 6.23) agrees well with the bulk data measured with inelastic x-rays scattering (IXS) [25] and ultrasonic measurements [20, 19]. The VFT fit

$$\ln(\eta(T)) = \ln(\eta_0) + \frac{B}{T - T_0} \tag{6.44}$$

yields the Vogel temperature T_0=149±2 K and B=1083.7±89 K^{-1}. The glass transition temperature $T_g \approx 177$ K, defined as the temperature at which the viscosity becomes equal to $\eta = 10^{12}$ Pas, was extrapolated from the collected data. Similarly to the viscosity, also for the value of the shear modulus μ(T) a

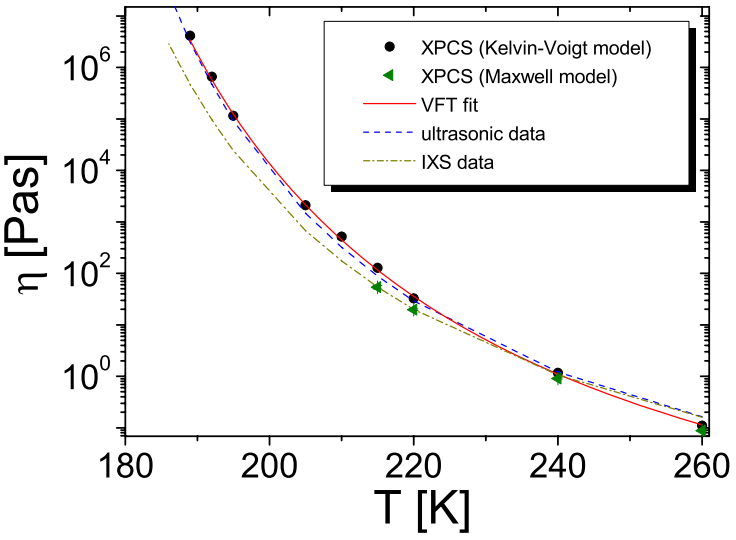

Figure 6.23: Viscosity $\eta(T)$ of dibutyl phthalate obtained from the Kelvin-Voigt model (•) and the Maxwell model (◁) compared with ultrasonic [20] (dotted blue line), x-ray inelastic scattering (IXS) [25] (green dotted line). The viscosity data from the Kelvin-Voigt model were fitted with the Vogel-Fulcher-Tamman equation (red line).

single VFT equation is sufficient to model the XPCS findings. The best agreement with the experimental data has been obtained for the Vogel temperature T_0=168±4 K. The shear modulus measured at the surface is compared to the bulk values in Fig. 6.24. The high frequency limit of the shear modulus $\mu(T)$ is measured with the ultrasonic studies, while the XPCS is sensitive to the

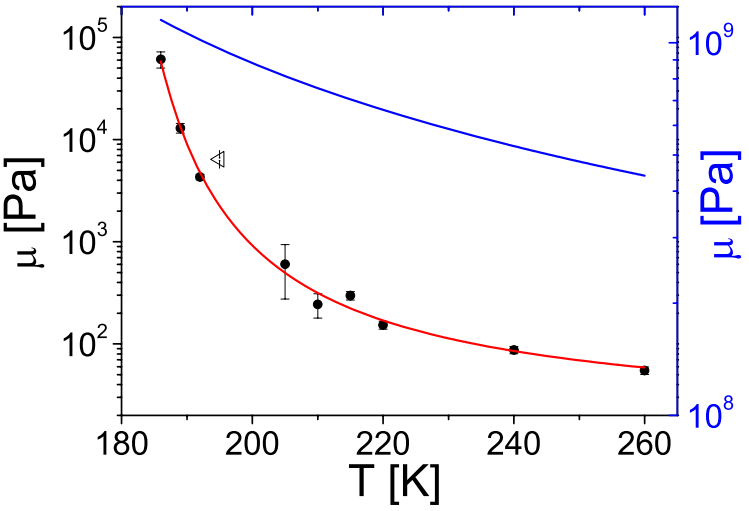

Figure 6.24: Shear modulus of dibutyl phthalate obtained from the Kelvin-Voigt model (•). Data from the Kelvin-Voigt model were fitted with the Vogel-Fulcher-Tamman equation (red line). The value of μ measured at 195 K is marked by (◁) (for details, please see text). The ultrasonic [20] (blue line) are shown for comparison.

much slower fluctuations of the liquid surface due to excitation of the capillary (Rayleigh) waves. The value of the shear modulus at room temperature μ_{RT}=39 Pa has been estimated.
Two additional measurements were performed at 195 K and 220 K for dibutyl phthalate heated from 186 K. At 195 K the surface shows an enhancement in the elasticity in comparison to the values predicted from VFT fit for the data collected upon sample cooling, while two data sets collected at 220 K match within the experiential uncertainty. The enhancement of the elasticity at low temperatures can be explained by the hysteresis effect. The dynamics of the dibutyl phthalate in deeply supercooled state is strongly affected by the presence of the structures frozen-in at lower temperatures. Far above the glass transition temperature the liquid relaxes fast enough to instantaneously "erase" its thermal history. In this case observed dynamics is independent of the previous sample treatment.

The structural relaxation rate defined as

$$\lambda(T) = \frac{\mu(T)}{\eta(T)} \tag{6.45}$$

is plotted in Fig. 6.25 as a function of inverse temperature 1000/T. The transition from the liquid to the glassy state is reflected by a change in λ over

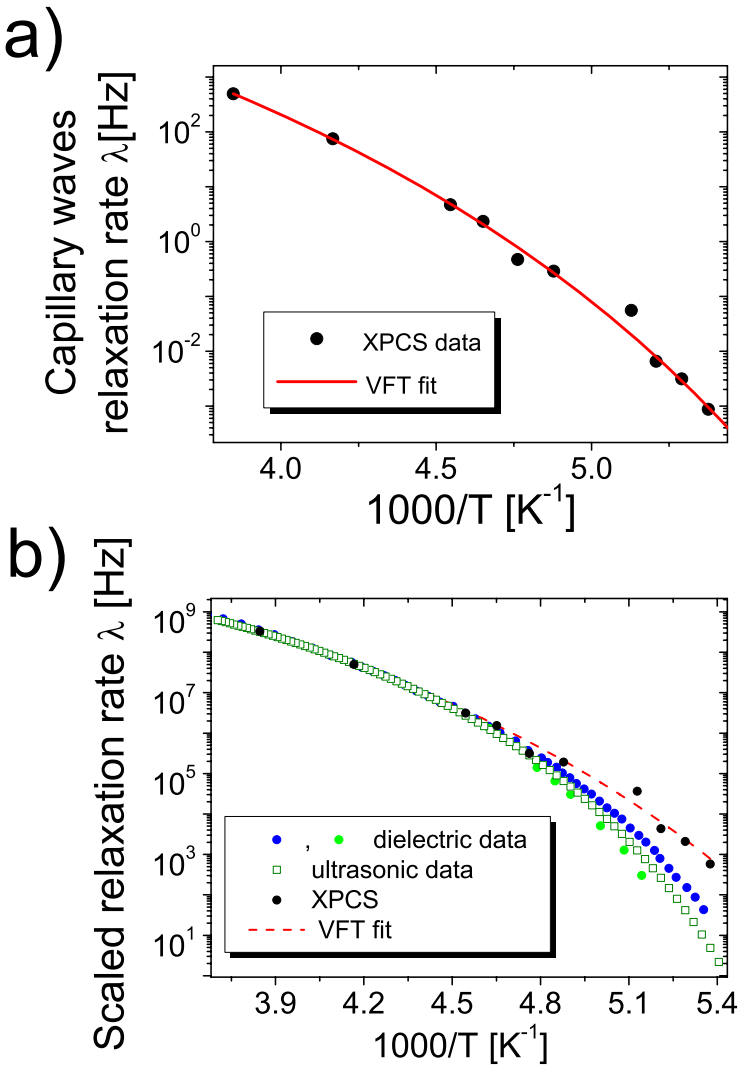

Figure 6.25: a)Capillary relaxation rate λ measured with XPCS b) Scaled relaxation rate λ of dibutyl phthalate measured with XPCS compared to the results from other experiments: dielectric spectroscopy [74, 75] and ultrasonic measurements [20].

six orders of magnitude. To compare the relaxation rates obtained from different techniques the curves were scaled to coincide at 260 K. The $\lambda(T)$ function for the dibutyl phthalate surface consists of a single branch, identified as a α-relaxation, which shape can be described by the simple Vogel-Fulcher-Tamman equation. The best fit was obtained for the Vogel temperature $T_0 = 123.8 \pm 12.9$ K. At higher temperatures (205 K<T<260 K) the relaxation rate obtained from XPCS experiment was found to be in good

agreement with the results from dielectric spectroscopy [74, 75] and the ultrasonic measurements [20], while the systematic deviation from the dielectric data was observed at lower temperatures. At 186 K the relaxation rate λ near the liquid(glass)/vapor interface is around one order of magnitude larger than in the bulk. **The surface relaxation becomes considerably faster than in the bulk upon approaching the calorimetric glass transition temperature T_g.**

Chapter 7

The quasielastic nuclear forward scattering

7.1 Motivation

The quasielastic nuclear forward scattering experiment was performed to study the relaxation processes at the nanometer length-scales around the glass transition temperature. This technique is well-suited for the investigation of the molecular motion in the time window from 10^{-8}s to 10^{-6}s corresponding to the transition from the fast β-relaxation to the α-relaxation. The surface sensitivity was achieved by applying quasielastic nuclear forward scattering in the grating incidence geometry. The results from the quasielastic nuclear forward scattering were expected to give insight into the mechanism of freezing of dibutyl phthalate near the liqui/vapour interface.

7.2 Resonant absorption and emission

In this and the following sections a short introduction to the quasielastic nuclear forward scattering (QNFS) experiment is given. Details concerning the theory of nuclear resonant scattering of synchrotron radiation have been described extensively in [76, 77, 78, 79, 80, 81, 82]. Because of the paramagnetic properties of iron in ferrocene the magnetic interactions will be omitted in the introduction.
The nuclear forward scattering experiment is based on the recoil-free resonant absorption of the photon with an energy matching the energy difference between the excited and the ground state of the irradiated isotope, the so-called Mössbauer effect. The resonant absorption followed by the re-emission is presented in Fig. 7.1 for ^{57}Fe. There is a certain probability that the Mössbauer isotope will absorb the incident ray (blue) with the energy E_γ equal to $\Delta E = E_e - E_g$ and will be brought from the ground to the excited state.

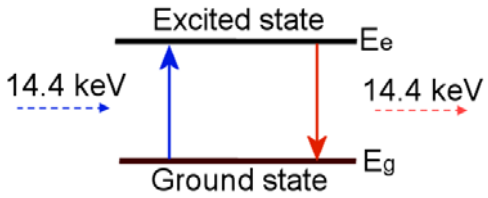

Figure 7.1: Nuclear transition between the ground and the excited state of the isolated and stationary ^{57}Fe isotope. The resonant absorption is marked with the blue arrows, while the deexcitation and re-emission are indicated by the red arrows.

The lifetime of the excited state in case of ^{57}Fe is τ_0=141 ns. Afterwards, the nucleus returns to its ground state and releases the excess energy by emitting the secondary photon (red) or ejecting a core electron instead (the internal conversion effect). The number of nuclei decaying via internal conversion per nuclei decaying via emission of the resonant photon is denoted by the internal conversion coefficient α. The resonant cross-section $\sigma(E)$ is defined as

$$\sigma(E) = \sigma_0 \frac{(\Gamma_{nat}/2)^2}{(E_0 - E)^2 + (\Gamma_{nat}/2)^2} \tag{7.1}$$

where

$$\sigma_0 = \frac{2\pi}{k^2} \frac{2I_e + 1}{2I_g + 1} \frac{1}{1 + \alpha}, \tag{7.2}$$

with I_e, I_g being the nuclear spin quantum number and Γ_{nat} is the natural linewidth (4.6×10^{-9}eV for ^{57}Fe).

7.3 The Doppler shift and the Lamb-Mössbauer factor

In the previous section the case of a stationary nucleus was considered. This condition is never met for a real system. At all temperatures atoms are not frozen but move continuously with the speed v. This movement results in the Doppler shift of the frequency of the absorbed (re-emitted) photon

$$\Delta\omega(v)_{Doppler} = \omega_0 \frac{v}{c}. \tag{7.3}$$

An additional shift of the photon frequency is caused by the recoil accompanying an emission or an absorption event

$$\Delta\omega_R = \frac{E_R}{\hbar} = \frac{E_\gamma^2}{2\hbar M c^2}, \tag{7.4}$$

where M denotes the mass of the absorbing (emitting) atom, E_R is the recoil energy of the photon, and the speed of light is abbreviated by c. Taking both effects into account the final frequency of the resonant photon is given by

$$\omega = \omega_0 \pm A\Delta\omega(v)_{Doppler} \pm \Delta\omega_R. \tag{7.5}$$

The pre-factor A varies from -1 to 1 depending on the relative direction of the atomic motion versus the detector.
The recoil energy created during the absorption (emission) of the 14.4 keV is $E_R = 1.95 \times 10^{-3} eV$, what significantly exceeds the linewidth of the ^{57}Fe nucleus. For an isolated atom the recoil prevents the resonant scattering effect. If the atom is not free but fixed in solid (or molecule), M in the eq. 7.4 is not the mass of a single atom but rather the mass of the cluster of atoms (the mass of the molecule). In such a case the recoil energy becomes comparable with the linewidth of the isotope and the conditions for resonant absorption are fulfilled. However, during the absorption (emission) of the photon by the nucleus embedded in the solid the part of the energy may be transformed into the matrix vibrations (phonons in case of crystal) destroying the conditions for the resonance to take place. There is a certain probability, called the Lamb-Mössbauer factor f_{LM}, that the resonant quantum will be emitted without loss of energy due to the vibrations in the solid. The factorf_{LM} for the atom fluctuating with the mean square amplitude $\langle x^2 \rangle$ is given by

$$f_{LM} = \exp(-k^2\langle x^2\rangle) = \exp(-\frac{E_\gamma^2}{\hbar^2 c^2}\langle x^2\rangle). \tag{7.6}$$

Since the energy of the resonant photon is fixed, the probability of recoilless emission can be improved by lowering the temperature(reducing the amplitude of the vibrations).

7.4 Electric quadrupole interaction

Nuclear states with the spin number I>1/2 have a non-spherical charge distribution. The measure of the charge deformation is given by the nuclear quadrupole moment Q which can be expressed by

$$eQ = \int \rho_n(\vec{r}) r^2 (3\cos^2\theta) - 1) d\vec{r}^{\,3}, \tag{7.7}$$

where e is the charge of the proton, ρ_n stands for the nuclear charge density in the volume element $d\vec{r}^{\,3}$ at position $\vec{r}$ from the center of the nucleus and at an angle θ to the nuclear spin quantization axis. The interaction with the external electric field gradient (EFG) results in a splitting of the excited state (I=$\frac{3}{2}$) into two sub-levels with the nuclear magnetic spin quantum numbers m=$\pm\frac{1}{2}$ and m=$\pm\frac{3}{2}$, what is represented in energy domain by two lines in the Mössbauer spectrum and by the modulation of the natural decay of the

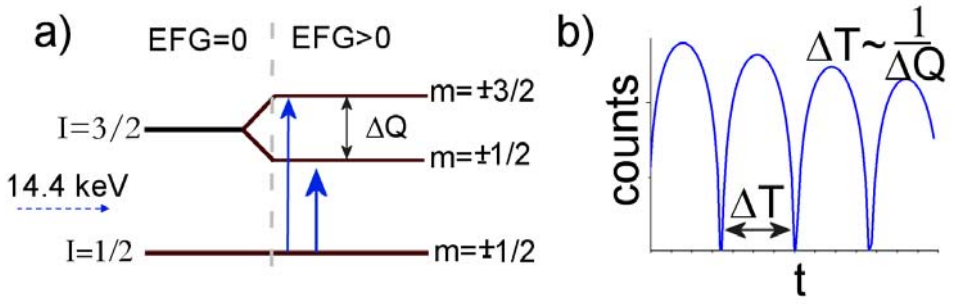

Figure 7.2: a) Splitting of the excited state of the ^{57}Fe isotope due to interaction with the external electric field gradient. b) The corresponding quantum beating pattern.

delayed signal by quantum beating in the time domain (see Fig. 7.2). The electric quadrupole energy depends on the gradient of the electrostatic field at the position of the nucleus. In general gradient of the field is expressed by means of the electric field gradient (EFG) tensor

$$V_{ij} = \frac{\delta^2 V}{\delta x_i \delta x_j}, \tag{7.8}$$

where V is the electrostatic potential inside the nucleus. The magnitude of the splitting(the frequency of the dynamical beats) reflects the energy difference between two excited states (see Fig. 7.2)

$$\Delta Q = E_{e(m=\pm\frac{3}{2})} - E_{e(m=\pm\frac{1}{2})} = \frac{eQV_{zz}}{2}(1+\frac{\eta^2}{3})^{\frac{1}{2}}. \tag{7.9}$$

To completely describe the EFG it is sufficient to determine the value of V_{zz} component and the asymmetry parameter

$$\eta = \frac{V_{xx} - V_{yy}}{V_{zz}}. \tag{7.10}$$

The electric field gradient is considered to have mainly two contribution:

1. A valence electron contribution arising from an anisotropic electron distribution in the valence shell of the Mössbauer isotope.

2. A neighboring ions contribution coming from an anisotropic charge distributions due to the presence of the other ions around.

7.5 Quasielastic nuclear forward scattering

Nuclear forward scattering (NFS) of synchrotron radiation, similarly to the conventional Mössbauer spectroscopy, is based of the effect of excitation of

the nuclear level with a synchrotron pulse (which is much shorter than the lifetime of the excited state) followed by the coherent decay of excited states characterized by the lifetime τ_0. The quantity of interest is the intensity of the delayed radiation, or to be more precise its evolution versus time after the exciting pulse. Due to the lack of periodicity in case of a disordered matter the condition of constructive interference of the re-emitted photons is fulfilled only in the forward direction.
The decay time of the excited state governs the time response $I(t)$ of the ensemble of the excited ^{57}Fe nuclei. The electrical quadrupole splitting of the iron nuclei in the tracer (ferrocene $Fe(C_5H_5)_2$) used during NFS experiment introduces the modulation of the delayed signal by quantum beats with a period of around 36 ns. Relaxations with characteristic times comparable to the lifetime of the excited state (τ_0=141 ns) introduce a phase shift between the photons re-emitted by different nuclei and results in an accelerated decay of $I(t)$ due to loss of coherence. Additionally, the coherent multiple scattering in optically thick media enhances the deexcitation process and leads to further increase in the decay rate of the observed intensity. The superposition of all of those effects yields the temporal evolution of the delayed signal [33]

$$I(t) = I_0[\int \frac{d\omega}{2\pi} e^{-iwt}(e^{\frac{-L}{4\tau_0}\phi(q,\omega)} - 1)]^2 \tag{7.11}$$

$$\phi(q,\omega) = \int dt' e^{i(\omega-\omega_0)t' - t'/2\tau_0} F_s(q,t') \cos(\Omega t'/2), \tag{7.12}$$

where the term $\phi(q,\omega)$ is called the response function, I_0 stands for the prompt intensity, and $\hbar\omega_0$ is the nuclear transition energy (14.4125 keV for ^{57}Fe). The effective thickness L is a function of the resonant cross-section σ, Fe number density $\frac{N}{V}$, enrichment in ^{57}Fe χ, and the optical thickness z

$$L = \sigma \frac{N}{V} \chi z. \tag{7.13}$$

Combining the eq. 7.11 and 7.12 yields

$$I(t) = I_{kin} R^2(t), \tag{7.14}$$

with

$$I_{kin} = I(0) L^2 \exp(-\frac{t}{\tau_0}) F_s(t)^2. \tag{7.15}$$

The multiple scattering effect is represented by the factor $R(t)$, which in absence of relaxation ($\tau_{relax} = \infty$) is modeled with the Bessel function of first order and the first kind $J_1(t)$

$$R(t) = \frac{J_1(2\sqrt{L f_{LM} t})}{\sqrt{L f_{LM} t}}. \tag{7.16}$$

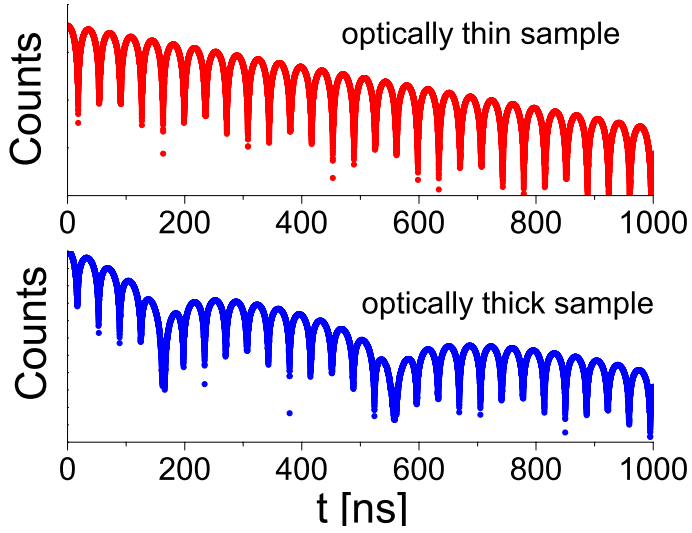

Figure 7.3: Simulated delayed signal (eq. 7.11) for the optically thin (red) and thick (blue) sample with well pronounced dynamical beating minima at around 180 ns and 550 ns.

In the limiting case of a small effective thickness $Lf_{LM} \rightarrow 0$, $R(t)$ can be approximated by

$$R(t) = \exp(-\frac{Lf_{LM}}{2\tau_0}). \tag{7.17}$$

The oscillatory behavior of $R(t)$ (eq. 7.16) leads to an additional modulation of the amplitude of the signal scattered in the forward direction, so-called dynamical beating (DB) (see Fig. 7.3). In general, DB exhibit characteristic features, which distinguish them from the quantum beating:

1. The separation between the minima of the dynamical beating increases with time.

2. The period of the dynamical beats decreases with increasing optical thickness L.

3. The initial decay of the delayed intensity is speed up proportionally to the optical thickness L.

The atomic motion is described by the so-called intermediate scattering function $F_s(q,t)$. In case of free diffusion with the diffusion coefficient D one obtains

$$F_s(q,t) = f_{LM} \exp(-Dq^2 t). \tag{7.18}$$

For glassy systems, the dynamics is described by the Kohlrausch stretched exponential

$$F_s(q,t) = f_{LM} \exp(-(t/\tau_{relax})^{\beta}). \tag{7.19}$$

It was shown in [18] that for free diffusion of ferrocene, assuming a Lorentzian profile of $\phi(q,\omega)$ eq. 7.11 can be simplified to

$$I(t) = I_0 \cos^2(\Omega t/2) \exp(-\frac{t}{\tau_0} - \frac{2t}{\tau_{relax}}) \frac{Lf_{LM}}{2t\tau_0} [J_1(\sqrt{\frac{Lf_{LM}t}{2\tau_0}})]. \qquad (7.20)$$

The cosine oscillatory factor in eq. 7.20 represents the quantum beating due to the interference between the photons emitted during deexcitation of the two resonance sub-levels, while the multiple scattering yields the dynamical beating (Bessel function J_1). When the product $f_{LM}L$ becomes so small that the first minimum of J_1 is beyond the experimental time window formula 7.20 can be further simplified to

$$I(t) = I_0 \cos^2(\Omega t/2) (\frac{Lf_{LM}}{4\tau_0})^2 \exp(-\frac{t}{\tau_0} - \frac{2t}{\tau_{relax}} - \frac{Lf_{LM}t}{8\tau_0}). \qquad (7.21)$$

7.6 Experimental details

The quasielastic nuclear scattering(QNFS) experiment was performed at beamline ID18 at the European Synchrotron Radiation Facility (ESRF) in Grenoble. The layout of the beamline is shown in Fig. 7.4. Radiation from the undulator

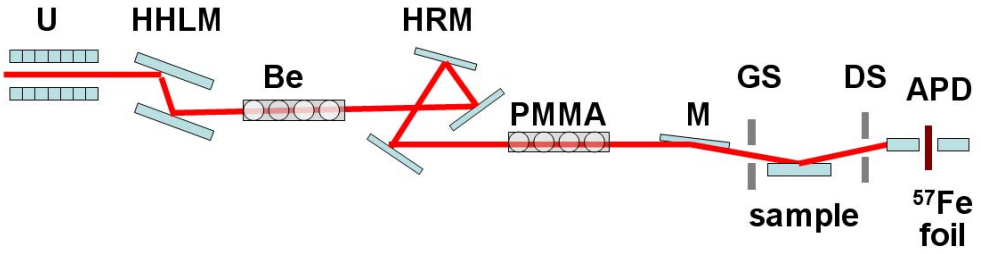

Figure 7.4: Layout of the beamline ID18. U- undulator insertion device, HHLM- high heat load monochromator, HRM- high resolution monochromator, Be- first collimating lenses, PMMA- second focusing lenses, M-mirror, GS-guard slits, DS- detector slits, APS- Avalanche Photo Diode detectors.

is pre-monochromatized by a high heat-load monochromator (HHLM). Since the ^{57}Fe-nuclei can absorb only radiation from a narrow energy range of few neV around 14.4 keV, the load of the detector and the level of the background can be minimized by further reduction of the energy spread of the incident radiation to around 1 meV by means of the high resolution monochromator (HRM). Compound refractive lenses (Be) are used to improve the performance of the HRM by matching the divergence of the beam to the acceptance of the reflections of the HRM crystals. Before impinging the specimen, the incident beam is focused in horizontal and vertical direction to 100μm$\times$100μm with

the help of compound refractive lenses. The content of the ^{57}Fe isotope in the investigated sample was low and a rather weak delayed signal was expected to be observed during the experiment. To improve the signal to background ratio the focusing beryllium lenses, known to be contaminated by iron atoms [83], were exchanged to polymethylmethacrylate (PMMA) lenses.

The incident beam is deflected downwards by the silicon mirror M, passes through the guard slits GS ($0.5 \times 4mm^2$) and impinges on the sample surface at a shallow angle $\alpha_i = 1.2$ mrad below the critical angle $\alpha_c = 1.5$ mrad. This limits the penetration depth of 14.4 keV radiation into dibutyl phthalate to only $\Lambda = 150$ Å. The beamsize of 30μm$\times 30\mu$m ensures the beam footprint on the investigated surface to be much shorter than the lateral dimension of the sample, thus the influence of the meniscus should be minimized.
The time necessary for an electron bunch to travel around the storage ring at the ESRF (circumference of 844.4 m) is 2.815 μs per revolution. In the so-called 16-bunch mode 16 equidistant buckets are filled, resulting in the time gap Δt between the two consecutive bunches of 176 ns. In practice, the useful time window for QNFS measurements is reduced by the time necessary for the detector to recover after the prompt pulse, which is around 20 ns. The remaining 151 ns matches the lifetime $\tau_0 \approx 144$ ns of the excited state of ^{57}Fe. The non-resonant part of the incident radiation is reflected by the investigated surface and interacts very weakly with the sample. Only photons from the resonant bandwith of the order of 10neV are absorbed by the iron nuclei and give rise to the QNFS signal.
A large dynamical range, nanosecond resolution and fast recovery time after the prompt pulses ($\approx 10^9$ photons/s) are mandatory for detectors used for nuclear forward scattering. The detector must stand the intense pulse exciting the sample, and a few nanosecond later be able to count a single photon of the delayed signal. Those requirements are met by the avalanche photodiode (APD) detectors. Since a single semi-transparent APD can detect only around 30% of the incident photons at 14.4 keV, the efficiency of the data acquisition is improved by stacking three detectors in a row.
The intensity of the resonant incident radiation in the prompt pulse is monitored by a fourth APD (further abbreviated by D4), positioned at the very end of the beamline, with an enriched ^{57}Fe foil mounted in front of it.
As described in the chapter concerning the cryostat design, in order to cool the organic liquids below their glass transition temperature T_g it is necessary to use the trough coated with a intermediate teflon layer. The three reservoirs version of the trough was used during the nuclear forward scattering experiment (see Fig. 7.5).

Dibutyl phthalate mixed with ferrocene was poured into the central reservoir, while the pure sample occupied the auxiliary reservoirs. The ratio of the ferrocene to dibutyl phthalate molecules was around 1:24. Within the detection limits, such small amount of the dopant was confirmed not to influence the

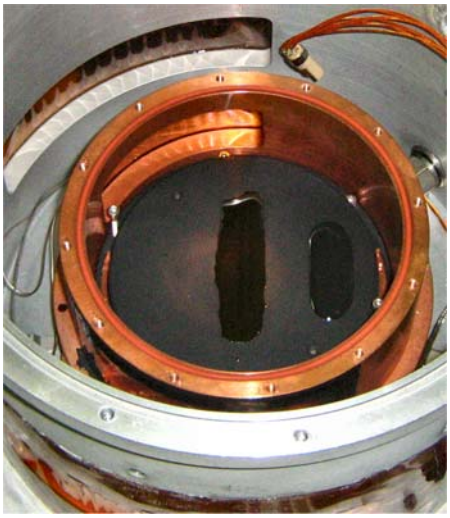

Figure 7.5: The top view of the inner chamber showing the configuration of the cryostat used during QNFS experiment. The investigated liquid occupies the center reservoir and the pure dibutyl phthalate was poured into the auxiliary one.

properties of the DBP surface. The sample temperature was measured with two Pt100 sensors dipped into the pure liquid 1 cm apart from each other.
The quasielastic nuclear forward scattering spectra were collected in the following sequence. The first measurements were performed for dibutyl phthalate/ferrocene cooled down to 155 K. Next, the delayed signal was collected at higher temperatures up to $T = 194$ K with 5 K steps. The maximum temperature, at which the resonant signal could be measured was limited by the dramatic drop in the value of the Lamb-Mössbauer factor f_{LM} with increasing temperature. Eventually, the last measurement was done for sample cooled down to 149 K. The cooling rate was 0.6 K/min. After reaching the desired temperature, the sample environment was stabilized for around 30 minutes before the measurement started.

The cryostat was mounted on a stage allowing the translation of the studied liquid in x, y, and in z direction. The relative position of the detectors with respect to the sample surface was controlled by tuning the height of the detector tower. Before each measurement both cryostat and detectors heights were scanned to optimize the delayed intensity.
The principles of the surface-sensitive QNFS measurement are presented in Fig. 7.6. The beam impinges the investigated surface at a shallow angle $\alpha_i \approx 0.8\alpha_c$. The evanescence wave excites only the topmost layer of the surface determined by the penetration depth ($\Lambda \approx$150 Å). The photons re-emitted in forward direction within the time window from 20 ns to 160 ns after the exciting pulse are collected at an exit angle $\alpha_f = \alpha_i$ and $\alpha_f = 0$ (see Fig. 7.6).

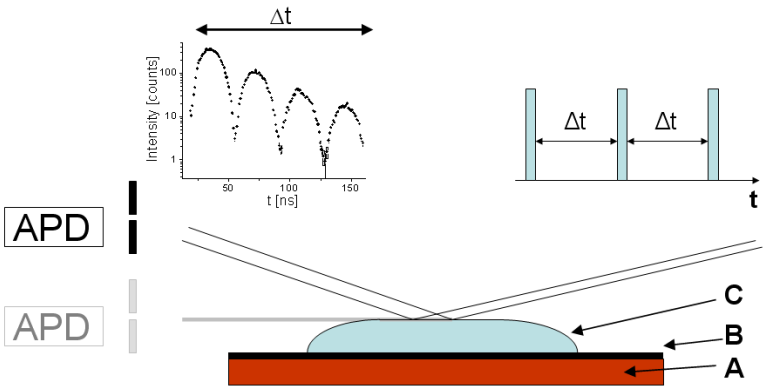

Figure 7.6: Schematic drawing of the surface sensitive QNFS experiment. The investigated liquid (C) is poured on top of Cu plate (A) coated with teflon(B). The APD detector collects the delayed signal form the flat part of the sample surface at an exit angle $\alpha_f = \alpha_i$ and $\alpha_f = 0$.

7.7 Results

All the recorded patterns were analyzed for the delayed time window ranging from 20 ns to 160 ns after the prompt. The time spectra recorded at exit angle $\alpha_f = \alpha_i$ (further referred to as specular data) and $\alpha_f = 0$ (further referred to as off-specular data) are displayed in Fig. 7.7 to Fig. 7.10.

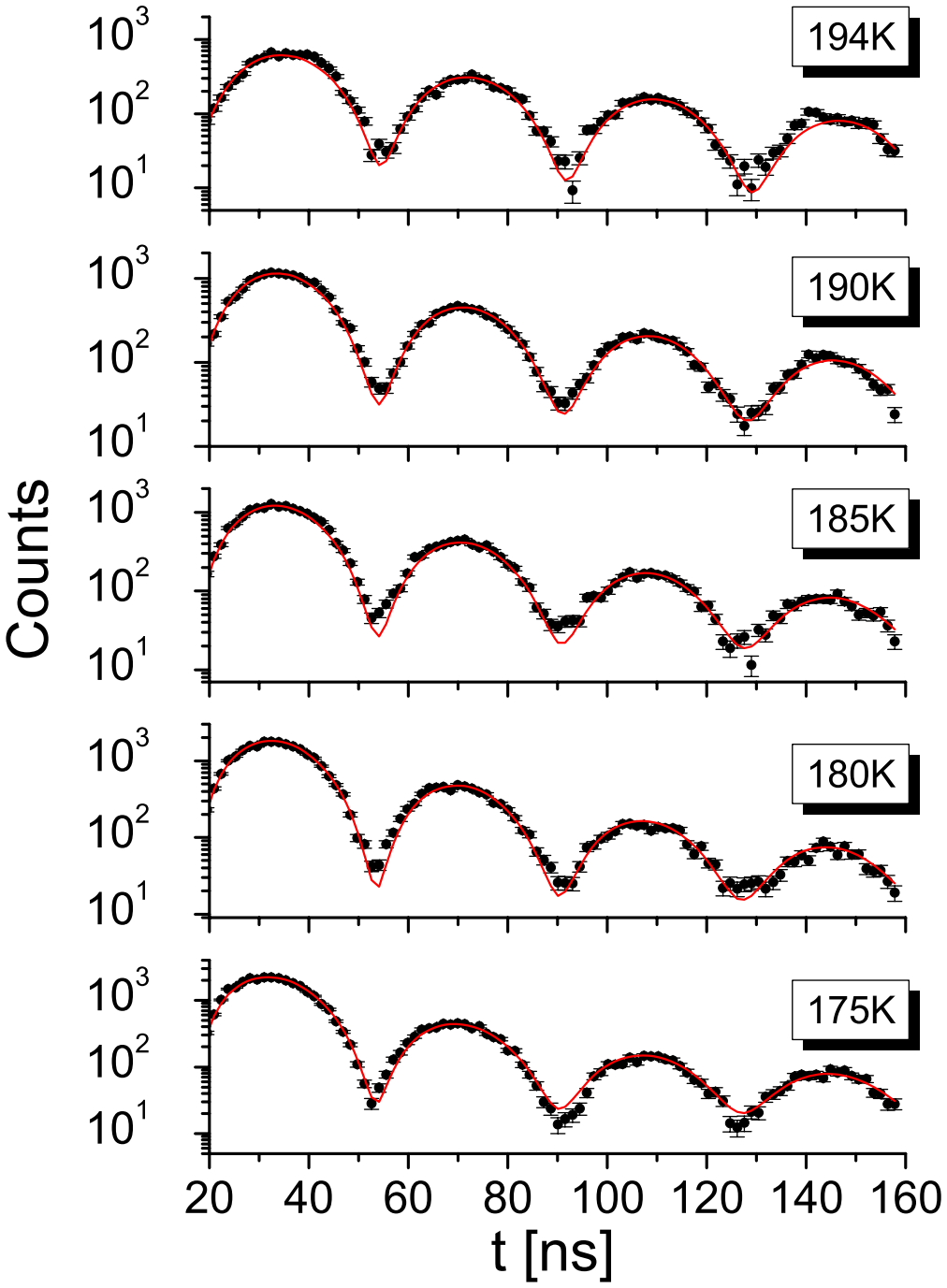

Figure 7.7: QNFS spectra collected at $\alpha_f = \alpha_i$.

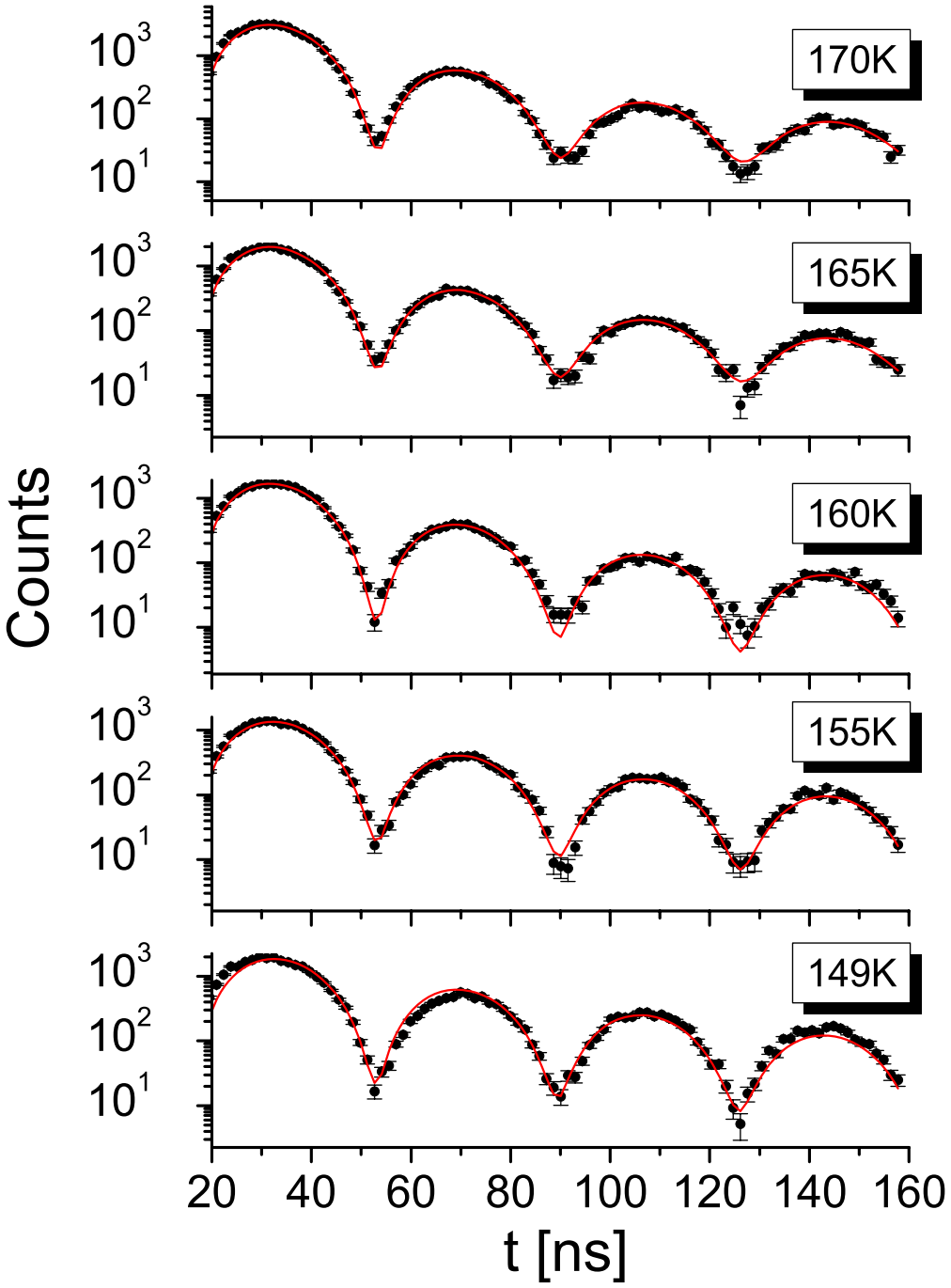

Figure 7.8: QNFS spectra collected at $\alpha_f = \alpha_i$ (continued).

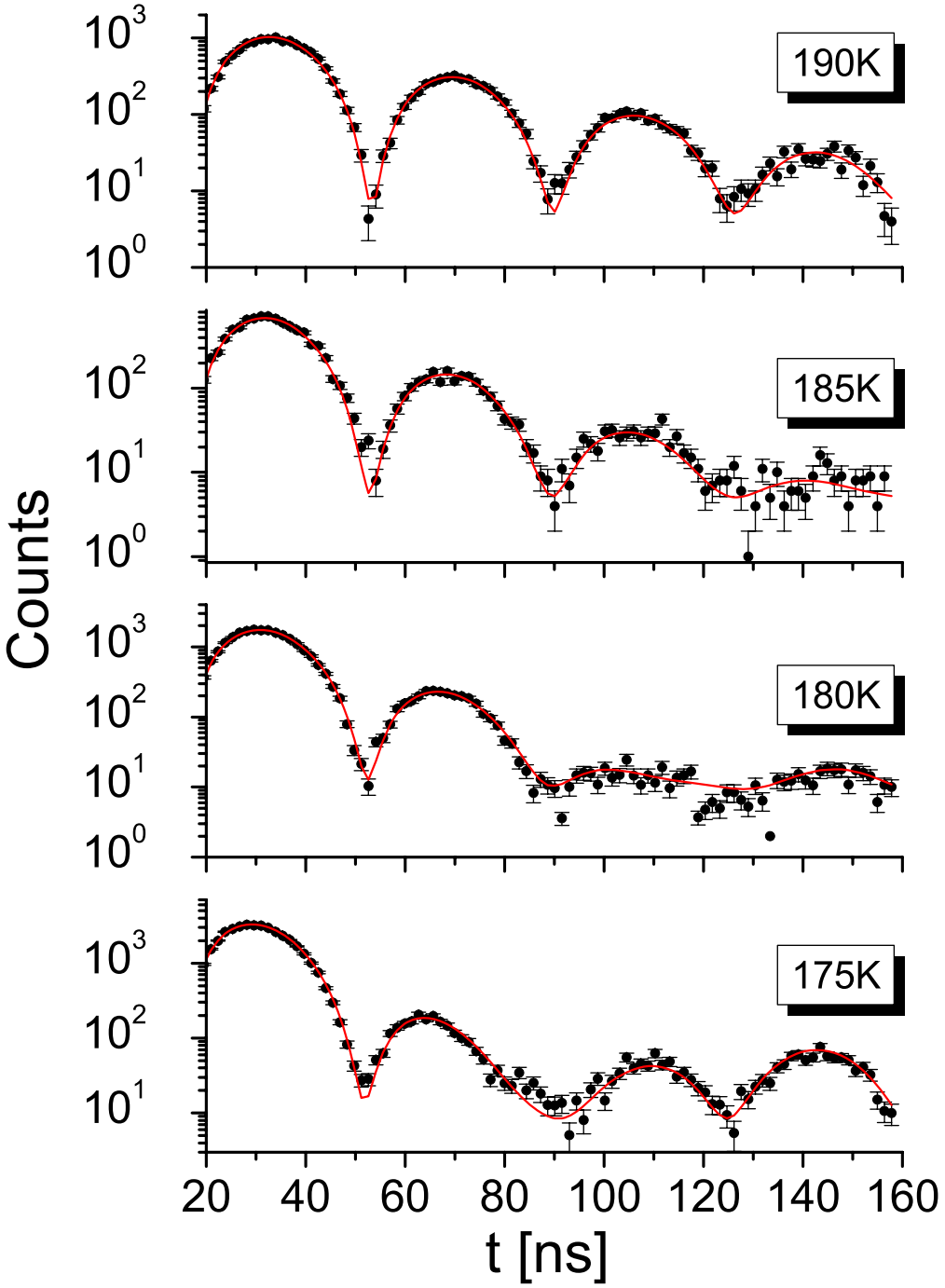

Figure 7.9: QNFS spectra collected at $\alpha_f = 0$.

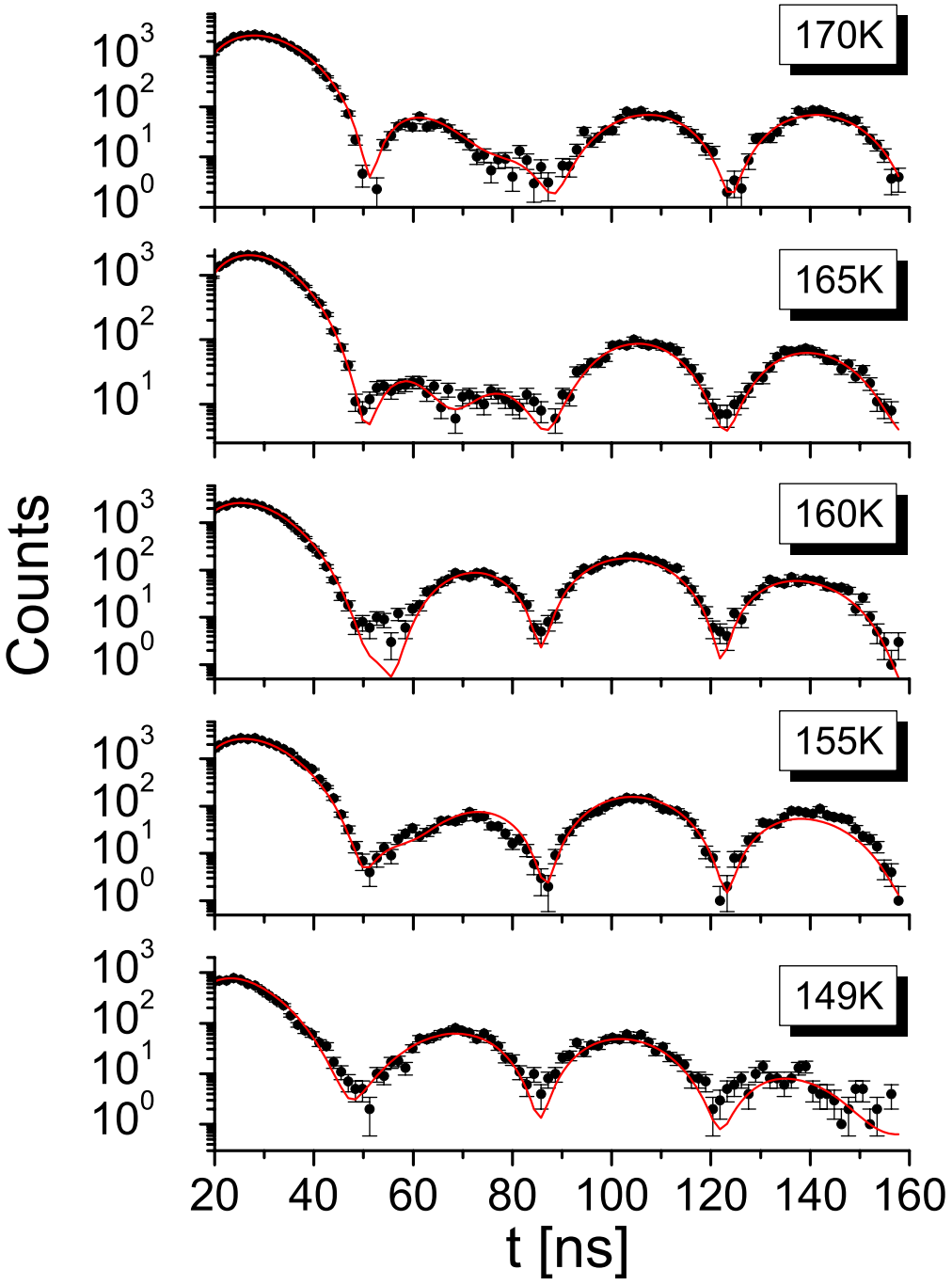

Figure 7.10: QNFS spectra collected at $\alpha_f = 0$ (continued).

A single quadrupole doublet ΔQ_1 is sufficient to model the decay of the delayed signal near the liquid/vapor interface for temperatures from 194 K down to 185 K. At lower temperatures an additional doublet ΔQ_2 must be added in order to reproduce the shape of the quasielastic nuclear forward scattering spectra.

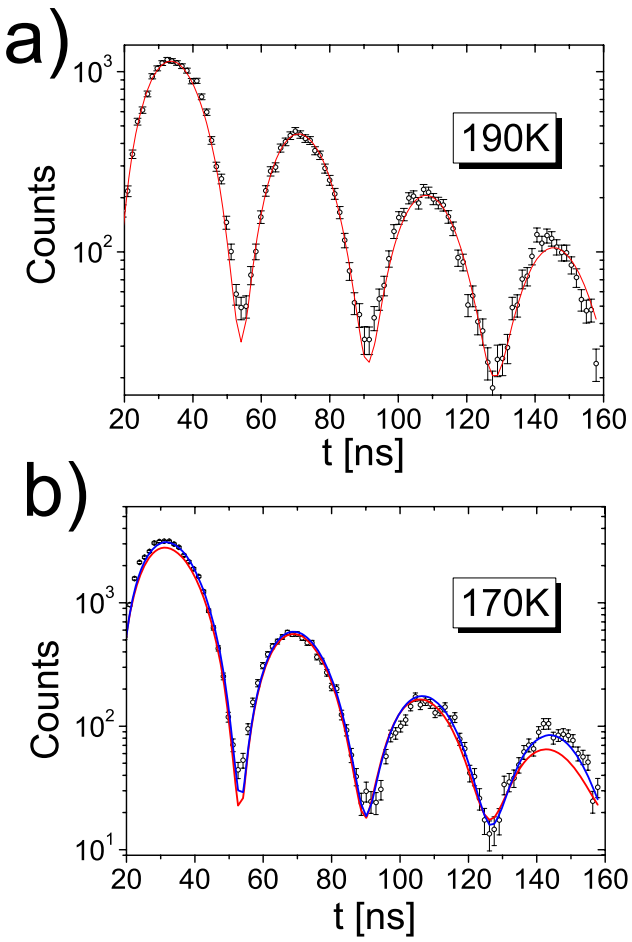

Figure 7.11: Delayed signal patterns collected at a) 190 K and b) 170 K fitted using eq. 7.11 (red line) and eq. 7.22 (blue line).

In the temperature range from 149 K to 180 K the recorded data can be fitted with a coherent superposition of two signals $E_{\Delta Q_1}(t)$ and $E_{\Delta Q_2}(t)$, described by different splitting Ω, effective thicknesses L, and relaxation times

τ_{relax} (see Fig. 7.11)

$$I(t) = |E_{\Delta Q_1}(t) + E_{\Delta Q_2}(t)|^2 = |cE_0 \int \frac{d\omega}{2\pi} e^{-i\omega t}(e^{-\frac{L_1}{4\tau_0}\phi_1(k,\omega)} - 1) + (1-c)E_0 \int \frac{d\omega}{2\pi} e^{-i\omega t}(e^{-\frac{L_2}{4\tau_0}\phi_2(k,\omega)} - 1)|^2 \tag{7.22}$$

where

$$\phi_i(k,\omega_i) = \int dt' e^{i(\omega-\omega_0)t' - t'/2\tau_0} F_{s_i}(k,t') \cos(\Omega_i t'/2) \tag{7.23}$$

and

$$F_{s_i}(k,t) = f_{LM_i} e^{-(t/\tau_{relax_i})^{\beta_i}}. \tag{7.24}$$

The relative strength of both signals $i = 1, 2$ is described by the factor c, the prompt intensity is denoted by $|E_0|^2$, and the nuclear transition energy $\hbar\omega_0 = 14.4125$ keV.
Since the accessible time window from 20 ns to 160 ns is too narrow to determine the stretching parameter β_i, the value reported for the bulk liquid [33] and confined sample [23] was set initially to $\beta_i = 0.5$. The choice of the value of the stretched exponent β does not influence the determination of the quadrupole splitting Ω and slightly alters the value of the Lamb-Mössbauer factor f_{LM} but affects significantly the mean relaxation time τ_{relax}

$$\tau_{relax} = \int dt F_s(k,t)/f_{LM} = \tau_{relax}\beta^{-1}\Gamma(\beta^{-1}). \tag{7.25}$$

A significant improvement of the quality of the fits was achieved by increasing β_2 to 0.9. The absolute value of the relaxation time depends on the stretched exponent chosen and is therefore subjected to a certain errors.
For the data collected at $\alpha_f = \alpha_i$, the optical thickness L of the uniform solution of ferrocene in dibutyl phthalate has been estimated to be smaller than 1. The first minimum of the Bessel function is at $29.4\tau_0/Lf_{LM}$, which is far outside the experimentally accessible time window and no dynamical beating should be observed in the specular patterns, what is confirmed by the shape of the recorded data sets. Because of a strong cross-correlation between parameters in eq. 7.22, for a sample with a small effective thickness $f_{LM}L$ it is impossible to use c, E_0, $L_i f_{LM_i}$, and τ_i simultaneously as free parameters. For samples with a very small value of $f_{LM}L$ the multiple scattering effect can be neglected in eq. 7.22 and the number of the fitting parameters was reduced by setting $L_i = 1$ and including the changes in the effective thicknesses $L_i f_{LM_i}$ into the factors c and $(1-c)$, respectively. The obtained parameters are presented in Fig. 7.12. In the temperature range from 149 K up to 180 K the relaxation time τ_{relax_1} decreases from $3.6\tau_0$ to $3\tau_0$, while τ_{relax_2} is only slightly affected by the temperature changes and stays on the level of $0.25\tau_0$. The frequency of the dynamical beating

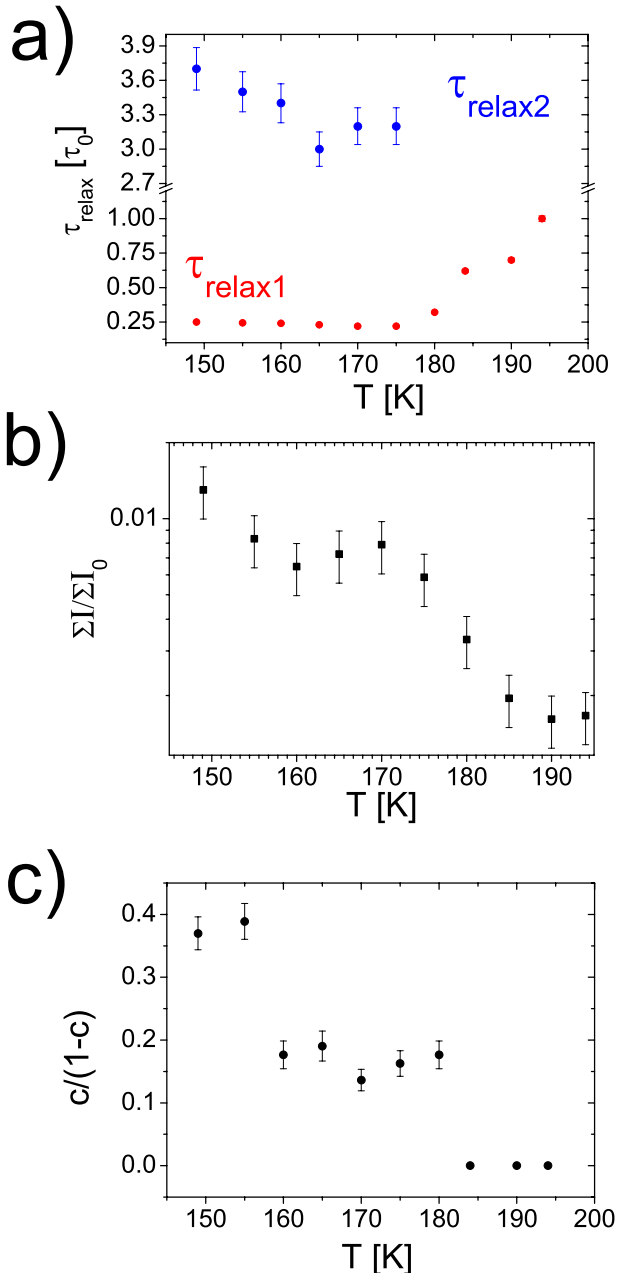

Figure 7.12: The summary of the parameters obtained from the fitting of the quasielastic nuclear forward scattering data: a)the relaxation times, b) the integrated delayed resonant intensity $\sum I$ normalized to the total resonant incident intensity $\sum I_0$, and c) the relative fraction of the signals emitted by the slowly and the fast relaxing fractions of the probed volume.

Ω is around $24.4\tau_0^{-1}$ and $24.0\tau_0^{-1}$ for the first and the second quadrupole splitting, respectively. The relative contribution of the slowly and fast decaying signals, c/(1-c), is equal to 0.39 at 149 K and decreases linearly to zero at 180 K. Surprisingly, above 180 K the relaxation time τ_{relax_2} becomes longer with increasing T and at 194 K approaches the mean lifetime of the excited state τ_0.

Also the shape of delayed signal patterns collected at an exit angle $\alpha_f = 0$ can be reproduced with a single quadrupole doublet only at temperatures above 180 K. The quantitative analysis of these data sets was impossible due to an additional modulation of the delayed signal by the dynamical beating (see eq. 7.10). The well-pronounced multiple scattering of the resonant photons indicates a large effective thickness of the measured specimen. The assumption $f_{LM}L = 1$ made during the analysis of the specular patterns is no longer valid for the off-specular measurements. In such a case the large number of free parameters in the model function and their strong cross-correlation significantly reduces quality and reliability of the obtained fits. For temperatures below 170 K the first minimum of the Bessel function enters the time interval 40 ns to 60 ns, in which the quantum beating of the rapidly decaying signal is most pronounced and diminishes the accuracy of the fitting routine.

7.8 Model of the liquid/vapor interface

7.8.1 The Mode-coupling prediction for the Lamb-Moessbauer factor

According to the mode-coupling theory (MCT) [84, 3], which has been successfully applied to explain the relaxation in bulk and confined dibutyl phthalate, the Lamb-Mössbauer factor can be separated into phonon-like f_{phonon} and relaxational parts f_{MCT}

$$f_{LM}(T) = f_{phonon}(T) \cdot f_{MCT}(T). \tag{7.26}$$

The $f_{phonon}(T)$ contribution is often approximated by the high temperature limit of the Debye model of the atomic vibration in the solid

$$f_{phonon}(T) = \exp(-\frac{6E_R T}{k_B \theta_D^2}), \tag{7.27}$$

where E_R is the recoil energy associated with the resonant emission(absorption) and θ denotes the Debye temperature of the material. The reduction in $f_{LM}(T)$ due to the fast β-relaxation is implemented in the MCT via a so-

called separation parameter ς

$$f_{MCT}(T) = \begin{cases} f_c + w\sqrt{\varsigma} = f_c + w\sqrt{\frac{T_c - T}{T_c}} & \text{if } T \leq T_c, \\ 0 & \text{if } T > T_c. \end{cases} \tag{7.28}$$

The value of f_{MCT} at the mode-coupling critical temperature T_c is denoted by f_c, and w is the proportionality factor. The MCT predicts a dramatic decrease of the intensity of the resonant signal as the sample temperature approaches T_c, which is usually up to 20% higher than the glass transition temperature T_g. Fig. 7.13 examplifies the temperature dependence of the Lamb-Mössbauer factor for the glassy system with the critical temperature $T_c = 180$ K and f_c =0.

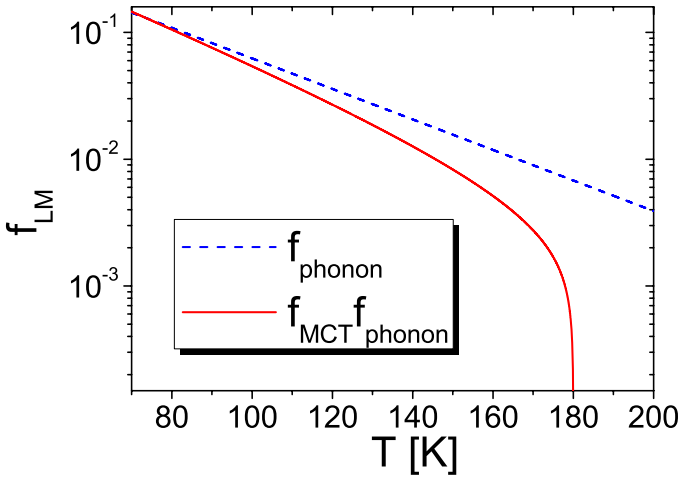

Figure 7.13: The Lamb-Mössbauer factor f_{LM} (red line) versus temperature calculated from the mode-coupling theory for material with the critical temperature T_c=180 K, the Debye temperature θ=70 K, and the recoil energy E_R=1.95·10^{-3}eV. The Debye model (dotted line) prediction is shown for comparison.

7.8.2 Model

To explain the results from the nuclear forward scattering experiment a multilayer model of the liquid/vapour interface is proposed. It is based on the assumption of a gradient in the molecular mobility close to the surface, with the assumption that molecules closer to the surface are more mobile than molecules further away from the surface. The relaxation time, according to this picture, is a function not only of the temperature T but also of the distance z from the surface. The critical temperature T_c is shifted towards lower values near the sample/vapor interface. The exact distribution of $\tau(T, z)$ and

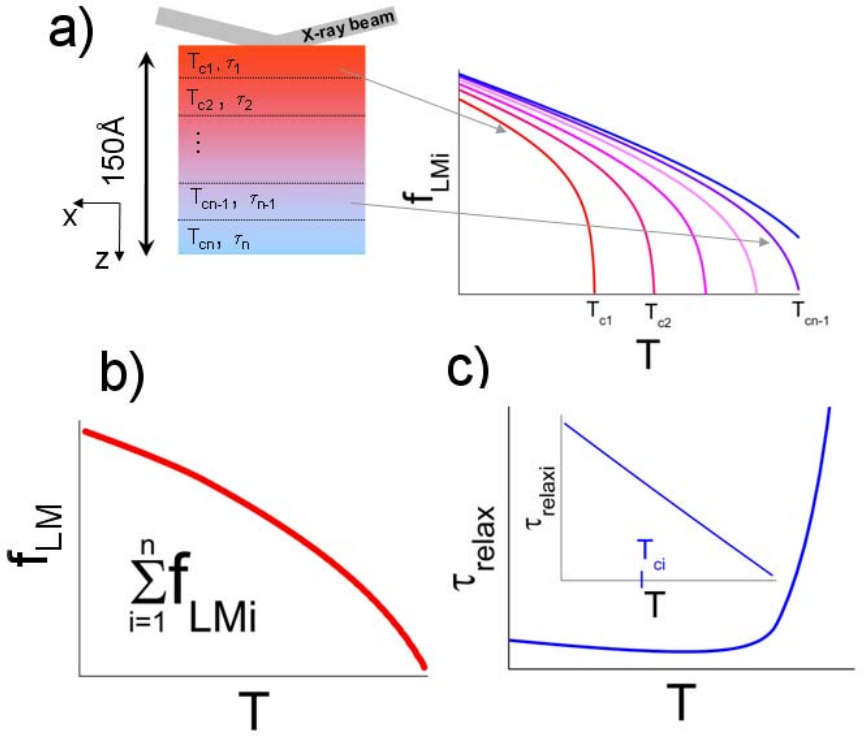

Figure 7.14: The multilayer model of the dibutyl phthalate liquid/vapor interface. a) The probed volume divided into n layers with different relaxation times τ_{relax_i} and the critical temperatures T_{c_i} (the corresponding curves of $f_{LM_i}(T)$ are shown in the graph). The gradient in the molecular mobility near the interface is represented by the transition from the blue color (slowly relaxing liquid) to the red region (very mobile molecules). b) The averaged Lamb-Mössbauer factor of the probed volume. c) Simulated temperature dependence of the effective relaxation time obtained in a QNFS experiment (for the details concerning the calculations see text). Inset: the relaxation time versus temperature for a single layer.

$T_c(z)$ is not specified within this model. The only requirement is that both functions should be monotonic with respect to the independent variables z and T.
The probed volume (determined by the penetration depth of 14.41 keV x-rays into dibutyl phthalate Λ=150 Å) has been divided into n equally thick slices characterized by critical temperatures T_{c_i} and relaxation times τ_i, where $i = 1...n$. The delayed signal at the detector position is the coherent sum of the individual resonant signals from each slice. The amplitudes of the signal emitted by slice i is determined by its Lamb-Mössbauer factor f_{LM_i}, the intensity $I_i(t = 0) = |E_i(t = 0)|^2$ of the prompt pulse at layer i, and the attenuation of the re-emitted signal due to the self-absorption effect. The

intensity recorded during the nuclear forward scattering experiment is then proportional to

$$I(t) \propto |\Sigma_{i=1}^{n} E_i(t=0) f_{LM_i}|^2, \tag{7.29}$$

while the effective relaxation time is approximated by

$$\tau_{relax} = \frac{\Sigma_{i=1}^{n} E_i(t=0) f_{LM_i} \tau_{relax_i}}{\Sigma_{i=1}^{n} E_i(t=0) f_{LM_i}}. \tag{7.30}$$

The electric field of the prompt pulse for each layer can be calculated with the help of the following equation [47]

$$E_i(t=0) = E_0 e^{-Im(q_z')z} \tag{7.31}$$

with

$$q_z' = \frac{2\pi}{\lambda}\sqrt{sin^2\alpha_i - 2\delta + i2\beta}. \tag{7.32}$$

The parameters λ, $\delta(T)$ and $\beta(T)$ in eq. 7.32 denote the wavelength of the incident radiation, dispersion and absorption coefficients of the investigated medium at temperature T.
The intensity and the relaxation time as a function of temperature were simulated using the model for the linear increase of $T_c(z)$ and the exponential decrease of τ_{relax} with increasing depth z. The outcome of the calculations is shown in Fig. 7.14.
The proposed model predicts the decrease of the observed relaxation time of the liquid surface with decreasing sample temperature.

7.8.3 Discussion

An enhancement of the delayed resonant intensity $I(t)$ at lower temperatures (see Fig. 7.12b) reflects the increase of the effective thickness $f_{LM}L_i$ of the investigated specimen. It can be ascribed to either an expanding fraction of the irradiated sample contributing to the quasielastic nuclear forward scattering signal and/or to improved probability of the resonant scattering event f_{LM}. The rapid increase of $I(t)$ around 180 K suggest the formation of the glassy state around this temperature. The precise determination of $I(t)$ is a rather difficult task due to the experimental errors caused by the finite precision of the setup alignment, the resolution effects, and varying sample curvature with the temperature. Additionally, the cross-correlation between the fitting parameters enhances the uncertainty intervals of the obtained results. The statistic of the collected data is not sufficiently good to perform a reliable fitting to retrieve the value of the critical temperature T_c near a free surface.
At the highest temperature only a small fraction of the probed volume contributes to the resonant signal. In the frame of the introduced model in the previous section, this implies only a few layers $i = k...n$ (where k is slightly lower than n) with the sufficiently high f_{LM_i} and long τ_{relax_i} to be detected.

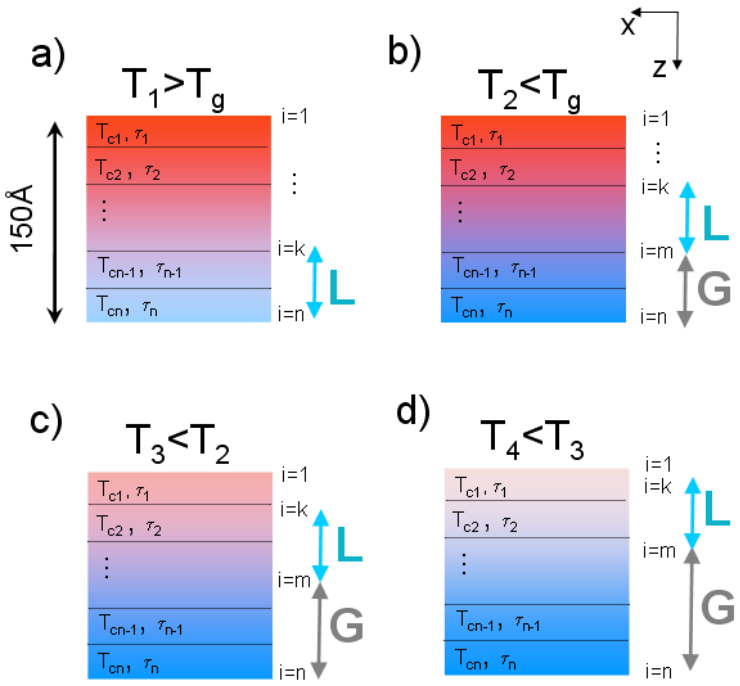

Figure 7.15: Interpretation of the experimental data in the framework of the multilayer model. At temperatures above the glass transition temperature T_g a) only a small fraction of the supercooled liquid L contributes to the QNFS signal (marked by the blue arrow). Below T_g b) the bottom layers transform into the glass G (gray arrow). Further cooling c) and d) shifts the glass/liquid border toward the surface.

This situation is depicted in Fig. 7.15a. The observed relaxation time is then an average over a very narrow distribution of τ_{relax_i}. At lower temperatures more and more layers become "visible" for the nuclear forward scattering experiment (k decreases). Averaging over a wider distribution of τ_{relax_i} results in shifting of the measured τ_{relax} toward shorter values (see Fig. 7.14c). Below T_{c_1} the whole probed volume contributes to the recorded QNFS pattern. Further cooling results in increases of the effective relaxation time τ_{relax_2}, as presented in Fig. 7.14c. Starting from 180 K a distribution of τ_{relax_i} is too broad to be approximated by a single value τ_{relax} and the quasielastic nuclear forward scattering pattern must be modeled with the coherent sum (eq. 7.22) of the signal re-emitted by the frozen ($i = m...n$) $|E_{\Delta Q_1}(t)|^2$ and the liquid ($i = k...m$) $|E_{\Delta Q_2}(t)|^2$ parts of the probed volume, weighted by the factors c and $(1 - c)$, respectively.

Further cooling causes the shift of the glass/liquid border towards the sur-

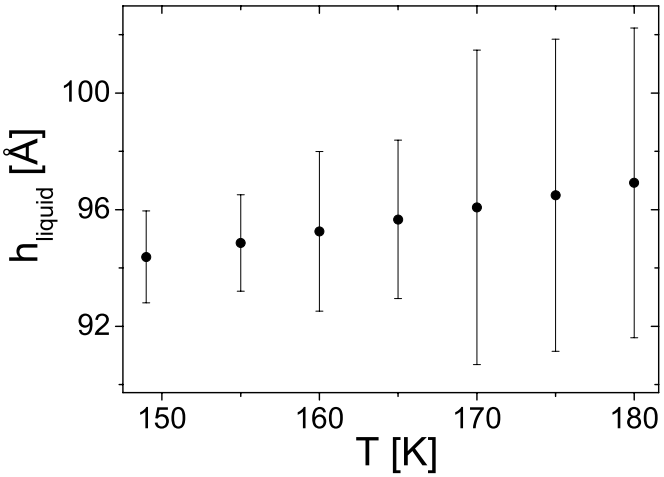

Figure 7.16: Thickness of the liquid part of the probed dibutyl phthalate surface.

face reflected by the larger value of factor c.
The relaxation time of the liquid part of the sample corresponds to the relaxation time of the bulk sample at 210 K, while the slowly relaxing part measured in the grazing incidence geometry has the relaxation time comparable to the bulk DBP cooled below the glass transition temperature. Also the quadrupole splittings provided by the fitting routine $\Omega_1 = 24.4\tau_0^{-1}$ and $\Omega_2 = 24.0\tau_0^{-1}$ match the values reported for the glassy and the liquid states of dibutyl phthalate. The reduction in Ω for more mobile part of dibutyl phthalate reflects the smearing out of the electric field gradient (EFG) experienced by the Fe atoms within the ferrocene molecules. This effect is often termed as the motional narrowing [85, 86].
From the ratio of the intensities re-emitted by the solid and liquid parts of the dibutyl phthalate surface $c/(1-c)$, the thickness of the liquid-like fraction of the probed volume $h \approx 97$ Å at 175 K was estimated. Upon cooling h increases to around 92 Å at 149 K.

The results from the quasielastic nuclear forward scattering experiment indicate the inhomogeneous dynamic to be the inherent property of the free surface.At the bulk glass transition temperature two distinguish relaxation times have been observed. The slower relaxation is identical to the one observed in the bulk glass phase, while the faster relaxation corresponds to the value found in the liquid phase at 210 K, ie. 30 K above the T_g in bulk. The scaled intensities allowed to quantify the thickness of the liquid-like phase to be around 100 Å. Both thickness and relaxation rate are only slightly affected by the cooling to 149 K, ie. 30 K below bulk T_g.

Chapter 8

Summary and discussion

In this work, several surface-sensitive x-ray scttering techniques were applied to obtain a comprehensive picture of the glass transition phenomenon near the liquid/vapor interface of the model organic glass former dibutyl phthalate. The static structure of the supercooled liquid was investigated by means of grazing incidence x-ray diffraction and x-ray reflectivity. The results show that the sample remains fully amorphous and has a uniform electron density ϱ_{el} upon cooling to the glass transition temperature. The reflectivity measurements yielded the value of the surface roughness of $\sigma \approx 3.65$ Å at 300 K. Lowering the sample temperature resulted in a linear decrease of $\sigma(T)$ excluding the possibility of surface freezing within the applied temperature range (175 K<T<300 K).
The second issue addressed during diffraction and reflectivity studies was the influence of the doping of dibutyl phthalate with ferrocene, which was used as a tracer for the quasielastic nuclear forward scattering (QNFS) measurements. It is crucial for the data analysis to confirm that the mixing of those two compounds with a ratio 1:19 does not alter the properties of the liquid/vapor interface of dibutyl phthalate. Ferrocene molecules expelled from the dibutyl phthalate matrix close to the surface are expected to form crystals as they do in their pure state. Since the diffraction pattern of crystalline ferrocene is very rich in the q-region accessible with the surface diffraction experiment, the precipitation of ferrocene from the host was expected to be reflected by the presence of the Bragg reflections on the GID pattern. However, no difference between the diffraction data for the pure and doped liquid was observed.
Because of the large difference between the electron densities of ferrocene $\varrho_{ferrocene} = 0.83 \times 10^{24}\mathrm{cm}^{-3}$ and dibutyl phthalate $\varrho_{DBP} = 0.34 \times 10^{24}\mathrm{cm}^{-3}$ a surface-induced segregation of ferrocene from dibutyl phthalate would lead to the formation of a bilayer structure close to the surface. This in turn would lead to modulation of the Fresnel-type reflectivity curve by so-called Kiessig fringes. All data sets obtained for the solution can be fitted assuming a semi-infinite and uniform liquid with a surface roughness matching the values

of the pure dibutyl phthalate. Within the detection limits, the experiments show that the static structure of the dibutyl phthalate surface is not affected by doping with ferrocene.

The dynamics at the surface on sub-μm length-scales was studied with coherent radiation via an x-ray photon correlation spectroscopy experiment performed under grazing incidence geometry. At room temperature, the capillary wave model provides a good description of the surface modes, while the data collected below 295 K can only be explained in the frame of the Kelvin-Voigt model of viscoelastic media. The structural relaxation rate $\lambda(T)$ retrieved from the XPCS data is in very good agreement with results reported for the bulk liquid well above the calorimetric glass transition temperature T_g. Upon approaching T_g the relaxation rate becomes larger near the surface than in the bulk and at 186 K the difference exceeds one order of magnitude. Since the viscosity $\eta(T)$ was found to be the same at the surface and deep inside the liquid, the increase of the relaxation rate can be attributed to the enhancement of the elasticity close to the liquid/vapor interface. The room temperature value of the shear modulus $\mu = 39$ Pa was extrapolated from the low temperature data.

The pronounced solid-like behavior of the dibutyl phthalate above its melting point $T_m = 238$ K suggests that elasticity can not be ascribed exclusively to the glass formation from the supercooled state but rather to the intra- and intermolecular interactions being present also in liquid at higher temperatures. The viscoelasticity of dibutyl phthalate above its melting temperature has been already observed with acoustic measurements [27], inelastic x-ray scattering [25], ultrasonic studies [20]. Beside dibutyl phthalate, several other non-polymeric organic liquids were reported to exhibit elastic properties above and below their melting temperatures [27, 29].

The enhancement of elasticity near the liquid/vapor interface may be explained by a stronger interaction between the molecules in the topmost layer of the liquid due to unbalanced forces at the surface. In this picture, the surface tension γ and the shear modulus μ are two closely related quantities determining the dynamics at the interface. At higher temperatures the restoring force for the thermal fluctuations is determined mainly by the surface tension, and the surface modes are described well by the capillary wave model. With decreasing temperature elasticity becomes the dominant factor defining the relaxation near the liquid/vapor interface. This is accompanied by the transition of the surface waves from the capillary into the elastic type. Increased elasticity yields a larger relaxation rate at the surface compared to the bulk liquid.

The concept of a higher relaxation rate near the free surface is also supported by the results from the quasielastic nuclear forward scattering experiment, in which the dynamics on molecular length scales around the calorimetric glass transition temperature is studied. This measurement, based on resonant x-

ray absorption, is well-suited to study the fast β-relaxation process in the time window ranging from 10^{-8} s to 10^{-6} s. The obtained data were analyzed in the light of the mode-coupling theory of the glass transition and a model of the liquid(glass)/vapor interface, predicting inhomogeneous dynamics along the distance z from the surface. The QNFS data can be explained when the molecular mobility is assumed to decrease with increasing distance from the interface. Upon cooling the distribution of the relaxation times is continuously shifted towards larger values and around 177 K a part of the probed volume is characterized by a relaxation time comparable to bulk dibutyl phthalate in the glassy state. The data reveals the existence of a 10 nm thick liquid-like surface layer characterized by the relaxation time comparable to the bulk liquid at 210 K.

The results obtained from XPCS and QNFS experiments are a direct proof of the surface-induced increase of the relaxation rate in the supercooled liquids and glasses, suggested by the studies of the polymer interfaces [87] and the simulations performed for the various glass formers [88]. The reduction of the glass transition temperature T_g near the the free surface has been argued to explain the results of positron lifetime spectroscopy [89], ellipsometry [90], and Brillouin light scattering [91].

The effect of liquid-like layer formation on the top of bulk sample is not a unique property of disordered matter but as it was first observed for crystalline materials [92, 93, 94, 95, 96]. Several theoretical descriptions of the surface melting phenomenon were developed to describe the existence of intermediate liquid layer at the crystal/vapor border [97] but very little work on this field has been done for disordered matter. For example, Jagla at al. [98] predicted the wetting of the glass/vapor interface by the liquid layer of thickness $h \sim -ln(T_0 - T)$, where T_0 denotes the thermodynamical glass transition temperature.

According to the XPCS findings, the enhancement in the elasticity is the major influence of the liquid/vapor interface on the dynamics of dibutyl phthalate in the supercooled liquid state. The QNFS measurements indicate that this effect becomes less pronounced with increasing distance from the interface. This results in an inhomogeneous dynamics along the direction perpendicular to the surface. According to this model, both the fast β and α-relaxation are affected by the vicinity of the liquid/vapor interface. Even 30 K below the bulk glass transition temperature a mobile liquid-like layer of the dibutyl phthalate separates the glass and the vapor phases. The gradient in the molecular mobility has been observed above and below the calorimetric glass transition temperature. This indicates an inhomogeneous relaxation to be an inherent property of the free surface. The effect of the liquid/vapor interface on the glass formation extends over several nanometers.

Chapter 9

Appendix

This appendix contains the normalized intensity autocorrelation functions $g_2(\tau, q_x)$ collected from the free surface of pure dibutyl phthalate using the point detector and the CCD camera.

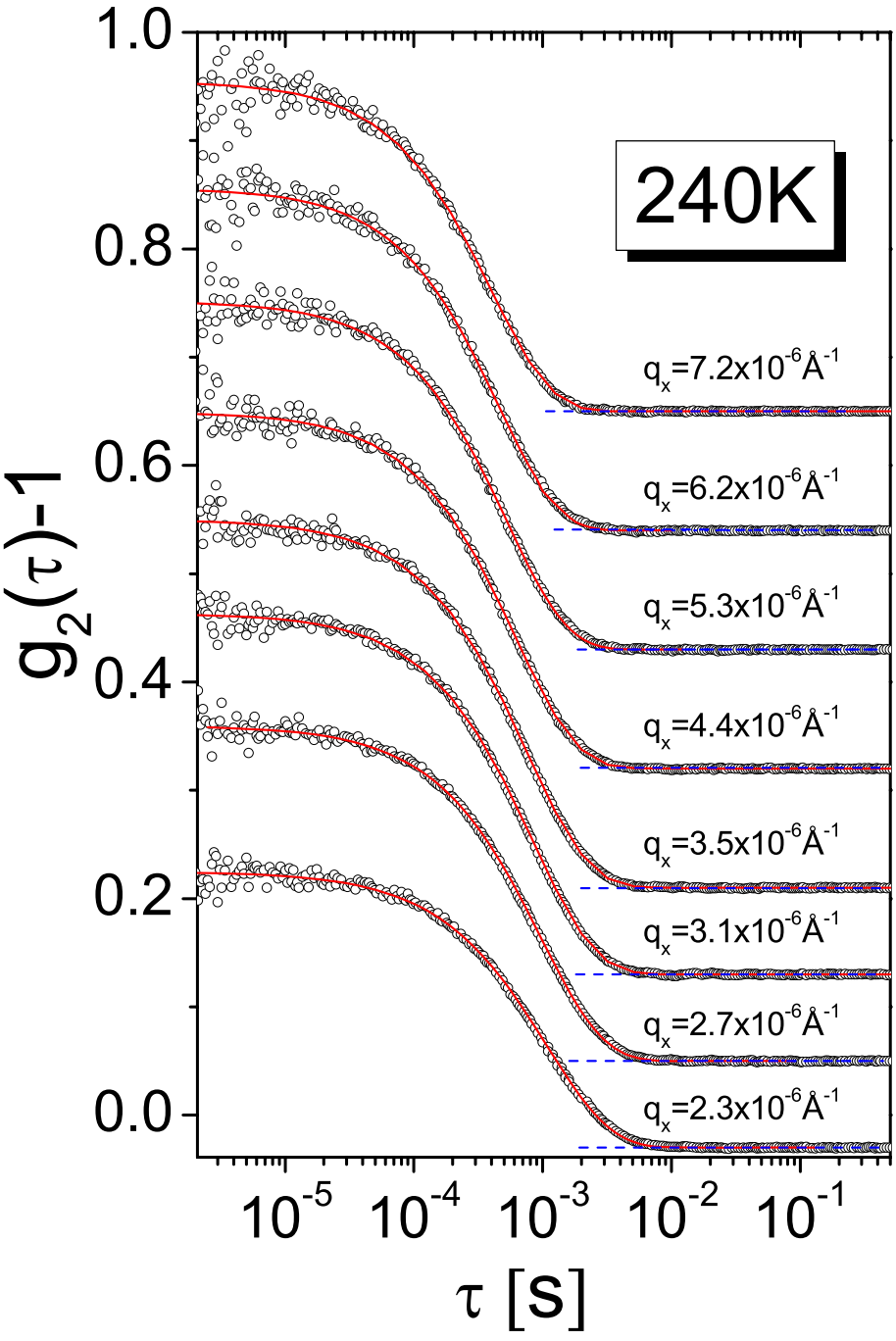

Figure 9.1: The intensity autocorrelation functions $g_2(\tau, q_x)$ recorded on the surface of dibutyl phthalate at 240 K. The origin of the correlation functions have been shifted for clarity and marked with the dashed blue line.

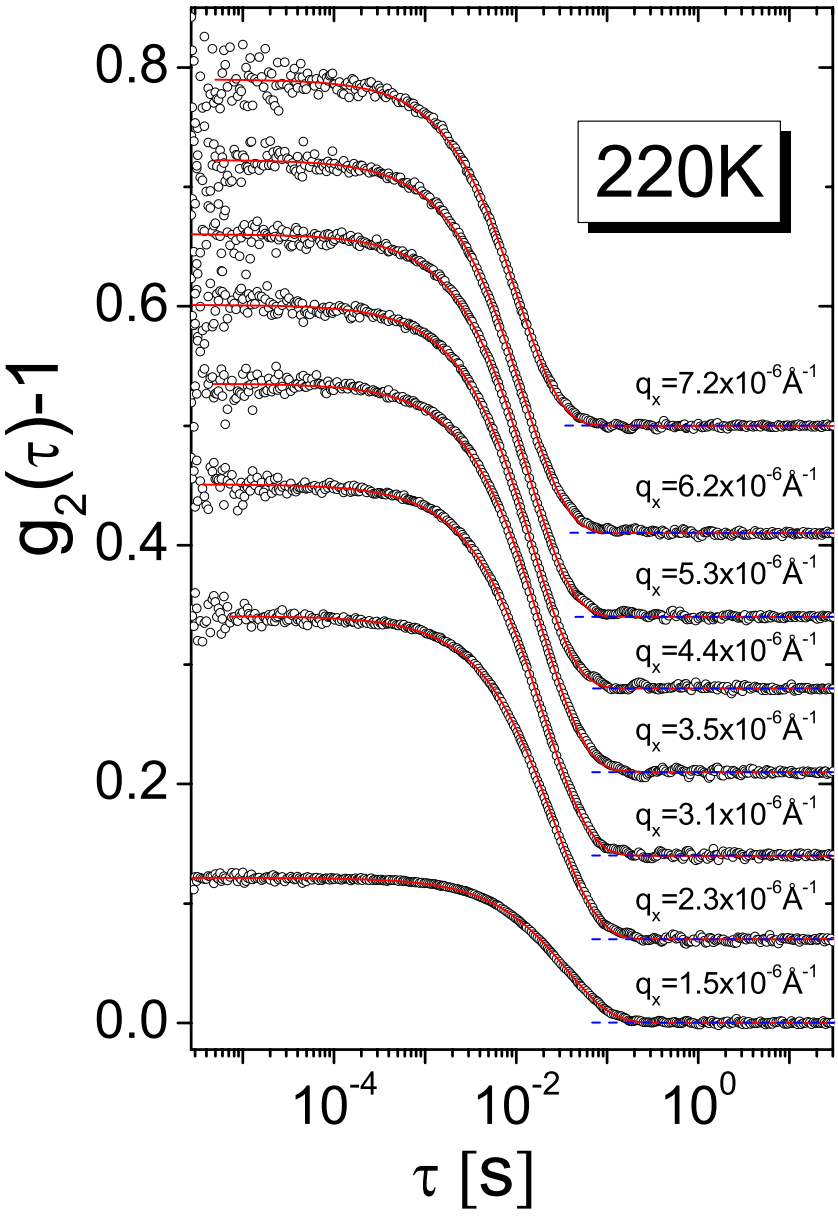

Figure 9.2: The intensity autocorrelation functions $g_2(\tau, q_x)$ recorded on the surface of dibutyl phthalate at 220 K. The origin of the correlation functions have been shifted for clarity and marked with the dashed blue line.

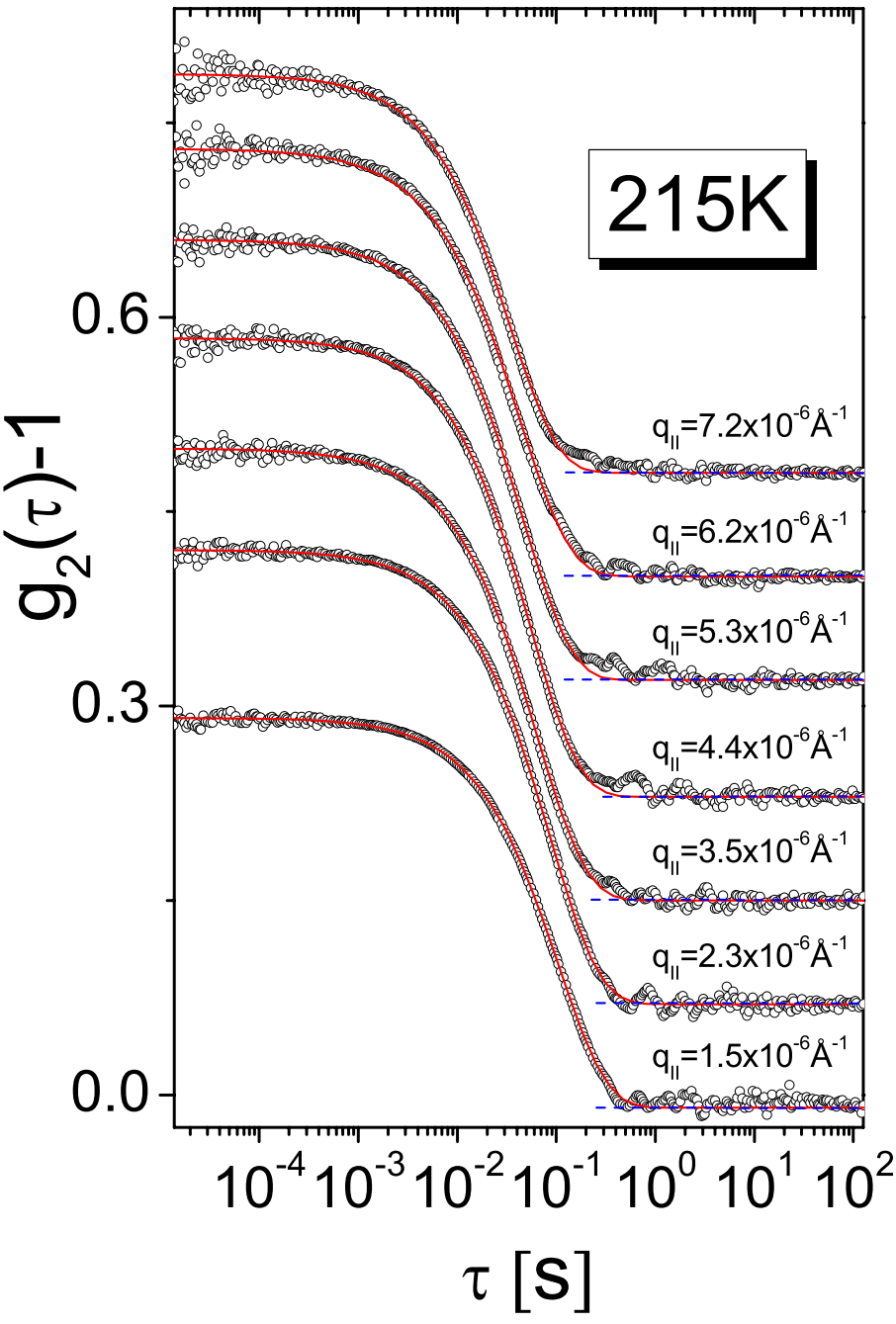

Figure 9.3: The intensity autocorrelation functions $g_2(\tau, q_x)$ recorded on the surface of dibutyl phthalate at 215 K. The origin of the correlation functions have been shifted for clarity and marked with the dashed blue line.

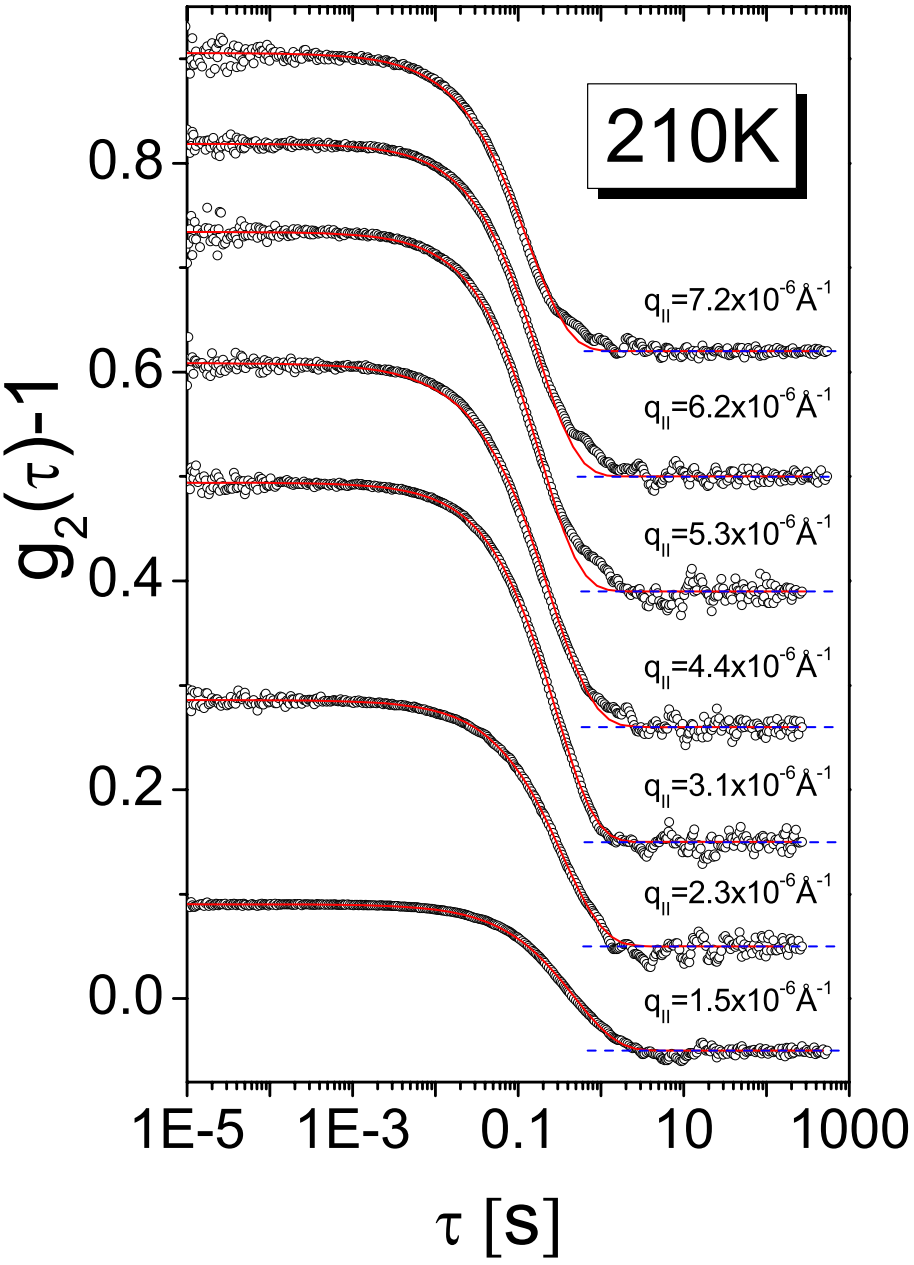

Figure 9.4: The intensity autocorrelation functions $g_2(\tau, q_x)$ recorded on the surface of dibutyl phthalate at 210 K. The origin of the correlation functions have been shifted for clarity and marked with the dashed blue line.

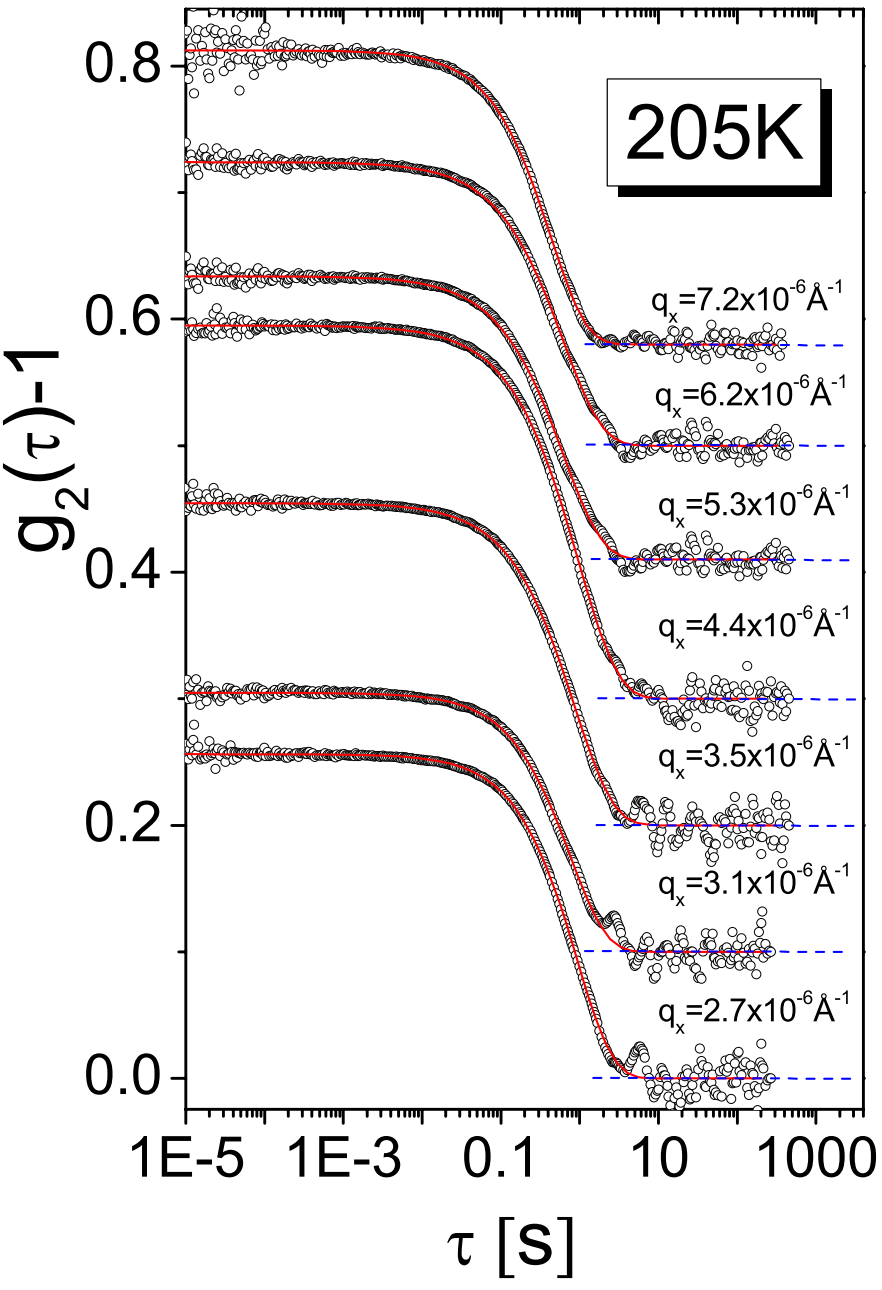

Figure 9.5: The intensity autocorrelation functions $g_2(\tau, q_x)$ recorded on the surface of dibutyl phthalate at 205 K. The origin of the correlation functions have been shifted for clarity and marked with the dashed blue line.

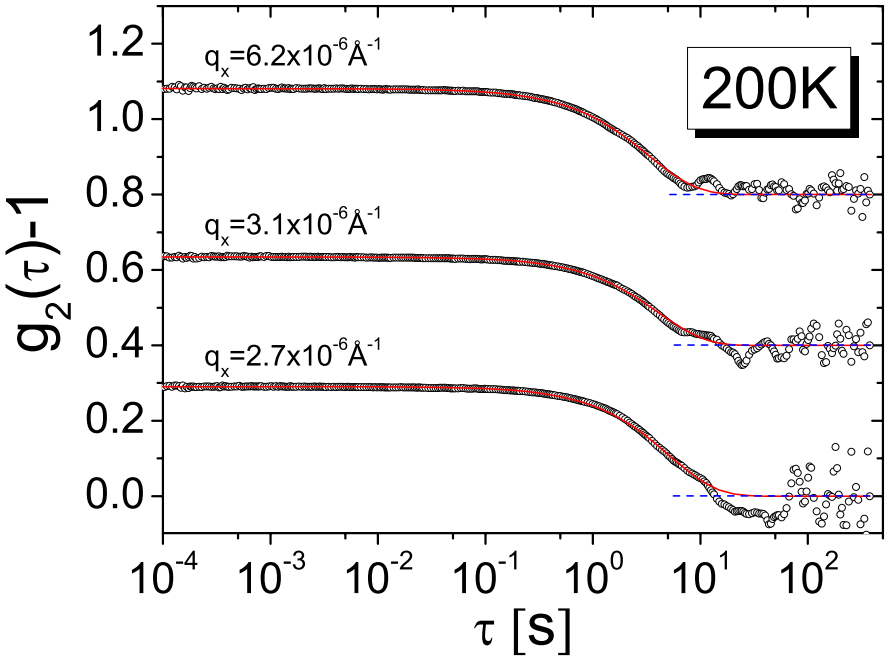

Figure 9.6: The intensity autocorrelation functions $g_2(\tau, q_x)$ recorded on the surface of dibutyl phthalate at 200 K. The origin of the correlation functions have been shifted for clarity and marked with the dashed blue line.

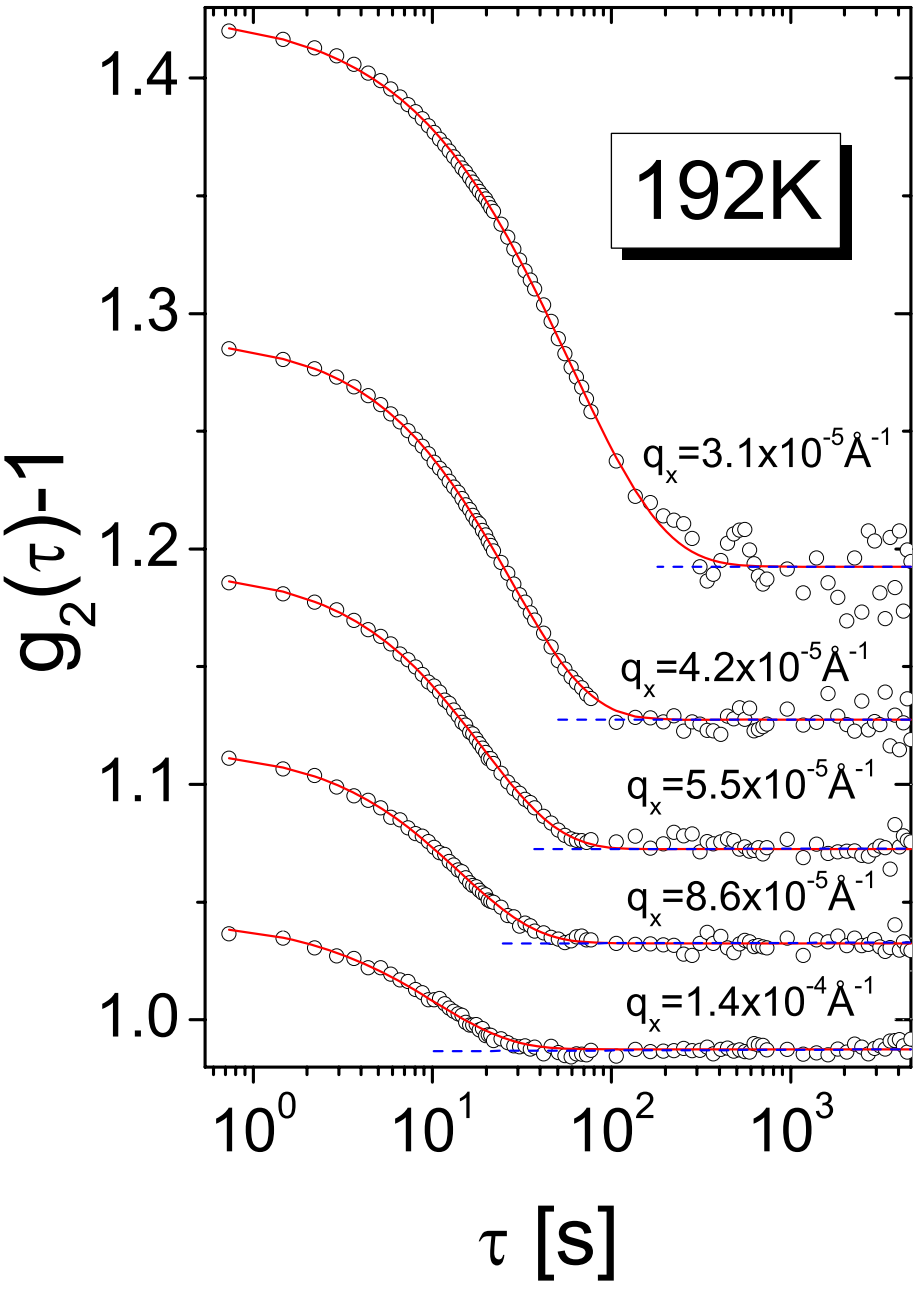

Figure 9.7: Selected intensity autocorrelation functions $g_2(\tau, q_x)$ recorded on the surface of dibutyl phthalate at 192 K. The origin of the correlation functions have been shifted for clarity and marked with the dashed blue line.

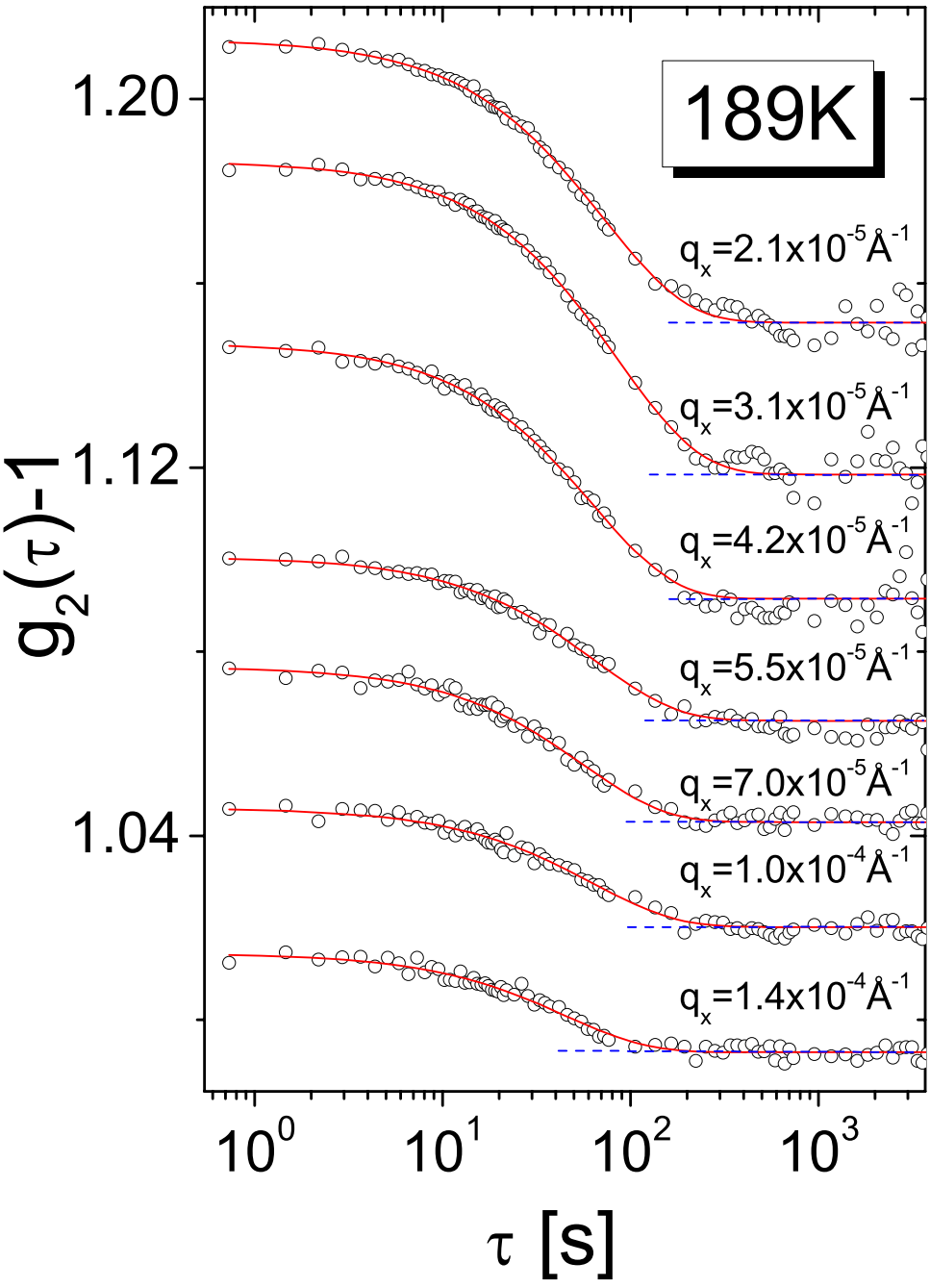

Figure 9.8: Selected intensity autocorrelation functions $g_2(\tau, q_x)$ recorded on the surface of dibutyl phthalate at 189 K. The origin of the correlation functions have been shifted for clarity and marked with the dashed blue line.

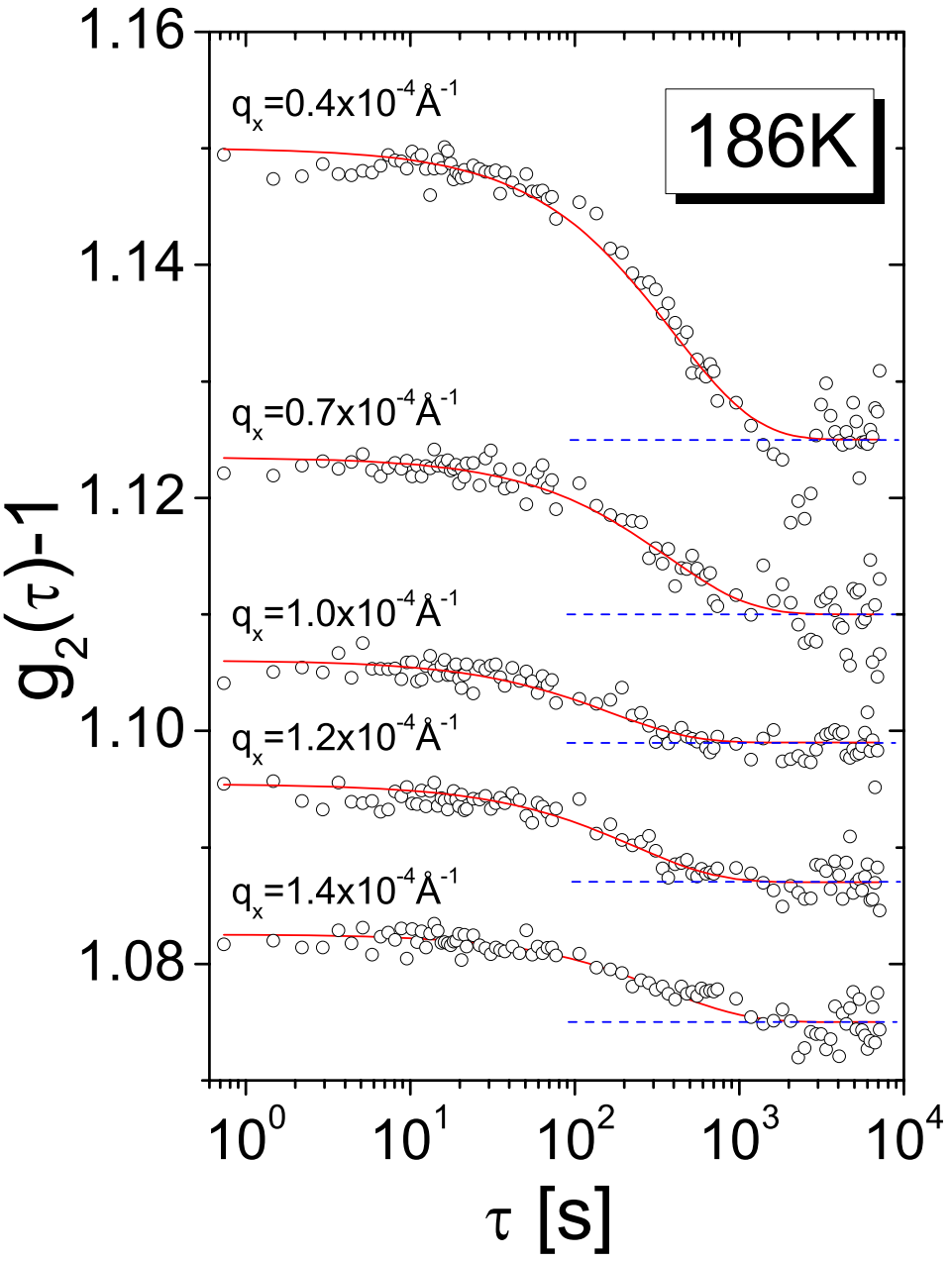

Figure 9.9: Selected intensity autocorrelation functions $g_2(\tau, q_x)$ recorded on the surface of dibutyl phthalate at 186 K. The origin of the correlation functions have been shifted for clarity and marked with the dashed blue line.

Bibliography

[1] J. F. Loffler, Intermetallics **11**, 529 (2003).

[2] B. Frick and D. Richter, Science **267**, 1939 (1995).

[3] H. Z. Cummins, W. M. Du, M. Fuchs, W. Götze, S. Hildebrand, A. Latz, G. Li, and N. J. Tao, Phys. Rev. E **47**, 4223 (1993).

[4] J. A. Forrest and K. Dalnoki-Veress, Advances in Colloid and Interface Science **94**, 167 (2001).

[5] B. Frick, M. Koza, and R. Zorn, *book of abstracts* (PUBLISHER, ADDRESS, 2003).

[6] W. Paul, K. Binder, D. W. Heermann, and K. Kremer, J. Chem. Phys. **95**, 7726 (1991).

[7] P. G. Debenedetti, *Metastable Liquids. Concepts and principles* (Princeton University Press, ADDRESS, 1996).

[8] J. Z. Jiang and K. Saksl, Materials Science and Engineering A **375-377**, 733 (2004).

[9] S. Streit-Nierobisch, C. Gutt, M. Paulus, and M. Tolan, Phys. Rev. B **77**, 041410 (2008).

[10] C. Angel, Science **267**, 1924 (1995).

[11] L.-M. Wang, C. A. Angell, and R. Richert, J. Chem. Phys. **125**, 074505 (2006).

[12] E. Donth, *The Glass Transition. Relaxation Dynamics in Liquids and Disordered Materials* (Springer Series in Materials Science, ADDRESS, 2001).

[13] K. Niss, C. Dalle-Ferrier, G. Tarjus, and C. Alba-Simionesco, Journal Of Physics-Condensed Matter **19**, (2007).

[14] G. Adam and J. H. Gibbs, J. Chem. Phys. **43**, 139 (1965).

[15] M. Arndt, R. Stannarius, H. Groothues, E. Hempel, and F. Kremer, Phys. Rev. Lett. **79**, 2077 (1997).

[16] M. H. Cohen and D. Turnbull, J. Chem. Phys. **31**, 1164 (1959).

[17] G. Wellenreuther, Ph.D. thesis, University of Hamburg, 2005.

[18] A. Meyer, H. Franz, J. Wuttke, W. Petry, N. Wiele, R. Rüffer, and C. Hübsch, Zeitschrift für Physik B Condensed Matter **103**, 479 (1997).

[19] R. L. Cook, H. E. King, Jr., C. A. Herbst, and D. R. Herschbach, J. Chem. Phys. **100**, 5178 (1994).

[20] A. J. Barlow, J. Lamb, A. J. Matheson, P. R. K. L. Padmini, and J. Richter, Proceedings of the Royal Society of London. Series A, Mathematical and Physical Sciences **298**, 467 (1967).

[21] R. S. Paluch M., Ziolo J. and H. P., J. Phys.: Condens. Matter **9**, 5485 (1997).

[22] T. Asthalter, M. Bauer, U. van Burck, I. Sergueev, H. Franz, and A. I. Chumakov, European Physical Journal E **12**, S9 (2003).

[23] G. Wellenreuther, H. Franz, U. Bürck, and I. Sergueev, Hyperfine Interactions **165**, 141 (2005).

[24] A. J. Barlow, J. Lamb, and A. J. Matheson, **292**, 322 (1966).

[25] A. Mermet, E. Duval, A. Polian, and M. Krisch, Phys. Rev. E **66**, 031510 (2002).

[26] I. Sergueev, H. Franz, T. Asthalter, W. Petry, U. van Bürck, and G. V. Smirnov, Phys. Rev. B **66**, 184210 (2002).

[27] B. Badmaev and B. Damdinov, Acoustical Physics **47**, 487 (2001).

[28] D. Brace, S. Gottke, H. Cang, and M. Fayer, J. Chem. Phys. **116**, 1598 (2002).

[29] B. B. Badmaev, T. S. Dembelova, and B. B. Damdinov, Advances in Colloid and Interface Science **104**, 299 (2003).

[30] A. Schönhals, Europhys. Lett. **56**, 815 (2001).

[31] M. Paluch, J. Zioło, S. J. Rzóska, and P. Habdas, Phys. Rev. E **54**, 4008 (1996).

[32] N. Menon, S. R. Nagel, and D. C. Venerus, Phys. Rev. Lett. **73**, 963 (1994).

[33] T. Asthalter, I. Sergueev, H. Franz, R. Rffer, W. Petry, K. l. Messe, P. Hrter, and A. Huwe, Eur. Phys. J. B **22**, 301 (2001).

[34] R. Richert, K. Duvvuri, and L. Duong, J. Chem. Phys. **118**, 1828 (2003).

[35] L.-M. Wang, V. Velikov, and C. A. Angell, J. Chem. Phys. **117**, 10184 (2002).

[36] R. Deegan, R. Leheny, N. Menon, S. Nagel, and D. Venerus, J. Phys. Chem. B **103**, 4066 (1999).

[37] H. Mo, G. Evmenenko, and P. Dutta, Chemical Physics Letters **415**, 106 (2005).

[38] R. Lim and S. J. O'Shea, Phys. Rev. Lett. **88**, 246101 (2002).

[39] X. Z. Wu, E. B. Sirota, S. K. Sinha, B. M. Ocko, and M. Deutsch, Phys. Rev. Lett. **70**, 958 (1993).

[40] S. Ruby, B. Zabransky, and P. Flinn, J. Phy. C **37**, 745 (1976).

[41] T. Seydel, A. Madsen, M. Sprung, M. Tolan, G. Grübel, and W. Press, Rev. Sci. Instrum. **74**, 4033 (2003).

[42] M. Tolan, *X-Ray Scattering from Soft-Matter Thin Films: Materials Science and Basic Research* (Springer-Verlag Telos, ADDRESS, 1999).

[43] A. Braslau, P. S. Pershan, G. Swislow, B. M. Ocko, and J. Als-Nielsen, Phys. Rev. A **38**, 2457 (1988).

[44] J. Daillant and M. Alba, Rep. Prog. Phys. **63**, 1725 (2000).

[45] J. Als-Nielsen and D. McMorrow, *Elements of modern x-ray physics* (John Wiley & Sons Ltd., ADDRESS, 2001).

[46] B. T. Holy. V, Pietsch U., in *High resolution x-ray scattering from thin films and multilayers*, edited by H. G. (Springer, ADDRESS, 1999).

[47] Maillaender, Ph.D. thesis, Ludwig-Maximilians-Universitaet Muenchen, 1990.

[48] A. Braslau, M. Deutsch, P. S. Pershan, A. H. Weiss, J. Als-Nielsen, and J. Bohr, Phys. Rev. Lett. **54**, 114 (1985).

[49] E. A. Guggenheim, J. Chem. Phys. **13**, 253 (1945).

[50] E. Eckstein, J. Qian, R. Hentschke, T. Thurn-Albrecht, W. Steffen, and E. W. Fischer, J. Chem. Phys. **113**, 4751 (2000).

[51] T. K. Xia and U. Landman, Phys. Rev. B **48**, 11313 (1993).

[52] E. Szczesniak, S. Glowinkowski, W. Suchanski, and S. Jurga, Solid State Nuclear Magnetic Resonance **8**, 73 (1997).

[53] W. Mason, W. Baker, H. McSkimin, and J. Heiss, Phys. Rev. **75**, 936 (1949).

[54] C. Gutt, T. Ghaderi, V. Chamard, A. Madsen, T. Seydel, M. Tolan, M. Sprung, G. Grübel, and S. K. Sinha, Phys. Rev. Lett. **91**, 076104 (2003).

[55] C. Gutt, T. Ghaderi, V. Chamard, A. Madsen, T. Seydel, M. Tolan, M. Sprung, G. Grübel, and S. K. Sinha, Phys. Rev. Lett. **91**, 179902 (2003).

[56] J. Jäckle and K. Kawasaki, J.Phys.: Condens. Matter **7**, 4351 (1995).

[57] A. Madsen, T. Seydel, M. Sprung, C. Gutt, M. Tolan, and G. Grübel, Phys. Rev. Lett. **92**, 096104 (2004).

[58] W. Flügge, in *Viscoelasticity*, edited by S. edition (Springer-Verlag, ADDRESS, 1975).

[59] J. L. Harden, H. Pleiner, and P. A. Pincus, J. Chem. Phys. **94**, 5208 (1991).

[60] H. Nakanishi and S. Kubota, Phys. Rev. E **58**, 7678 (1998).

[61] R. B. Dorshow and L. A. Turkevich, Phys. Rev. Lett. **70**, 2439 (1993).

[62] R. Meister, C. J. Marhoeffer, R. Sciamanda, L. Cotter, and T. Litovitz, J. Appl. Phys. **31**, 854 (1960).

[63] A. Madsen, T. Seydel, M. Tolan, and G. Grübel, Journal of Synchrotron Radiation **12**, 786 (2005).

[64] T. Thurn-Albrecht, W. Steffen, A. Patkowski, G. Meier, E. W. Fischer, G. Grübel, and D. L. Abernathy, Phys. Rev. Lett. **77**, 5437 (1996).

[65] J. Bruce and R. Pecora, *Dynamic Light Scattering: With Applications to Chemistry, Biology, and Physics* (Courier Dover Publications, ADDRESS, 2000).

[66] R. S. Stock and W. H. Ray, Journal of Polymer Science: Polymer Physics Edition **23**, 1393 (1985).

[67] P. Pusey, *Photon Correlation Spectroscopy and Velocimetry (Plenum, New York), edited by H. Z. Cummins and E. R. Pike* (PUBLISHER, ADDRESS, 1977).

[68] Z. Jiang, H. Kim, X. Jiao, H. Lee, Y.-J. Lee, Y. Byun, S. Song, D. Eom, C. Li, M. H. Rafailovich, L. B. Lurio, and S. K. Sinha, Phys. Rev. Lett. **98**, 227801 (2007).

[69] C. Gutt, T. Ghaderi, M. Tolan, S. K. Sinha, and G. Grubel, Phys. Rev. B **77**, 094133 (2008).

[70] R. Fendt, Ph.D. thesis, Technische Universitt Dortmund, 2007.

[71] D. Lumma, L. B. Lurio, S. G. J. Mochrie, and M. Sutton, Rev. Sci. Instrum. **71**, 3274 (2000).

[72] T. Seydel, A. Madsen, M. Tolan, G. Grübel, and W. Press, Phys. Rev. B **63**, 073409 (2001).

[73] H. Kim, A. Rühm, L. B. Lurio, J. K. Basu, J. Lal, D. Lumma, S. G. J. Mochrie, and S. K. Sinha, Phys. Rev. Lett. **90**, 068302 (2003).

[74] P. K. Dixon, L. Wu, S. R. Nagel, B. D. Williams, and J. P. Carini, Phys. Rev. Lett. **65**, 1108 (1990).

[75] S. A. Dzyuba and Y. D. Tsvetkov, Journal of Structural Chemistry **28**, 343 (1987).

[76] G. Smirnov, Hyperfine Interactions **97-98**, 551 (1996).

[77] Y. V. Shvyd'ko, Hyperfine Interactions **123-124**, 275 (1999).

[78] U. van Bürck and G. V. Smirnov, Hyperfine Interactions **90**, 313 (1994).

[79] A. Q. R. Baron, A. I. Chumakov, H. F. Grünsteudel, H. Grünsteudel, L. Niesen, and R. Rüffer, Phys. Rev. Lett. **77**, 4808 (1996).

[80] A. Q. Baron, Hyperfine Interactions **125**, 29 (2000).

[81] W. Götze and L. Sjögren, Reports on Progress in Physics **55**, 241 (1992).

[82] G. Smirnov, Hyperfine Interactions **123-124**, 31 (1999).

[83] C. Janot, P. Delcroix, and M. Piecuch, Phys. Rev. B **10**, 2661 (1974).

[84] T. R. Kirkpatrick, Phys. Rev. A **31**, 939 (1985).

[85] R. Kubo and T. Tomita, Journal of the Physical Society of Japan **6**, 888 (1954).

[86] P. W. Anderson, Journal of the Physical Society of Japan **6**, 316 (1954).

[87] R. D. Priestley, C. J. Ellison, L. J. Broadbelt, and J. M. Torkelson, Science **309**, 456 (2005).

[88] B. Böddeker and H. Teichler, Phys. Rev. E **59**, 1948 (1999).

[89] G. B. DeMaggio, W. E. Frieze, D. W. Gidley, M. Zhu, H. A. Hristov, and A. F. Yee, Phys. Rev. Lett. **78**, 1524 (1997).

[90] S. Kawana and R. A. L. Jones, Phys. Rev. E **63**, 021501 (2001).

[91] J. A. Forrest, K. Dalnoki-Veress, J. R. Stevens, and J. R. Dutcher, Phys. Rev. Lett. **77**, 2002 (1996).

[92] J. W. M. Frenken, P. M. J. Mare, and J. F. van der Veen, Phys. Rev. B **34**, 7506 (1986).

[93] C. S. Jayanthi, E. Tosatti, and L. Pietronero, Phys. Rev. B **31**, 3456 (1985).

[94] J. W. M. Frenken and J. F. v. d. Veen, Phys. Rev. Lett. **54**, 134 (1985).

[95] A. Trayanov and E. Tosatti, Phys. Rev. Lett. **59**, 2207 (1987).

[96] R. Trittibach, C. Grütter, and J. H. Bilgram, Phys. Rev. B **50**, 2529 (1994).

[97] J. G. Dash, Contemporary Physics **30**, 89 (1989).

[98] E. A. Jagla and E. Tosatti, EPL (Europhysics Letters) **51**, 648 (2000).

Acknowledgements

I would like to deeply thank the various people who, during the last three years provided me with useful and helpful assistance. Without their care and consideration this work would not have accomplished.
I am grateful to my supervisors **Prof. Dr. Wilfried Wurth** and **Dr. Hermann Franz** for setting up this project and giving me the opportunity to explore the new fields of science at HASYLAB.
First, there are two gentlemen who I especially want to thank. Without their help I would not have been able to finish this project and learn all the things that I have learned in the past three years.
I am grateful to **Dr. Hermann Franz** for the supervision of my work in HASYLAB. I enjoyed to be a member of his research group. I appreciate his unlimited patience in educating me for last three years and shearing his knowledge with me. I benefited a lot from the discussions (starting always with: "I have a question..."). Working with him, especially performing the experiments under his guidance, was a great pleasure.
I am in great debt to **Dr. Christian Gutt**. I want to thank him for the advices during the experiments and the data analysis. He was always happy to bring me back on the right track, whenever I got lost in the world of the coherent x-rays scattering form the soft matter surfaces. His support can not be overestimated.
I would like to express my gratitude for the help, I got form **Dr. Christian Gutt** and **Dr. Hermann Franz** during writing this manuscript. They made a great effort to correct my terrible English and to show me how to describe the experimental data in the right way. Their patience and determination to hunt down all of the missing or misused prepositions impressed me a lot (but I am afraid, in this field, I am very resistant to knowledge). I thank them very much for they enormous work.
A big "Thank you" goes to **Frank-Uwe Dill**, who did impressive work during designing, building, and commissioning of the cryostat used during this project. His great sense of humor made working with him extremely enjoyable.
During my stay in Hamburg beside the *Hard X-ray scattering and diffraction* research group I also been working with the major part of the **Dr. Gerhard Grübel** *Scattering with Coherent X-rays* research group. I would like to thank **Dr. Gerhard Grübel** for his hospitality. I always felt welcomed in his team. I would like to say thank you to **Dr. Olaf Leupold** and **Dr. Oliver Seeck**. Their doors were always open for me in case of problems and questions.
I thank to **Dr. Bernd Struth** and **Dr. Dmitri Novikov** for their help in performing the experiments at the beamline BW1.
Dr. Ilia Sergueev and **Dr. Yuriy Chushkin** from European Synchrotron Radiation Facility are gratefully acknowledged for their assistance during the

experiments at ID18 and ID10A. It was a pleasure for me to perform the measurements at those beamlines.
The sample preparation would not be possible without help of **Klaudia Hagemann** and **Dr. Tina Autenrieth**, who were so kind to tolerate me occupying all of the free space in their labs.
I could not leave Hamburg without saying "Thank you" to **Christine Berber** and without expressing my gratitude for all the help in solving the problems related to the administrative issues.
All my fellow PhD students and postdocs have to be mentioned: **Bente**, **Simone**, **Tina**, **Sebastien**, **Fabian**, **Lorenz** and **Kai**. I enjoyed not only to work but also to spend my free time with them. I hope we will all meet again sometimes.
I cant skip mentioning my friend **Milena**. It was a true pleasure and great fun to shear the office with her. We have work together in developing some remarkable sample cells. I enjoyed both to work and to chat with her (not always about the scientific topics).
Few words about my friend **Wojciech**. We studied together at three universities in three countries. He turned out to be a great companion and office mate.
"For sure", I would like to say "*merci*" to **Agnès** for her friendship and support whenever I needed it.
At last but not least I want to thank my mother and my sister for believing in me and encouraging me during all my studies. I dedicate this work to them.

Thank you!